Journal Pre-proofs

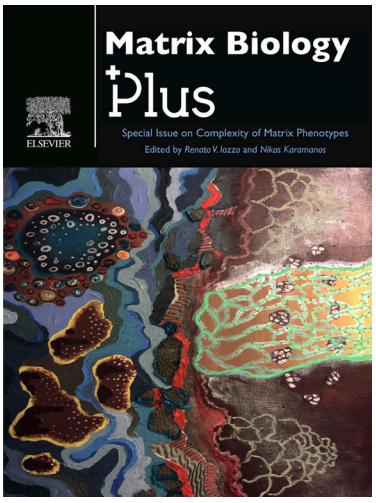

The importance of matrix in cardiomyogenesis: Defined substrates for maturation and chamber specificity

Jake Ireland, Kristopher A. Kilian

PII: S2590-0285(24)00020-6
DOI: https://doi.org/10.1016/j.mbplus.2024.100160
Reference: MBPLUS 100160

To appear in: *Matrix Biology Plus*

Received Date: 7 February 2024
Revised Date: 15 August 2024
Accepted Date: 16 August 2024

Please cite this article as: J. Ireland, K.A. Kilian, The importance of matrix in cardiomyogenesis: Defined substrates for maturation and chamber specificity, *Matrix Biology Plus* (2024), doi: https://doi.org/10.1016/j.mbplus.2024.100160

The importance of matrix in cardiomyogenesis: defined substrates for maturation and chamber specificity

Jake Ireland[1], and Kristopher A. Kilian[1,2,3*]

[1]School of Chemistry, UNSW Sydney, Sydney, New South Wales, Australia

[2]School of Materials Science and Engineering, UNSW Sydney, Sydney, New South Wales, Australia

[3]Australian Centre for NanoMedicine, UNSW Sydney, Sydney, New South Wales, Australia

Abstract

The optimization of human embryonic stem cell-derived cardiomyocytes (hESC-CM) is a promising approach for generating cardiac cells for disease modelling and regenerative medicine. However, current protocols invariably lead to mixed population of cardiac cell types and often generate cells that resemble embryonic phenotypes. Here we developed a combinatorial approach to assess the importance of extracellular matrix proteins (ECMP) in directing the differentiation of cardiomyocytes from human embryonic stem cells (hESC). We did this by focusing on combinations of ECMP commonly found in the developing heart with a broad goal of identifying combinations that promote maturation and influence chamber specific differentiation. We formulated 63 unique ECMP combinations fabricated from collagen 1, collagen 3, collagen 4, fibronectin, laminin, and vitronectin, presented alone and in combinations, leading to the identification of specific ECMP combinations that promote hESC proliferation, pluripotency, and germ layer specification. When hESC were subjected to a differentiation protocol on the ECMP combinations, it revealed precise protein combinations that enhance differentiation as determined by the expression of cardiac progenitor markers kinase insert domain receptor (KDR) and mesoderm posterior transcription factor 1 (MESP1). High expression of cardiac troponin (cTnT) and the relative expression of myosin light chain isoforms (MLC2a and MLC2v) led to the identification of three surfaces that promote a mature cardiomyocyte phenotype. Action potential morphology was used to assess chamber specificity, which led to the identification of matrices that promote chamber-specific cardiomyocytes. This study provides a matrix-based approach to improve control over cardiomyocyte phenotypes during differentiation, with the scope for translation to cardiac laboratory models and for the generation of functional chamber specific cardiomyocytes for regenerative therapies.

Keywords: Extracellular Matrix Proteins, Cardiomyocyte Differentiation, Chamber Specification, Action Potential Morphology, Array Platform, Cardiomyocyte Maturation.

Introduction

It's been two decades since cardiac cell therapies were first investigated with the initial hypothesis that non-contracting stem cells could transdifferentiate when injected into an infarct region (1, 2). Despite the promising benefits of pre-clinical trials, cell therapies in larger animals appeared to interfere with native electrical conduction (3). The decades since have seen tremendous improvements in cardiac modelling and regenerative medicines as the field of pluripotent stem cell research has expanded. The use of human embryonic stem cells (hESC) and human induced pluripotent stem cells (hiPSC) has provided alternative options to primary cells for investigating cardiomyogenisis (4), exploring cardiomyocyte lineage specification (5), and has pioneered the field of engineered heart muscle (EHM) as alternative delivery methods of stem cells to infarct regions (6, 7). Contracting cardiomyocytes developed from human embryonic stem cells, known as human embryonic stem cell-derived cardiomyocytes (hESC-CM), have been cultured in laboratories around the world with some incredible ability to resemble the morphologic and phenotypic qualities of the adult heart (8, 9). The efficiency of differentiating cardiomyocytes from a pluripotent cell source is nearing 100% for most modern protocols (10) but issues persist that prohibit these cells from entering clinical use (11, 12). Currently clinical translation for stem cell derived cardiomyocytes face controversy regardless of the cell source as hESC pose ethical dilemmas and hiPSC struggle to find a footing in clinical translation due to the large number of genetic changes required for pluripotent cell generation (119, 120). In this study we chose to work with hESC because they have extant success in clinical translation to treat ischemic cardiac conditions in humans and serves as a reliable cell source for modelling cardiac differentiation in vitro (121). The criteria for a protocol to meet clinical standards require phenotypic and electrophysiological purity, a high differentiation efficiency, and an absence of adverse effects in pre-clinical animal models (13). Whilst differentiation efficiency can be achieved, most protocols give rise to a heterogeneous population of cardiac cell types that often display varying action potential morphologies (5, 14).

Efforts to improve cardiac differentiation protocols are also influenced by the need for better cardiac models for safety pharmacology testing. The S7B guidelines from the International Conference of Harmonisation (IHC) stipulate a need to investigate ion channel interactions, in particular with hERG receptors (15). These guidelines encourage simple studies, often with Chinese hamster ovarian (CHO) cells transfected with a hERG receptor that

demonstrate a simplistic and impractical example of ion channel interactions that don't account for the broad range of available ion channels of a functional adult cardiomyocyte (16, 17). These studies also highlight the limited representation of biomimetic systems as pharmacological agents that pass these trials and can later be removed from the market, such was the case with Cisapride (18), and Terfenadine (19) for unknown ion channel interactions not found during pre-clinical testing. The other side of this coin is that beneficial compounds that could help millions of patients, could unfairly be removed from further testing due to an incomplete picture of ion channel interactions in hERG receptor models (20). The Comprehensive in-vitro Pro-arrhythmic assay (CiPA) is a movement that is encouraging the use of alternative methods including PSC-CM in safety pharmacology testing (20, 21). Commonly PSC-CM represent immature cardiomyocytes similar to embryonic cardiac tissue with an unorganized ultrastructure and poor ion channel presentation which can vary with increased incubation periods leading to inconsistent results (22). Before PSC-CM become a viable cardiac model for safety pharmacology testing, or to be used in cell therapies, variability in maturation and electrophysiological responses need to be standardised.

Several modern protocols have a range of achievements in the purity and quality of PSC-CM (10, 23, 24, 25). The majority of these protocols focus on the utilisation of small molecules responsible for guiding lineage pathways that would be most favourable for producing cardiomyocytes whilst microenvironmental cues of the extracellular matrix, have received less attention. While these chemical signals are important factors, they often lead to unguided differentiation towards a cardiac lineage without the ability to direct chamber specification. Several studies have claimed to enrich kinetic or electrophysiological properties of chamber-specific cell types that are often described as "atrial-like, ventricular-like, and nodal-like" cells (26, 27, 28, 29). However, to consistently produce these chamber-like cell types, specific differentiation protocols need to be developed to direct chamber specificity with rigorous selection criteria that factor in the importance of extracellular matrix proteins (ECMP) (30, 31, 32).

The importance of ECMP in cardiac differentiation and maturation is evidenced by the variability of expression in a developing embryo (33). Furthermore, congenital diseases responsible for improper ECMP expression show the significance ECMP can have on alignment (34), growth (35), morphology (36, 37, 38), chamber specification (39, 40), and maturation (41, 42). ECMP remodelling following an ischemic event or during progressive heart failure is also evidence of the importance of how cardiomyocytes will adapt to alterations in the ECMP structure (43, 44, 45, 46). Studies utilising decellularised ECMP scaffolds show the influence the ECMP structure can have on inducing differentiation of stem cells towards a cardiomyocyte lineage without the need to implement a differentiation protocol (47, 48, 49, 50). The evidence of these studies into the ECMPs importance during the early stages of cardiomyogenisis shows how providing "outside-in" signaling can augment differentiation (51). Early methods for culturing hESC used MEF feeder layers that would deposit a complex mixture of ECMP that provided a suitable substrate that allowed attachment whilst maintaining the stemness and proliferation of the cells (52). More modern protocols now utilize commercial substrates like Matrigel™ or Geltrex™ which are extracted and purified substrates made up of the same complex mixture of ECMP. Whilst these animal-derived matrices have gained good reputation for maintaining stem cells they can often show wide variability in composition and do not reflect the native ECMP composition found in cardiac tissue and are a poor representation of the ECMP present during human cardiac development (53, 54).

In recent years, considerable work has been devoted to replacing Matrigel™ with singular ECMP such as fibronectin, laminin or vitronectin (55, 56, 57, 58), as well as combinatorial assessments of ECMP matrices (59, 60, 61) for the maintenance of stem cell pluripotency. Alternative studies have been investigating protein combinations to direct cardiomyocyte lineage specification by utilizing proteins prevalent in native cardiac tissues such as fibronectin and laminin. Jointly these proteins showed an improved differentiation efficiency when cultured on a 70:30 ratio of fibronectin to laminin (62). More recent research focuses on identifying specific proteins required for the in vivo maintenance of human cardiomyocytes. The abundance of laminin 221 and 521 in the adult human heart was investigated and showed improved cardiomyocyte progenitor specification and enhanced cardiac function in mice when transplanted into areas of the induced infarct (63). Other studies demonstrate a strategy for the maturation of hPSC-CM monolayers, by emphasizing the importance of specific ECMP conditions in a 3D culture format and the involvement of integrin signaling pathways in the maturation process (64). While these findings are intriguing, a comparative analysis with modern differentiation protocols reveals lower differentiation efficiency or improvements when PSC-CM are cultured using specialized techniques and fabricated platforms not readily available to most laboratories. Additionally, the observed enhancement in animal models is often associated with cultures undergoing prolonged in vitro incubation. Conflicting studies suggest that improvements in in-vivo cell therapies may arise due to in vitro extracellular matrix remodeling resulting from extended culture periods (64, 65), and similar results can be achieved through alternate techniques that do not utilize ECMP substrates (66). Despite these advancements, the precise role of specific proteins in guiding differentiation, maturation, and chamber specificity within the cardiac lineage remains to be fully understood.

In this paper, we report an ECMP microarray approach to evaluate the role of initial matrix conditions in directing cardiac differentiation in hESCs. We used 6 commonly found ECMP including collagen 1, collagen 3, collagen 4, fibronectin, laminin, and vitronectin by presenting them alone and in combinations to produce 63 different protein permutations. These ECMP surfaces were assessed for promotion of proliferation, maintenance of pluripotency, and expression of germline-specific biomarkers. We then analysed this data in combination with the biomarker expressions that would typically follow cardiomyocyte differentiation by investigating the commitment to the mesoderm linage, and the influence on promoting

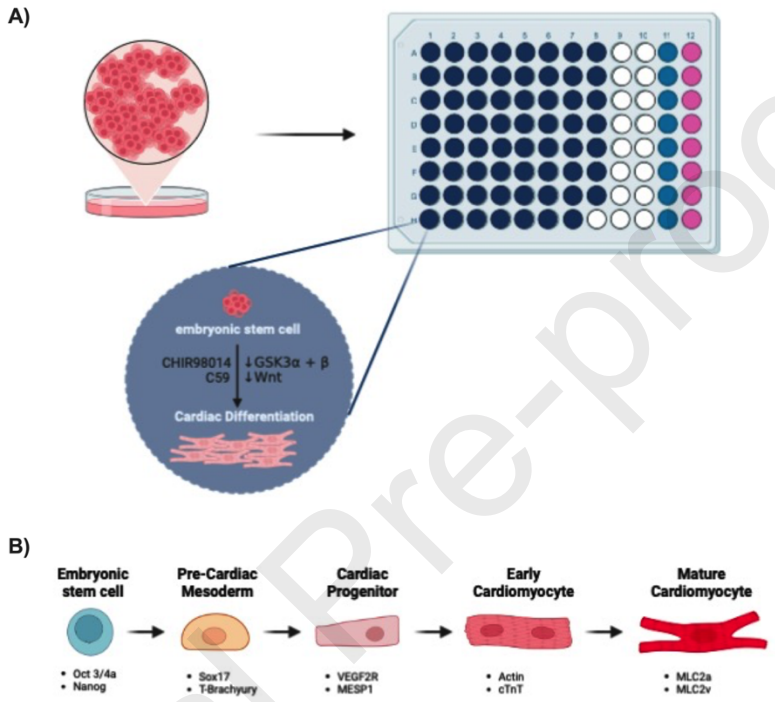

Figure 1. ECM Array Plate to investigate cardiomyocyte differentiation lineage specification. A) ECMP array seeded with hESC and cultured for 5 days. Cells are then differentiated using a ventricular cardiomyocyte differentiation protocol. B) Cells are fixed and stained at various timepoints throughout the cardiomyocyte lineage so assess the effects ECMP combinations have on differentiation potential. Created by BioRender.com

cardiomyocyte progenitors. Induction of differentiation using media formulations and analysis of cardiomyocyte biomarkers revealed ECMP combinations that enhance cardiomyogenisis, with three surfaces that promote high functional maturation as determined by contraction analysis. Custom criterion - based on molecular markers and action potential morphology -was used to identify ECMP combinations that direct differentiation to ventricular, atrial, conduction, and nodal phenotypes, providing the first matrix-based approach to direct chamber specificity whilst highlighting how ECMP affect the critical milestones throughout cardiomyocyte differentiation. The workflow of these experiments are detailed in figure 1.

Results

Protein microarrays identify optimal microenvironments for pluripotent stem cell proliferation.

Before delving into the impact of ECMP on cardiomyocyte differentiation, our investigation first focused on how our ECMP array could affect the proliferation and pluripotency of hESC. To explore the combinations of ECMPs available for supporting pluripotent stem cells, numerous studies have employed an array technique. These studies often utilize protein spotters on a biomimetic hydrogel to enhance throughput, ensuring accuracy and reproducibility. However, caution is warranted, as many of these studies may be misleading, deviating from traditional culture techniques and introducing features that can specifically impact differentiation. Such features include alterations in substrate stiffness (67, 68, 69), topographical confinement (70, 71, 72), restricted cell populations (72, 73), and paracrine signalling from adjacent microenvironments (74, 75). The array spot method, with its incorporated features, may identify optimal ECMP combinations for a particular array setup, but potentially lacks a full representation of the traditional in vitro culture conditions utilized for pluripotent stem cell proliferation and maintenance in clinical settings. Traditional cell culture methods, like plastic multiwell cell culture dishes, are frequently adapted and scaled up for clinical protocols. In contrast, the array-based approach allows the creation of numerous cost-effective and user-friendly microenvironments that can be replicated in various laboratories.

In this study, six commonly encountered ECMP were selected and arranged within a 96-well plate, creating 63 distinct permutations. The chosen matrix proteins included collagen 1, collagen 3, collagen 4, fibronectin, laminin, and vitronectin. Figure 2A outlines the arrayed protein combinations, utilizing 63 wells of a 96-well plate to represent unique protein permutations. Prior to the fabrication of the array, the proteins were dissolved in 1x DPBS at a concentration of 25 µg/mL. A final volume of 200 µL was added to each well, and the concentrations of individual proteins were adjusted based on the number of proteins combined in each well. This method of concentration dilution was implemented to ensure uniform protein concentrations across all wells, eliminating it as a potential source of variability among combinations.

After seeding hESCs across the array, we measured confluency on each ECMP combination over 5 days using the Olympus Confluency Checker. For measuring cell viability, alamarBlue™ was used as a measure of cells' metabolic activity. This was used in conjunction with the confluency software to differentiate between growth and fitness. From Figure 2C and S1, we can see a general correlation between cell viability and confluency for most ECMP combinations but also some disparities. This highlights the dynamic nature of hESC in response to

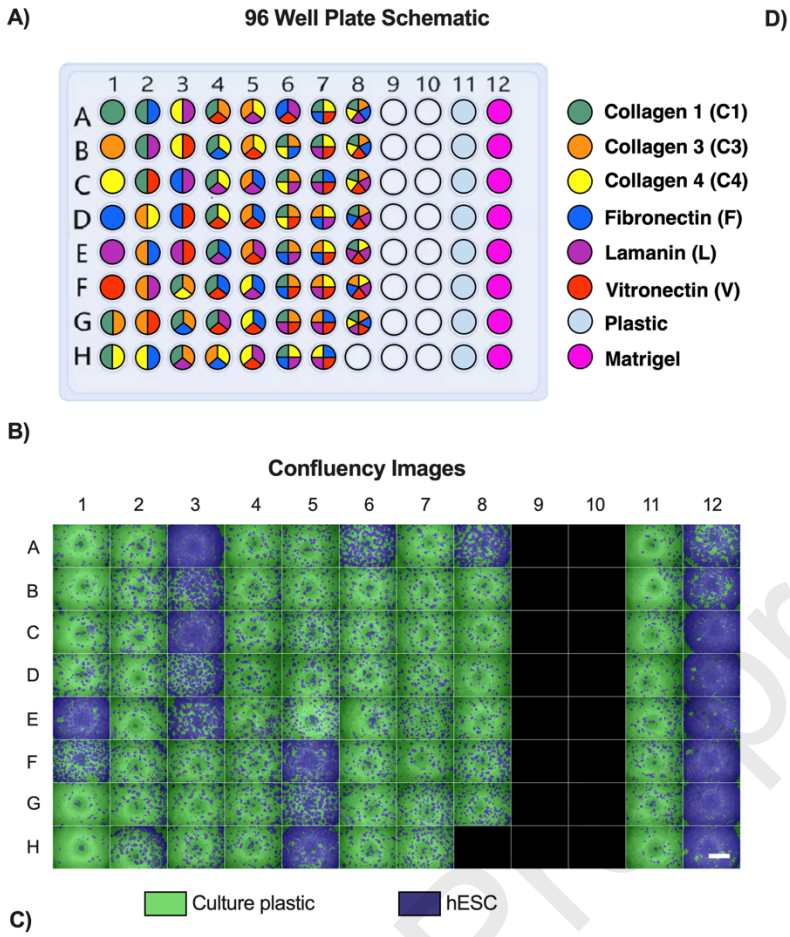

D)

Protein Combination	Well plate Location	Well Plate Number
C1	A1	1
C3	B1	2
C4	C1	3
F	D2	4
L	E1	5
V	F1	6
C1C3	G1	7
C1C4	H1	8
C1F	A2	9
C1L	B2	10
C1V	C2	11
C3C4	D2	12
C3F	E2	13
C3L	F2	14
C3V	G2	15
C4F	H2	16
C4L	A3	17
C4V	B3	18
FL	C3	19
FV	D3	20
LV	E3	21
C1C3C4	F3	22
C1C3F	G3	23
C1C3L	H3	24
C1C3V	A4	25
C1C4F	B4	26
C1C4L	C4	27
C1C4V	D4	28
C1FL	E4	29
C1FV	F4	30
C1LV	G4	31
C3C4F	H4	32
C3C4L	A5	33
C3C4V	B5	34
C3FL	C5	35
C3FV	D5	36
C3LV	E5	37
C4FL	F5	38
C4FV	G5	39
C4LV	H5	40
FLV	A6	41
C1C3C4F	B6	42
C1C3C4L	C6	43
C1C3C4V	D6	44
C1C3FL	E6	45
C1C3FV	F6	46
C1C3LV	G6	47
C1C4FL	H6	48
C1C4FV	A7	49
C1C4LV	B7	50
C1FLV	C7	51
C3C4FL	D7	52
C3C4FV	E7	53
C3C4LV	F7	54
C3FLV	G7	55
C4FLV	H7	56
C1C3C4FL	A8	57
C1C3C4FV	B8	58
C1C3C4LV	C8	59
C1C3FLV	D8	60
C1C4FLV	E8	61
C3C4FLV	F8	62
C1C3C4FLV	G8	63
Matrigel	A11-H11	64
Plastic	A12-H12	65

Figure 2. ECMP Plate Array A) Layout of arrayed ECMPs in a 96 well plate. hESC are seeded at $1.24x10^4$ $cells/cm^2$ to allow proliferation over 5 days. **B)** Images of hESC using Olympus confluency checker where green donates culture plastic and purple donates cells. Images taken on day 5 at 10X magnification, Scale bar 500μM. **C)** Graphical comparison of the viability and confluency of all 63ECMP combinations to highlight similarities and differences of the ECMP combinations on the hESC. **D)** List of proteins combinations used to generate the ECMP array with the proteins name abbreviation, the location of the well in the 96 well plate and the well plate number referenced to the X axis of the comparison of confluency and viability graph.

different microenvironments and how cell spreading is not always correlated to the cell's metabolic fitness and vice versa. The dotted threshold lines in figure S1 indicate the response of hESC on the commercial substrate Matrigel. We see there are a handful of ECMP combinations that had higher confluency and metabolic viability in comparison to Matrigel, indicating an improved proliferative ability on select ECMP combinations. Most ECMP combinations showed a decreased confluence and viability compared to Matrigel, indicating some ECMP combinations can inhibit cell proliferation while others may display an induced apoptotic response. This comparison demonstrates how hESC morphology is not always the best indicator of viability.

On day 5 (120h), three independent cultures of hESC cells cultured on the 63 different ECMP combinations were fixed and stained with DAPI to assess the quantity of DNA present in each well (PRO):

$$PRO = \frac{\chi - \mu_{DNA}}{c} \qquad \textit{(Equation 1)}$$

Where χ is the Log_2 of the DNA signal for the well, μ_{DNA} is the average of the Log_2 DNA signal for all the wells on the plate, and σ_{DNA} is the standard deviation of the Log_2 DNA signals for all the wells on the plate. Proliferation Index values from the replicated cultures (n=3 per ECMP condition) were averaged for each ECMP combination (μ_{PRO}). The proliferation behaviour of the hESC cells to each ECMP combination, μ_{PRO} are displayed in a heat map in Figure 2. Each row corresponds to the ECMP combination, and the three columns represent the three independent cultures. The rows and columns were clustered using Euclidian distancing as a similarity metric with an average linkage method. The combinations are displayed using a color code of blue to red to indicate two cluster groups of lower and higher proliferation compared to the global average mean (μ_{PRO} = 0), respectively.

By performing a Pearson correlation between the three independent cultures, we investigated the prevalence of ECMP combinations in relation to the observed proliferation. We found a number of ECMP combinations that consistently produced high proliferation rates (red) and low proliferation rates (blue) as displayed in figure 3. Whilst these ECMP combinations could be prevalent in these groups due to biological variation, the prevalence of the individual ECMP in the high and low proliferation combinations is intriguing. These findings are also mirrored in Figure S4 where the effects of the individual ECMP on proliferation when averaging from the three biological repeats.

Prior research has emphasized the significant role of collagen 4 as a major component of the basement membrane across the human body, often collaborating with various extracellular matrix (ECM) proteins to promote growth and remodeling in disease scenarios (45). Therefore, it is not surprising that our findings indicate an equal presence of collagen 4 in both high and low-proliferation groups. As illustrated in Figure 3, S2, and S4, laminin and vitronectin are prominently featured in the high proliferation group but less so in the low proliferation group. Conversely, collagens I

and III exhibit a higher frequency in the low proliferation group and a lower frequency in the high proliferation group.

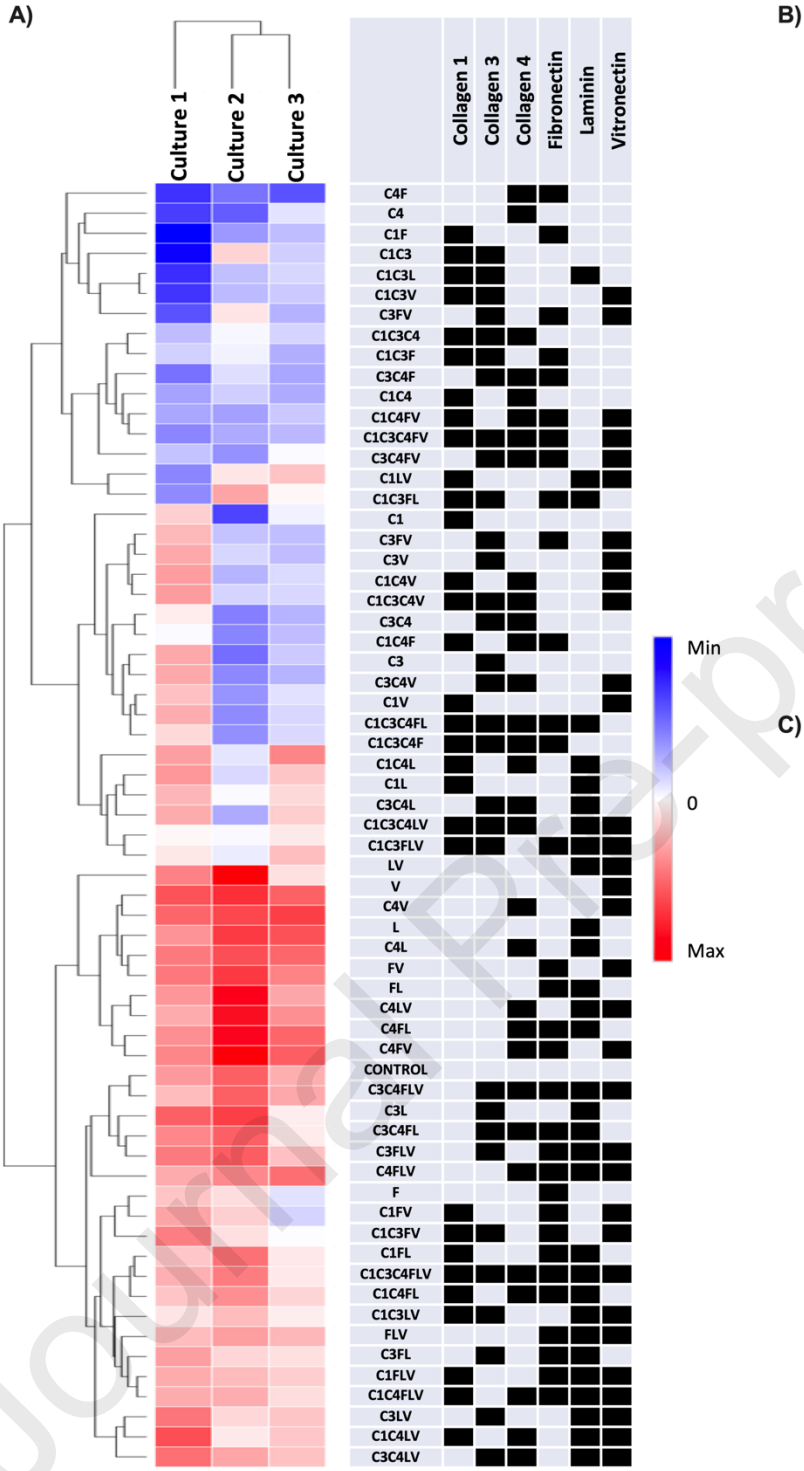

B)

Low proliferation ECMP

	Protein Combination
1	C4
2	C1C4
3	C1F
4	C3C4
5	C4F
6	C1C3C4
7	C1C3F
8	C1C3L
9	C1C3V
10	C1C4F
11	C3C4F
12	C1C3C4L
13	C3C4FV
14	C1C3C4FV

Protein	# of groups including protein
Collagen 1	9
Collagen 3	9
Collagen 4	10
Fibronectin	6
Laminin	2
Vitronectin	3

C)

High proliferation ECMP

	Protein Combination
1	Matrigel
2	L
3	V
4	C4L
5	C4V
6	FL
7	FV
8	LV
9	C3FL
10	C3LV
11	C4FL
12	C4FV
13	C4LV
14	FLV
15	C1C4FL
16	C1FLV
17	C3C4LV
18	C3FLV
19	C4FLV
20	C1C4FLV
21	C3C4FLV

Protein	# of groups including protein
Collagen 1	3
Collagen 3	5
Collagen 4	10
Fibronectin	12
Laminin	15
Vitronectin	14

Figure 3. **Heat map of extracellular matrix proteins (ECMPs) combinations effect on human embryonic stem cell (hESC) proliferation**. **A)** Heat map of the mean proliferation index values (μ_{PRO}) of each ECMP combination (row) for the three independent cultures (columns). The ECMP combination are indicated with the protein name anocrynm and the shaded boxes in the table to the right of the heat map. A hierarchical clustering was performed with a Euclidian distancing metric and an average linkage method. Hierarchical clustering of the ECMPs revealed two segregated groups (i) Higher proliferation than the global average mean (red boxes) (ii) Lower proliferation than the global average mean of 0 (blue boxes). **B and C)** listed ECMP combinations that produce a consistently higher or lower proliferation response in three independent cultures. A secondary breakdown of the frequency of individual ECMP in the high and low proliferation combinations is also listed.

Relationships between proliferation and pluripotency on defined protein microenvironments

To ascertain the effects of the ECMP combinations on the level of pluripotency in comparison to proliferation, hESCs were cultured for 5 days before being fixed and stained for stemness markers Oct3/4a and Nanog (Figure 4). While Oct3/4a and nanog will normally be highly expressed in pluripotent cells, the expression level of nanog can be variable in individual cells. Previous studies on pluripotency in hESC have also shown that a low nanog expression level can maintain pluripotency in culture without differentiating (122). Whilst we expect stemness markers in hESC to be highly expressed in undifferentiated cells, we used the expression of OCT3/4a as a measure of pluripotency and confirmed pluripotency by comparison to the nanog expression level. For each protein combination, the ratio (R) of the Log_2 of the OCT3/4a signal and the DNA signal was calculated. From this, a pluripotency index value (PLU) can be calculated for each protein combination using the equation below:

$$PLU = \frac{R - \mu_{ratio}}{\sigma_{ratio}} \qquad \textit{(Equation 2)}$$

Here, R represents the ratio value for the protein combination, μ_ratio signifies the average of all ratio values across every protein combination, and σ_ratio is the standard deviation for all ratio values across every protein combination. Each ECMP combination is then assigned coordinates (PRO, PLU) to visualize the relationship between hESC proliferation and pluripotency on different ECMP combinations (Figure 4B). Pluripotency index values from three independent replicates (n = 3 per ECMP condition) were collected and averaged (μ_PLU) for each ECMP combination.

In Figure S3, the heatmap displays individual pluripotency index values alongside proliferation index values. Rows represent different ECMP combinations, and the six columns represent independent proliferation and pluripotency array experiments. Clustering analysis, utilizing Euclidean distancing and an average linkage method, organized ECMP combinations into four distinct groups, aligning with the quadrants in Figure 4B. These groups are: i) high proliferation and high pluripotency (red group/top right), ii) high proliferation and low pluripotency (green group/bottom right), iii) low proliferation and low pluripotency (blue group/bottom left), and iv) low proliferation and high pluripotency (orange group/top left).

Plotting the coordinates (PRO, PLU) uncovered a negative correlation between pluripotency and proliferation index values ($r = -0.7847$, $p < 0.0001$), suggesting that an ECMP reducing pluripotency tends to increase proliferation. No ECMP combinations strongly promoted both proliferation and pluripotency simultaneously. However, combinations including collagen I (C1) and collagen IV (C4) with laminin (L) or vitronectin (V) emerged more than once as promoters of both. Conversely, the absence of collagen IV (C4) in these combinations led to decreased pluripotency and proliferation. Matrigel favored proliferation over pluripotency at day 5, possibly due to slight differentiation from high confluency. A repeated test on Matrigel fixed on day 3

showed the expected result of high pluripotency and lower proliferation. Examples of proteins dominant in each quadrant are illustrated in Figure 4A with OCT3/4 immunostaining images.

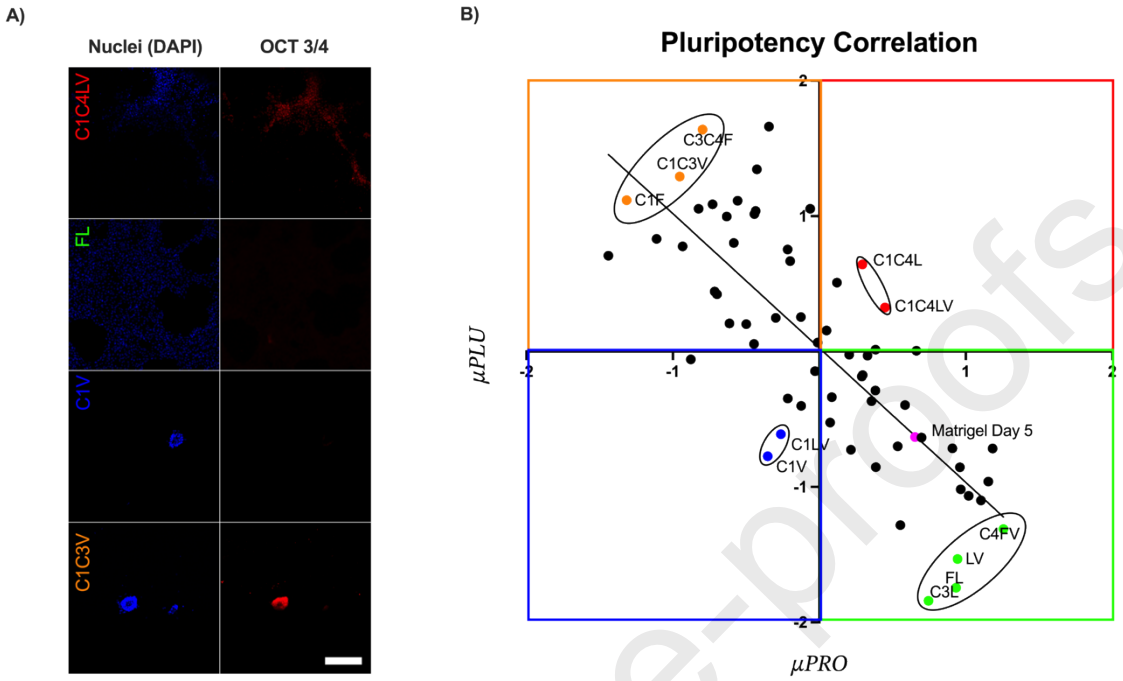

Figure 4. Influence of extracellular matrix protein (ECMP) combinations on human embryonic stem cell (hESC) proliferation and corresponding pluripotency on day 5 of culture. A) Phase contrast images of cells in 96 well at 4x magnification (Scale bar = 500μM) and the respective immunofluorescent images of the DAPI and OCT4 biomarker at 10X magnification (Scale bar = 100μM). These images are representative of similar images (n=3) using a single plane confocal image. B) The mean proliferation index values (μPRO) and mean pluripotency index values (μPLU) for each ECMP combination on day 5 of the culture were average between the three independent cultures and graphed using a Pearson's correlation. The ECMP combinations are plotted into one of four groups i) High proliferation and high maintenance of pluripotency (red) ii) High proliferation and low maintenance of pluripotency (green) iii) Low proliferation and low maintenance of pluripotency (blue) iv) Low proliferation and high maintenance of pluripotency (orange). These high and low data points are referring to the averaged index values around the global average mean (0).

Correlation plots in Figure S4 analyze the magnitude effects of each ECMP on proliferation and pluripotency. Collagens 1, 3, and 4 had a negative impact on proliferation but a net positive effect on pluripotency, indicating a conducive environment for maintaining stem cells. Collagen 4 had a minor impact on proliferation compared to collagens 1 and 3. This effect is also observed in Figure 4 between the blue and red quadrants, where the ECMP combinations containing collagen 4 had higher pluripotency. Collagen 1 had the most significant impact, decreasing proliferation and promoting pluripotency. Laminin and vitronectin positively affected proliferation but had a net negative impact on pluripotency, suggesting a conducive proliferative microenvironment with differentiation influence. Fibronectin was the only ECMP negatively affecting both proliferation and pluripotency, and no ECMP showed a positive impact on both.

Defined matrix proteins guide the expression of germline molecular markers.

The ability to generate all cell types from a single hESC means we have the opportunity to develop cardiac models and specific cardiac cell types that could be used for regenerative cell therapies. The utilization of an ECMP substrates is allowing us to manipulate thel of hESC differentiation and guide them down specific pathways. Insights into embryology have revealed key signaling pathways that regulate germline specification that can also influence the formation of their downstream derivatives. Employing our ECMP array for evaluating the impact of ECMP combinations on proliferation and pluripotency in H9 hESC, we discovered that specific ECMP combinations exhibit superior pluripotency promotion compared to leading commercial substrates like Matrigel™ and Geltrex™. Notably, certain ECMP combinations demonstrated diminished expression of pluripotency markers, suggesting potential germ layer differentiation and a potential leaning toward a specific germ lineage. The ability for ECMP combinations to potentially influence germ linage specification is intriguing as cardiac differentiation could be enhanced if ECMP combinations promote mesodermal and pre-cardiac lineages. Wnt activation is required for the activation of all three germlines but additional regulatory signaling is required for specific germlines. Endodermal and mesodermal lineages originate from a Foxa2 positive region of the primitive streak and require Wnt suppression and activin promotion and are generally able to able to alternate until lineage commitment proteins are expressed (4). To explore this further, we immunostained the hESC for the endoderm marker Sox17 and the mesoderm marker T-Brachyury. Using the equation below, we then used the averaged intensity signals from subsequent con-focal images to create an index value for each of the 63 protein combinations.

$$Biomarker\ Index\ Value\ (BIV) = \frac{\chi - \mu_{BIV}}{\sigma_{BIV}} \qquad \textit{(Equation 3)}$$

Where the Biomarker Index Value (BIV) is calculated from χ which is the Log_2 of the signal for the well, μ_{BIV} is the average of the Log_2 signal of all the wells on the plate, and σ_{BIV} is the standard deviation of the Log_2 signals of all the wells on the plate. These germ layer index values are averaged from replicated cultures (n=3) for each ECMP combination and displayed as a final index value for the germ line biomarker (μ_{germ}).

These averaged germ layer indices were subsequently compared to proliferation and pluripotency indices, forming a comprehensive heatmap cluster diagram in Figure 5A. In the cluster diagram, each row signifies an individual ECMP combination, and columns represent averaged proliferation indices, pluripotency indices (OCT3/4a and Nanog), and germ layer markers (Sox17 and T-Brachyury). Hierarchical clustering, utilizing Euclidean distancing and average linkage, discloses three distinct groups: 1) low pluripotency and high germ layer differentiation, 2) high pluripotency and low germ layer differentiation, and 3) a central cluster displaying non-partisan expression. This clustering effectively highlights the relationship between pluripotency and germ-layer differentiation is broad.

Correlation graphs further illuminate these relationships. Figure 5B shows a Pearson's correlation graph between Sox17 and T-Brachyury index values indicating a moderate positive correlation (r=0.4668, R2=0.1996, p=<0.0001), suggesting a potential preference for multi-lineage specification when ECMP signals encourage deviation from pluripotency. Due to the index values being calculated from images of multiple cells in a culture well, heterogenous populations of cells expressing endodermal and mesodermal markers is often observed. This correlation graph also shows data points that deviate from the trendline, indicating that some ECMP combinations influence a preference for Sox17 or T-Brachyury expression. Specific ECMP combinations, such as C1C3V, C1C3F, and C3C4, exhibit enhanced Sox 17 and expression and C1, C3, and C4 all showed enhanced T-Brachyury expression (Figure 5C and S5) signifying ECMPs influence on lineage commitment. Notably, C3C4FLV demonstrates a capability to promote multi-lineage specification by enhancing both T-Brachyury and Sox17 expression.

The hierarchical cluster also revealed distinct groups exhibiting either low pluripotency and high germ layer differentiation or high pluripotency and low germ layer differentiation. A central region, however, remains ambiguous, suggesting co-expression of pluripotency and germ layer markers or uncorrelated expression within the same well. Pearson's correlation between average pluripotency (μ_{Plu}) and germ layer (μ_{germ}), index values establish a moderate negative correlation (r=-0.4104, R2=0.1684, p=<0.0001) (Figure 5D), reinforcing the dynamic interplay between pluripotency and germ layer commitment. These findings provide valuable insights into the nuanced relationship among ECMP combinations, pluripotency, and germ layer differentiation.

Expression patterns of MESP1 and MLC2 isoforms predict optimal cardiomyocyte differentiation.

By narrowing the view on these 63 protein combinations, we find there are specific ECMP combinations that can promote germ layer differentiation while others promote pluripotency. To further probe cardiac lineage specification, we first explored several markers of cardiac progenitors including kinase insert domain receptor (KDR), which is used to signify a pre-cardiac mesoderm cell type (76). T-Brachyury^{+}/KDR^{+} cells can enter the cardiac lineage and express various genes and transcription factors as the cells become progressively differentiated. The regulation of multipotent cardiovascular progenitor cell specification can be observed through the enhanced expression of mesoderm posterior 1 (MESP1) (77). After immunostaining and hierarchical clustering analysis of KDR and MESP1 stained populations, alongside the SOX17 and T-Brachyury populations evaluated in the preceding section, we see a range of differential expression across all ECMPs. However, there is no significant correlation between the early germ layer and cardiac progenitor molecular markers (Figure S6-S12). While selecting ECMPs alone may promote germ layer specification and enhance cardiac progenitor markers, we believe that temporal administration of cardiac-promoting supplements is necessary for cardiac differentiation.

To evaluate how protein combinations may trigger cardiac lineage programs, we subjected our cultures to differentiation media conditions and immunostained for T-

Brachyury, KDR and MESP1. Figure 6 shows a cluster diagram constructed from the index values on all 63 ECMP combinations for T-brachyury, KDR, and MESP1 pre and post-differentiation. By performing hierarchical clustering, we can see the segregation of groups that correspond to high and low expression of both pre and post differentiation expression of MESP1, where the majority of the 28 ECMP combinations that showed positive index values for pre- and post-differentiation expression of MESP1 are represented in the bottom half of the cluster diagram. A correlation of MESP1 expression for pre and post differentiation shows a weak positive correlation in Figure S13 ($r=0.3243$ $R^2=0.1052$ $p=<0.0001$). When we isolate the 28 ECMP combinations that had a double positive MESP1 expression for pre and post differentiation, we see a tighter correlation that remains weakly positive ($r=0.2468$ $R^2=0.06090$ $p=0.0264$). This weak correlation is unsurprising because MESP1 expression is transiently expressed throughout differentiation. Nevertheless, it is still feasible that ECMP combinations that show positive expression of MESP1 in both pre and post differentiated cells will produce enhanced differentiation of cardiomyocytes and may positively influence cardiomyocyte maturation.

The indication of maturation is frequently associated with the manifestation of mature cardiomyocyte markers such as cardiac troponin (cTnT) (78). In the developmental phase of hearts, there is typically a higher demand for strongly contracting cardiomyocytes in ventricular tissue as opposed to atrial tissue due to the resistance and forces needed for effective blood ejection into the body. These two chambers develop alternate versions of the myosin light chains (MLC) denoted MLC2a and MLC2v. This transition is commonly associated with maturation in in-vitro cultures where the immature cardiomyocytes predominantly express the MLC2a gene, which undergoes a switch to the MLC2v isoform during maturation (79, 80, 81, 82, 113).It has since become standard practice to represent the expression of MLC2a to MLC2v as a comparison of maturation between groups where more matured groups display more MLC2v and less MLC2a (83, 123). To assess the maturation of the cardiomyocytes differentiated on our 63 protein combinations, we immunostained our cells for cTnT, MLC2a, and MLC2v on day 14 of the differentiation protocol and used the equation previously used (equation 3) to generate index values for the cardiomyocyte maturation biomarkers.

These index values are averaged from replicated cultures (n=3) for each ECMP combination (μ_{CMAT}). These averaged CMAT index values are compared to the proliferation, pluripotency, germline, and cardiac progenitor index values and are displayed in a heatmap cluster diagram in Figure 6. Hierarchal clustering shows that the double positive MESP1 ECMP combinations grouped in the lower half of the cluster diagram all show positive MLC2v expression, with the majority showing a strong negative MLC2a expression.

Surprisingly only a few shows positive cTnT expression in this same group. When looking at the cTnT expression, only two ECMP combinations show negative MLC2v expression suggesting that expression of cardiac troponin leads to the progressive maturation of cardiomyocytes. We expect to see a positive correlation when we compare the MESP1 expression for both pre and post-differentiation to these mature cardiac markers. Figure S13 shows this correlation of MESP1 with cardiac troponin, where no correlation is observed in both the pre and post differentiation MESP1

expression graphs, and the correlation of MLC2a with MESP1 for both pre and post differentiation. In both these graphs, we see a weak negative correlation, as expected. We would assume that expression of MESP1 would correlate with cardiac differentiation and maturation; thus, as MESP1 expression increases, we would see enhanced cardiac differentiation and a decrease in MLC2a expression. There is a positive correlation between MESP1 pre and post differentiation expressions with MLC2v, supporting the hypothesis that increased expression of MESP1 often leads to enhanced differentiation and maturation of cardiomyocytes as dictated by increased expression of MLC2v (Figure S14).

Select matrices that promote cardiomyogenisis and influence chamber specification

Following the completion of various biomarker stains and the examination of the impact of ECMP combinations on the expression of cardiac progenitor and maturation markers, our focus shifted to identifying the ECMP substrates capable of generating functional contracting cardiomyocytes. Out of the 63 protein combinations

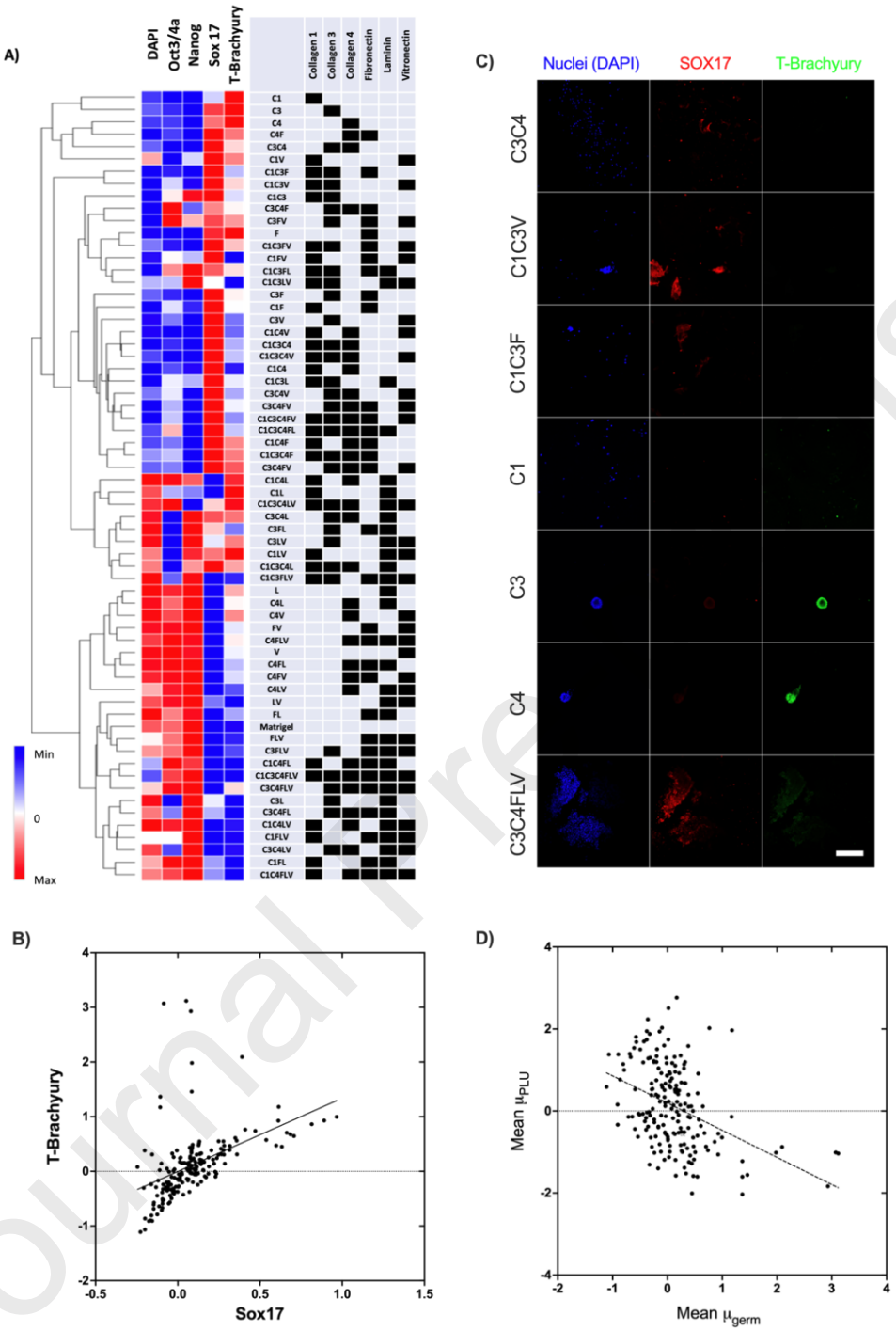

Figure 5. **Heat map of extracellular matrix proteins (ECMPs) combinations effect on human embryonic stem cell (hESC) proliferation, pluripotency, and germ layer differentiation**. **A)** Heat map of the mean proliferation index values (μ_{PRO}), mean pluripotency index values (μ_{Plu}), and mean germ layer index values (μ_{Germ}) for each ECMP combination (row). The ECMP combination is indicated with the protein name acronym and the shaded boxes in the table to the right of the heat map. **B)** Pearson correlation matrix of sox17 and T-Brachyury index values (r=0.4468 R^2= 0.1996). **C)** Images showing the high sox17 and low T-Brachyury expression on C3C4, C1C3V, and C1C3F protein combinations, low sox17 and high T-Brachyury expression on C1, C3, and C4 protein combinations, and the dual expression of sox17 and T-Brachyury on C3C4FLV. Corresponding immunocytochemical stain DAPI (blue), Sox17 (Red), and T-Brachyury (green) scale bar is 100μm. **D)** Pearsons's correlation between the mean pluripotency index values (μ_{PLU}) and the mean germ layer index values ((μ_{Germ}) for all 63 combinations (r= -0.4104 R^2= 0.1684).

tested, along with the Matrigel control group, 20 exhibited the presence of

contracting cardiomyocytes. Figure 7 displays confocal images depicting the observed biomarker stains for each of these 20 ECMP combinations.

Given the extensive collection of confocal data, we thought it appropriate to conduct a principal components analysis (PCA) to explore potential clustering among the ECMP combinations that induced contracting cardiomyocytes compared to those that did not. In Figure 8, the PCA graph displays all 63 protein combinations and the Matrigel control groups in triplicate. Although a slight clustering effect of ECMP combinations resulting in contractions is observed on the left side of the graph, it is not distinctly separated from the non-contracting group. The principal components primarily contributing to the separation of the contracting from the non-contracting groups are MESP1 (both pre and post differentiation) and MLC2v. Moreover, groups such as pluripotency, T-brachyury, and MLC2a are crucial for distinguishing non-contracting groups (Figure S15B). When evaluating the supporting graphs for the PCA plot (Figure S15C and D) we found it to be the wrong choice for distinguishing differences between the contracting and non-contracting groups. As this plot doesn't clearly distinguish between the two groups, we explored an alternative dimension-reduction method called t-distributed stochastic neighbouring embedded (t-SNE). Figure 8B shows the t-SNE graph for all 63 ECMP combinations and the control group, offering a visual representation of potential clusters with distinct characteristics. While t-SNE is not a statistical tool, it color-codes ECMP combinations according to contracting and non-contracting groups, revealing a significant crossover between the two. Unlike PCA plots, t-SNE displayed a distinct tight cluster of contracting cells separated from the main data body (highlighted with a circle). To account for variable parameters, we produced the same cluster plot with different perplexity values (0-50), that consistently showed the same small tight cluster of contracting cells (Figure S16). This suggests that the ECMP combinations within this cluster had unique values setting them apart from other contracting and non-contracting data points. The ECMP combinations in this cluster—C1C3FLV, C3C4FV, and C1C3C4V—stand out in the cluster diagram (Figure 6), grouped at the bottom, indicating similarities in the expression of mesoderm, cardiac progenitor, and cardiomyocyte maturation markers. Notably, the MESP1 post-differentiation and MLC2v index values are highly expressed above the global average mean in these three ECMP combinations.

Upon identifying three distinct ECMP groups (C1C3FLV, C3C4FV, and C1C3C4V) that formed a separate cluster from the main dataset, we conducted a series of a-priori statistical tests to determine if these three groups exhibited statistically different biomarker expressions compared to the control group on Matrigel™. The null hypothesis stated that all biomarker expressions in hESC were equal when cultured on Matrigel™ and the three specified ECMP combinations. To assess the statistical significance of any differences, we employed a MANOVA test, allowing for the examination of multiple variables. The selected biomarkers for this analysis were T-brachyury, KDR, MESP1, cTnT, MLC2a, and MLC2v. These biomarkers were chosen due to their relevance in highlighting key stages of cardiomyocyte lineage specification, encompassing germ layer differentiation, cardiac mesoderm, cardiac progenitor, and mature cardiomyocyte protein expression. The MANOVA test yielded a significant difference among the four groups, as indicated by a Pillai's Trace value of 2.5068, $F(18, 15) = 4.2354$, and $p = 0.0035$. Consequently, we reject the null hypothesis, concluding

that there is a significant disparity in biomarker expression levels between the Matrigel™ and ECMP combinations. Further details on these statistical tests are available in the supporting methods.

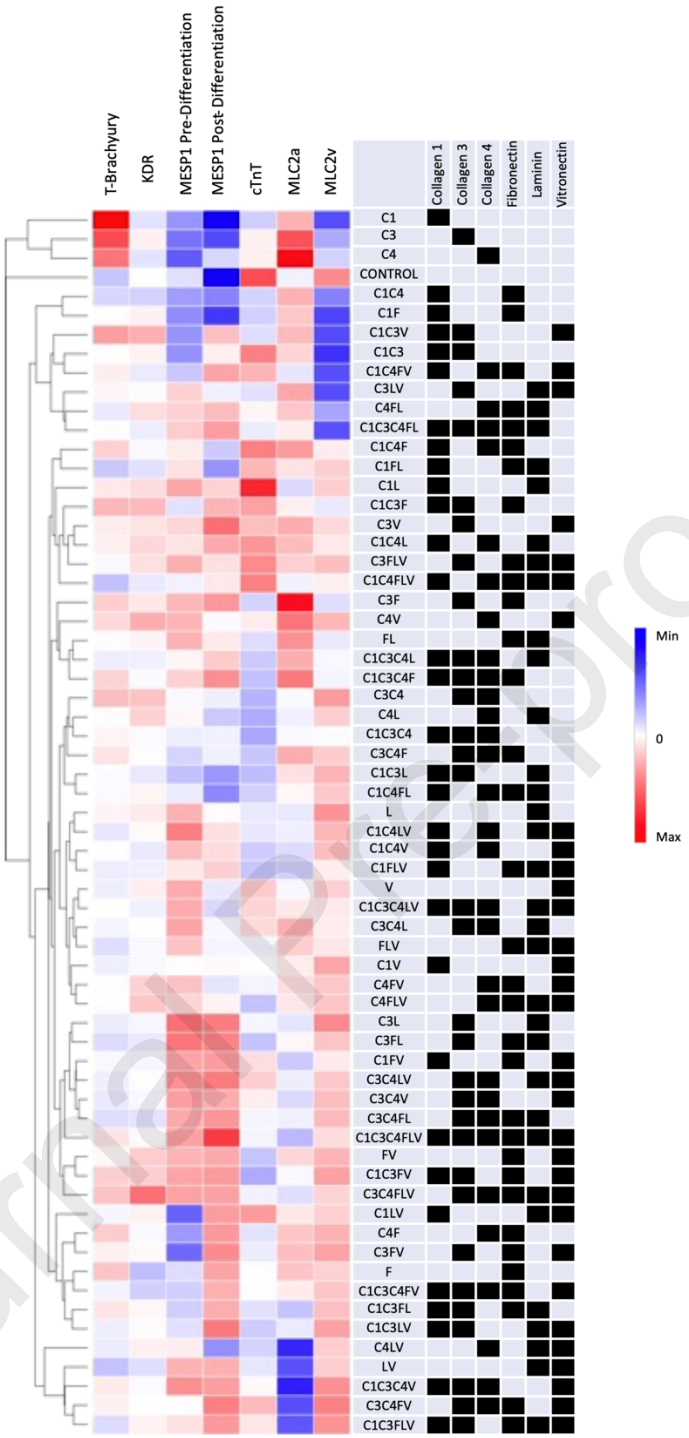

Figure 6. **Extracellular matrix proteins (ECMPs) combinations effect on human embryonic stem cell (hESC) germ line, cardiac progenitor, and mature cardiac biomarker expression.** Heat map of average expression index values for each biomarker (column) on the individual ECMP combination (rows). Three independent array cultures were conducted for each biomarker. The ECMP combination is indicated with the protein name acronym and the shaded boxes in the table to the right of the heat map. A hierarchical clustering was performed with a Euclidian distancing metric and an average linkage method. High (red) and low (blue) data points are referring to the averaged index values around the global average mean (0).

Next, we sought to explore the contractile properties of these differentiated cells to examine the early-stage changes in the contraction profile. This was achieved with high-speed optical mapping of the contracting cardiomyocytes that are then analyzed

using Pulse Video Analysis software from CuriBio (84). The electrophysiological and kinetic characteristics of cardiomyocytes serve as essential indicators for identifying chamber specification based on the action potential (AP) morphology. Distinct cardiac cell types exhibit unique ways of propagating the action potential (14, 29, 85). While textbook definitions exist for these chamber-specific action potential morphologies, practical observations often reveal a spectrum of morphologies both in vivo and in vitro. This variability can be attributed to factors such as the chosen location to measure the electrophysiological activity in the heart or the presence of multiple cell types within the same culture dish. Notably, atrial, and ventricular waveforms exhibit a range of morphologies when measured from different locations or at different depths within the heart wall (86, 87).

Despite these variances, we have tried to develop a template criterion that could be used to identify chamber-specific AP morphologies based on structural, electrophysiological, and biomarker characteristics (See Table S1). To effectively identify AP morphology, we must determine the speed of the different phases that make up the action potential duration (APD) as well as the time difference between distinct regions of the ADP – these are often written as ADP followed by a number to signify the time difference between a percentage of the contraction time and the pairing percentage on the relaxation time. This type of analysis is often referred to as the indices of triangulation and can help identify chamber-specific cell types through discrete characteristics. For example, nodal cells often have a slow AP velocity when performing patch clamping (88, 89). We predicted this to be ~5-10μm/s from the data collected of the AP morphologies of the 20 groups of contracting cardiomyocytes. Nodal cells often lack an early repolarization phase and show a plateau in the repolarization phase so as not to induce quick repolarization in surrounding atrial tissue (90). The characteristics of the repolarization phase of nodal cells show an APD50 and APD90 of 100 and 150 ms, respectively, with the indices APD50/APD90 and APD90-APD50 of approximately 0.6 and 50 ms, respectively (88). Additionally, the ratio of APD30-40/APD70-80 will show roughly 0.65 (29).

Owing to their imperative role in rapidly transmitting electrical signals, conductive cells exhibit a notably swift upstroke velocity, calculated to exceed 100 μm/s (91). These cells share a repolarization phase, akin to ventricular myocytes but with a lower amplitude, this feature is attributed to their close proximity in vivo (91, 92). Notably, conductive cells demonstrate extended action potential durations, with APD50 and APD90 measuring approximately ~220 ms and ~300 ms, respectively (92). Key indices such as APD50/APD90 and APD90-APD50 are estimated to be around 0.7 and 80 ms, respectively (91). Our calculations indicate that the ratio of APD30-40/APD70-80 should fall within the range of 0.6–0.8.

Atrial cells typically exhibit an intermediate action potential (AP) velocity, falling between nodal and ventricular cells, with our calculations indicating this to be approximately 20 μm/s (93, 94). In general, atrial cells are characterized by a lack of a plateau phase and a more triangular AP morphology. The variability in AP morphologies of atrial cells introduces a considerable window for triangulation indices. The repolarization phase for atrial cells may exhibit an APD50 and APD90 values around 25 ms and 200 ms, respectively, although other studies report APD50 and APD90 closer to 200 ms and 400 ms, respectively (95, 96, 97, 98). Consequently, repolarization indices such as APD50/APD90 and APD90-APD50

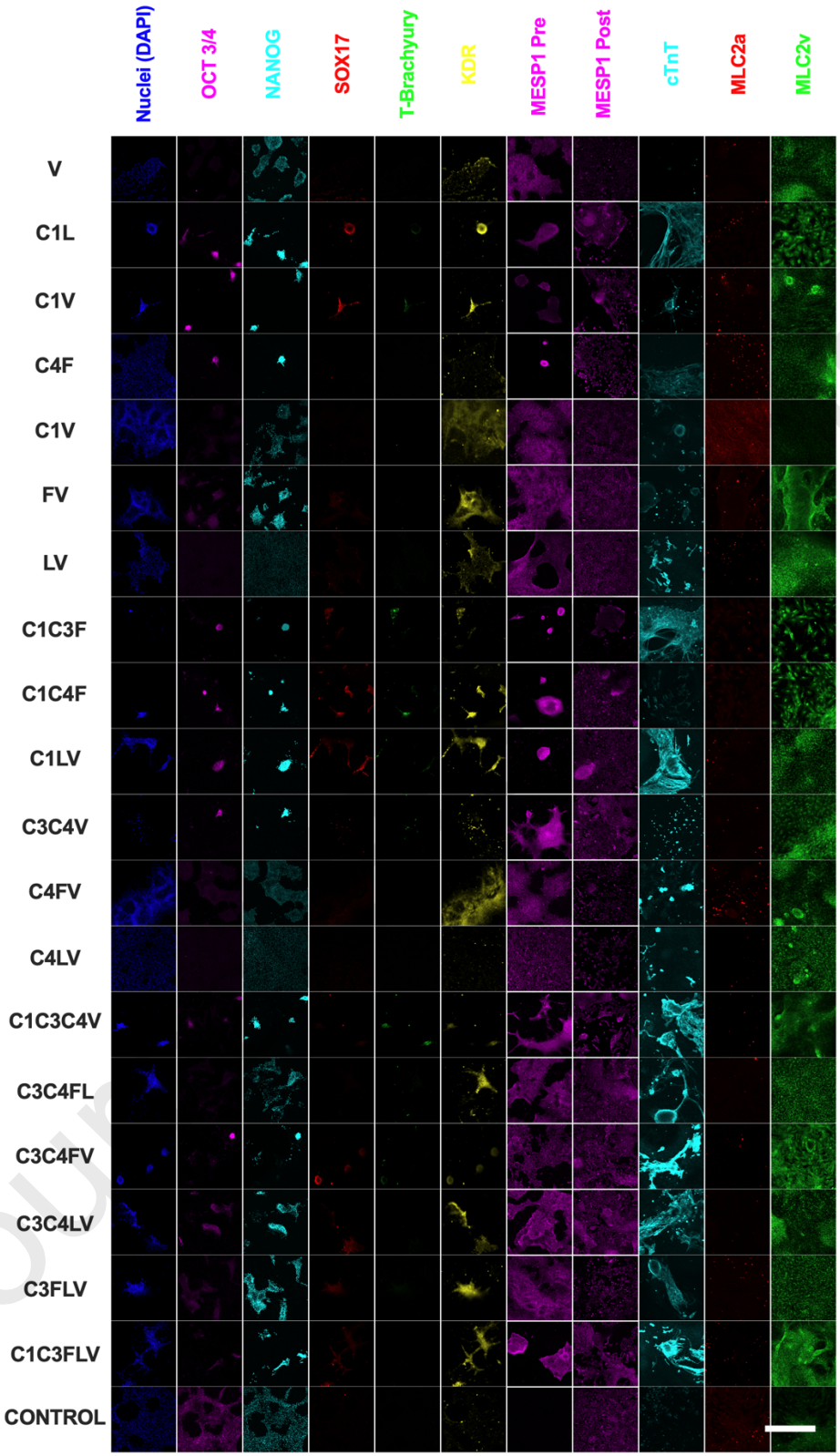

Figure 7. Confocal images of extracellular matrix protein (ECMPs) combinations effect on human embryonic stem cell (hESC)expression of pluripotency, germ line, cardiac progenitor, and mature cardiac biomarker expression. Corresponding immunofluorescent stain DAPI (blue), Oct3/4a (Magenta left) Nanog (cyan Left) Sox17 (red left), T-Brachyury (green left) KDR (yellow), Mesp1 Pre and Post differentiation (Magenta center), and cTnT (cyan right), MLC2a (red right), MLC2v (green right), scale bar is 100μm.

also exhibit a range between 0.2-0.5 and 175-200 ms, respectively (96, 98). Additionally, the ratio of APD30-40/APD70-80 is estimated to have a value of

approximately 0.7-0.9 (29).

Ventricular myocytes are characterized by their predominant expression of MLC2v over MLC2a. These cells exhibit a highly organized structure and often display faster action potential (AP) velocities similar to conductive cells, with our calculations indicating a velocity of approximately 70-100 μm/s (92, 99). Ventricular cells are renowned for their distinct plateau phase, a feature reflected in their repolarization indices. Given the greater thickness of ventricular tissue compared to atrial tissue, the AP morphology of ventricular cells can vary based on their location, whether towards the epicardium or the internal chamber. Midmyocardial tissue may report APD50 and APD90 values of 200 ms and 270 ms, respectively, while ventricular cells closer to the epicardium may exhibit APD50 and APD90 values of 300 ms and 400 ms (92, 99). This variability results in a range for repolarization indices such as APD50/APD90 and APD90-APD50, estimated to be 0.65-0.85 and 50-130 ms, respectively (99, 100). Additionally, the ratio of APD30-40/APD70-80 is anticipated to have a value of approximately 0.8-1.0 (29).

We conducted an optical mapping study on the 20 ECMP combinations that induced cardiomyocyte contractions, and the results are displayed in Figure 9 and Figure S17. Particularly focusing on the three ECMP combinations (C1C3FLV, C3C4FV, and C1C3C4V) identified in the t-SNE graph in Figure 8B for their enhanced maturation characteristics, we observed that all three of these ECMP combinations exhibit similar or improved contraction profile characteristics compared to the control group. This conclusion is based on several key observations. Beat rate variation in these three ECMP groups tends to be lower than in the control group and are significantly different in the C3C4FV group (t-test P=0.0067). These lowered beat rate variations indicate a more established contraction frequency and a reduced likelihood of competing pacemaker regions. While two of the three ECMP groups

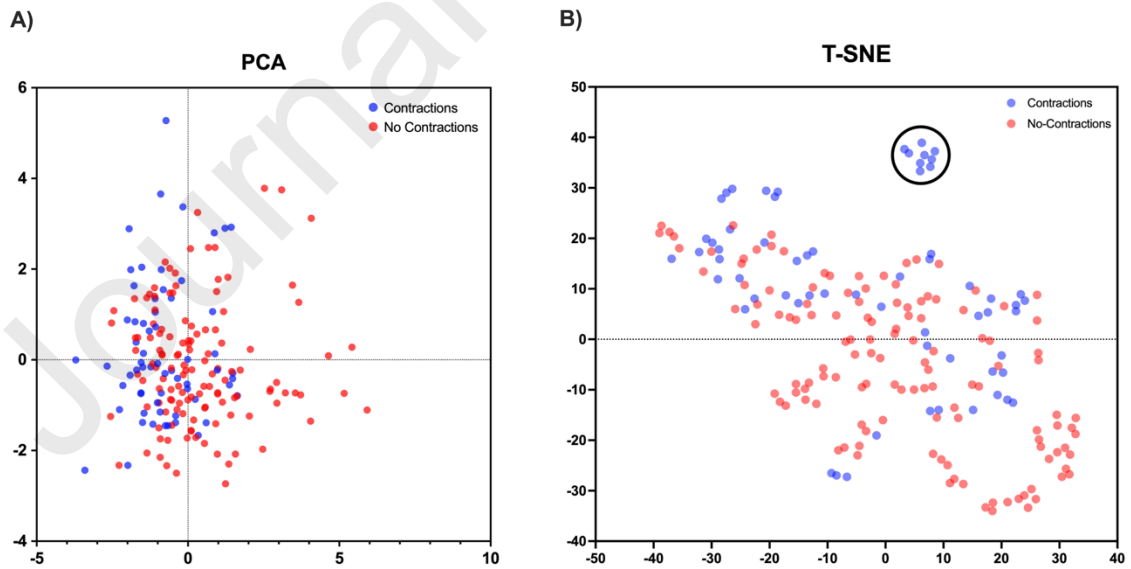

Figure 8. Principal component analysis (PCA) and T-distributed stochastic neighbor embedding (T-SNE) of biomarker index data from hESC cells on 63 ECMP combinations and a Matrigel control group. A) Data points are separated into two groups, the ECMP combinations that produced contracting cardiomyocytes (blue dots) and those ECMP combinations where no cardiomyocytes were observed contracting (red dots). B) t-distributed stochastic neighbor embedding plot. Data points are separated into two groups, the ECMP combinations that produced contracting cardiomyocytes (blue dots) and those ECMP combinations where no cardiomyocytes were observed contracting (red dots).

show a similar contraction velocity and contraction duration to the control group, the C3C4FV group shows a significantly lowered contraction velocity and a significantly increased contraction time. In addition, there is a significant difference between the

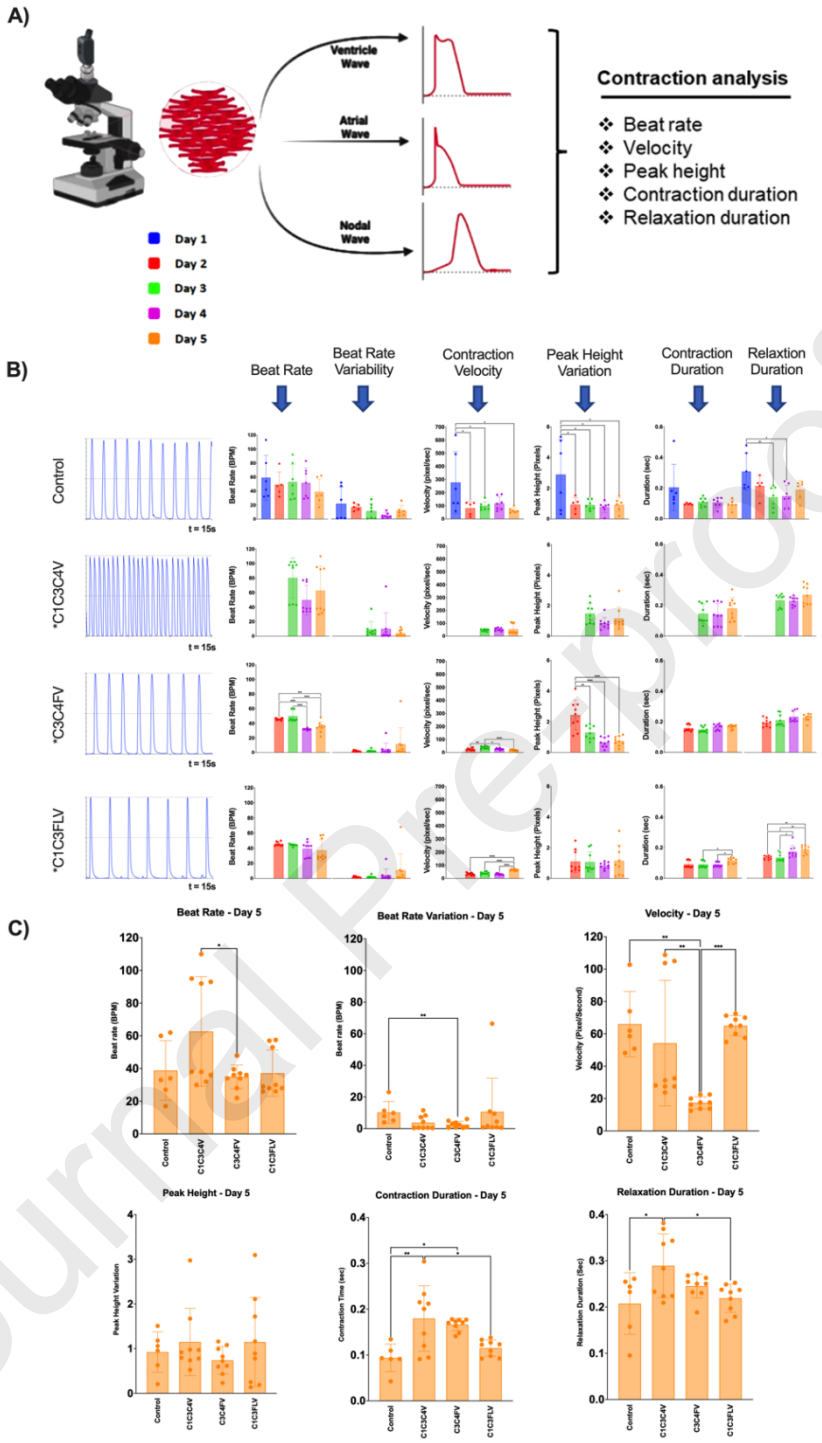

Figure 9. **Contraction Profiles for top three ECMP combinations that produced contracting cardiomyocytes and the control group.** A) ECMPs featuring contracting cardiomyocytes are optically mapped using a high-speed microscope to compare action potential (AP) morphologies. B) AP morphologies for ECMP combinations for the top three with the control group. The left panel shows the normalized peak height contraction profiles for each ECMP combination as derived from high-speed videos. These profiles are from videos taken on day 5 and are representative average of 9 independent videos taken. The bar charts on the right show the beat rate, beat rate variation, contraction velocity, peak height variation, contraction duration, and relaxation duration of the cardiomyocytes measured over a five-day period. C) Statistical analysis of contraction metrics for select formulations compared to controls. These mean values are averaged from three independent regions within the culture well with videos taken in triplicate with a ten-minute interval between each recording round. * P value < 0.05, ** P value < 0.01, *** P value < 0.001.

means of the relaxation times of the control and ECMP groups when performing a one-way ANOVA (P=0.0133). The increased contraction velocity, contraction time, and reduced beat rate variation suggest that cardiomyocytes in these ECMP groups possess a more matured phenotype, possibly due to increased ion channel distribution, and or, improved sarcomere alignment which enhances their ability to control the repolarization phase. The increased relaxation duration also implies a more matured phenotype with increased ion channel density and distribution but could also indicate improved retention of calcium in the sarcoplasmic reticulum and improved calcium handling through ion channels in these ECMP groups. The discovery of the reasons for the improved contraction profile metrics falls outside the scope of this study but is an exciting area for future research.

The characterization of cardiomyocyte AP morphology on the 20 ECMP combinations was conducted using the criteria list we developed in Table S1. By applying this criteria list, we assigned a chamber specification to each of the 20 ECMP combinations, as outlined in Table S2. Subsequently, we generated PCA and t-SNE graphs using the AP morphology data derived from the optical mapping study (see Figure 10). The PCA graph reveals a random distribution of data points without significant clustering. However, when colour-coded based on their assigned chamber specification, evidence of clustering emerges, with certain areas indicating potential crossover between groups. Notably, the scree plot illustrates an elbow for two principal components, and the proportion of variance exceeds the 80% threshold on the first principal component (figure S18). When we generated the t-SNE graph for the AP morphology data we saw a similar separation of data points grouping into the chamber specifications we assigned them. To ensure this data was accurate we replicated the t-SNE graph and adjusted the perplexity value between 0-15 to ensure the grouping of data points was consistent (Figure S19). Collectively, this data underscores how the combined analysis of molecular markers and contraction

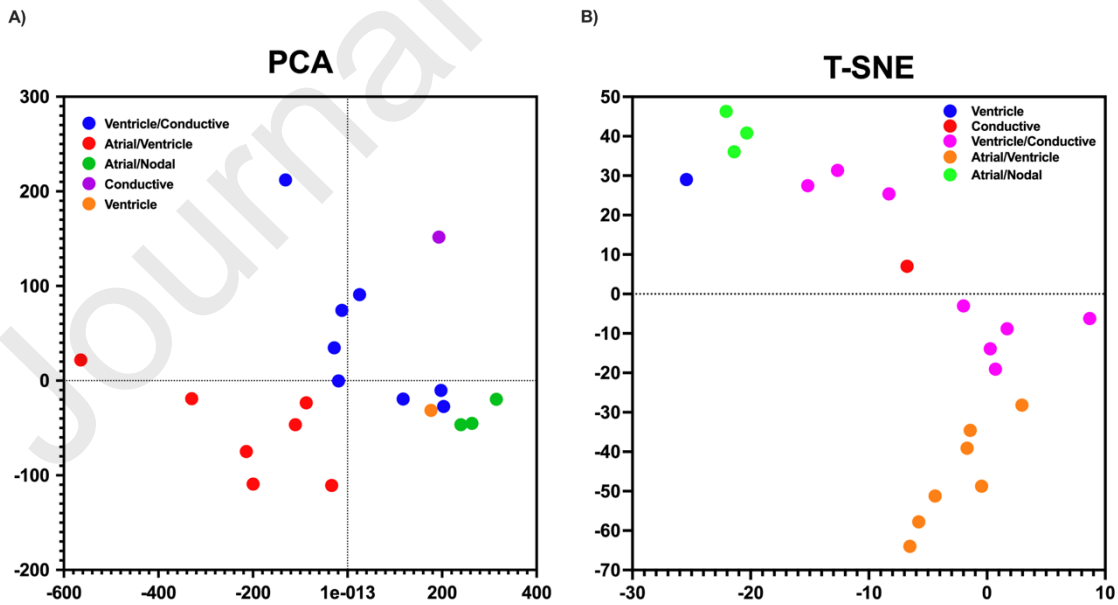

Figure 10: Principal component analysis (PCA) and T-distributed stochastic neighbor embedding (T-SNE) plot of chamber specifications A) Principal component analysis of all AP morphology measurements for all 20 contracting ECMP combinations. Data points are separated into chamber specific groups, B) t-distributed stochastic neighbor embedding plot of all the 20 AP morphology characteristics. Data points are separated into chamber specific groups.

optical mapping can reveal subtle differences in cardiac lineage specification. We believe this demonstrates that specific ECMP combinations have the potential to influence chamber-specification during cardiac differentiation.

Discussion

In this study, we developed an ECMP array to identify how individual proteins and their combinations can influence the proliferation and pluripotency of hESC. We then built on this platform to identify how specific ECMP combinations can aid cardiac differentiation and influence chamber specific characteristics. Previous studies have demonstrated that hESC can show preferences for certain protein combinations for the maintenance of pluripotency similar to commercial substrates (57, 59, 101). These studies highlight that there are specific ECMP combinations that can maintain the pluripotency of stem cells for long period in culture and thus alludes to the possibility that alternative ECMP combinations could direct cell fate. The number of literature sources investigating the benefits of ECMP combinations on maintaining stem cell's pluripotency highlights stem cells can be maintained on various ECMP combinations but also indicates that this could be a cell line-specific behaviour. Here we screened 63 ECMP combinations and identified a preference for laminin, vitronectin, collagen I and collagen IV (C1C4LV) for our H9 hESC which displayed good expression of pluripotency markers and consistent proliferation rate compared to Matrigel™. We also demonstrated that hESC on this ECMP combination could reach 80% confluency. while maintaining similar cell morphology and differentiation efficiency when compared to cultures on Matrigel™. When the C1C4LV combination was compared to ECMP combinations with one or more of these ECMP removed, we identified the importance of collagen I and collagen IV, as removal of the collagens negatively affected proliferation and pluripotency. Our study also revealed that whilst certain ECMP combinations could maintain pluripotency, others could increase expression of markers associated with specific germ layers, and hence might influence lineage specification.

The downregulation of pluripotency markers, indicates certain ECMP combinations may induce germ-line differentiation of hESC. Furthermore, specific ECMP combinations can influence precise germline differentiation lineages and even enhance cardiac progenitor markers. In many cases, ECMP promoted dual lineage expression of Sox17 and T-brachyury, indicating simultaneous expression of endoderm and mesoderm markers, which we denoted as mes-endodermal populations. This phenomenon was particularly evident in cells cultured on C3C4FLV, which exhibited enhanced co-expression of Sox17 and T-brachyury. However, we also observed instances of single germline expression, with mesoderm lineage expression occurring when cells were cultured on single collagen groups (C1, C3, and C4), while endoderm marker expression alone was promoted in more complex combinations (C1C3V, C1C3F, and C3C4). Analysis of cardiac progenitor markers KDR and MESP1 revealed positive correlations between each marker and the mesoderm marker T-brachyury. Therefore, our array-based approach successfully identified ECMP combinations capable of directing pluripotent stem cell populations toward specific germ lineages and the enhanced expression of cardiac progenitor markers. Whilst these results seemed promising ECMPs alone were not

able to induce cardiac differentiation to produce contracting cardiomyocytes without the addition of soluble lineage-promoting factors.

Upon subjecting the hESC cultured on the ECMP combinations to a cardiomyocyte differentiation protocol, we observed the derivation of cells exhibiting cardiac progenitor characteristics, characterized by heightened expression of KDR and MESP1. These progenitor cells were more inclined to produce cardiomyocytes with enhanced expression of maturation biomarkers. We conducted a hierarchal clustering analysis on the index values (refer to Figure 6) associated with T-brachyury, KDR, and MESP1 both pre and post differentiation. This analysis revealed distinct clusters, with MESP1- (pre and post) combinations prominently positioned at the top and MESP1+ (pre and post) combinations clustered towards the bottom. Immunostaining for maturity markers, including cTnT, MLC2a, and MLC2v, unveiled specific combinations exhibiting elevated MESP1, cTnT, and a high ratio of MLC2v:MLC2a - a characteristic indicative of a mature phenotype in vitro.

Further statistical analysis of cardiac-specific markers across all 63 ECMP combinations pinpointed unique clusters - C1C3FLV, C3C4FV, and C1C3C4V - on the t-distributed stochastic neighbor embedding (t-SNE) plot. These combinations demonstrated optimal characteristics for fostering cardiomyocyte differentiation. Video analysis provided additional insights, revealing that 20 out of the 63 ECMP combinations induced robust contraction post-differentiation, including the three optimal matrices mentioned above. To refine our findings, we developed a custom chamber specific criterion list, incorporating our experimental data and insights from existing literature (refer to Tables S1 and S2). The criteria list in these tables combined expression data, AP morphology data, and morphological information which we used to predict the chamber specification of the contracting cardiomyocytes generated on each of the 20 ECMP combinations. When we performed subsequent PCA and t-SNE analysis on the AP morphology data gathered from the 20 ECMP combinations, we found an accurate alignment between our predictions and the clustering of groups (refer to Figure 10).

Although the cardiac differentiation pathway is well defined in the literature with a variety of protein biomarkers that can indicate the stage of differentiation (refer to Figure 1), we discovered certain combinations of ECMP that favour the expression of cardiomyocytes that don't necessarily align with expected biomarker expression pathways. Biomarker expressions for the early stages of differentiation showed us that many of the ECMP combinations promoted co-expression of seemingly conflicting biomarkers in the same well (such as the endoderm maker sox17 with the mesoderm marker T-brachyury). Throughout our study, we investigated the expression of ten well-known biomarkers in the cardiomyocyte differentiation lineage. We acknowledge that we did not investigate the specific influences the ECMP had on the heterogeneity of cell types which will be an important undertaking in future translation of our approach. Whilst modern cardiac differentiation protocols have had success in producing cardiomyocytes that could potentially be used in pharmacological testing and cell therapies, it is apparent that the next stage of differentiation protocols will need to utilise refined protein substrates to ensure consistent purity of cardiomyocyte populations with desirable functional characteristics.

Conclusions

In summary, we employed our ECMP microarray to investigate the differentiation potential of hESC on ECMP combinations that differ from commercial substrates. This endeavour lead to the discovery of ECMP combinations that promote various aspects of pluripotency and proliferation and others that help guide cardiomyocyte differentiation. Integrating this array approach with modern cardiac differentiation protocols allowed us to systematically assess cardiomyocyte lineage specification across different ECMP combinations and revealed specific matrices that enhance cardiomyocyte maturation and guide differentiation to chamber-specific cell types. Our findings tell us that future explorations of how the ECMP substrate influences chamber-specific differentiation should investigate the intricate interplay ECMP have in promoting non-cardiac lineages to better understand the effect this has on the maturation and chamber specification of cardiomyocytes. This exploration holds the promise of significantly improving our understanding of cardiac differentiation methodologies, contributing not only to the enhanced precision of cardiac models in safety pharmacology but also facilitating the development of improved cell therapies in the pursuit of a cure for cardiac disorders. Furthermore, this platform will prove useful for development of cultureware for cell production and manufacturing, with scope for precise matrix formulations serving to complement advanced bioreactor technologies, where dynamic mechanical and electrical stimulation can be employed for further cell and tissue maturation.

Material and Methods

Array Fabrication

Collagen 1 (Advanced Biomatrix, #5007) and collagen 3 (Advanced Biomatrix, #5021) are received in solution at a concentration of 3mg/mL and 1mg/mL, respectively. We immediately dilute both collagen solutions down to 25µg/mL in 0.01mol HCL solution in

DPBS prior to coating culture surfaces. Collagen 4 (Advanced Biomatrix, #5016) is received as 5mg powder. We reconstitute the collagen 4 powder by adding 5mL of cold 0.25% acetic acid (Chem Supply Pty Ltd Australia, AA009) and mixing through gentle pipetting. We then incubate the reconstituted powder at 2-8oC with gentle swirling. We then dilute the 1mg/mL solution down to 25$\mu g/mL$ in 0.25% acetic acid immediately prior to coating culture surfaces. Fibronectin (ThermoFisher Scientific, #33016015) is received as a 5mg lyophilized powder. We reconstitute the powder by adding 5mL of warmed sterile 1X DPBS and allow it to dissolve at 37oC for 30 minutes. Any undissolved material can be gently separated apart with sterile stainless-steel forceps until fully dissolved. Reconstituted fibronectin is then aliquoted into 25µL volumes and stored at -20oC. Fibronectin is thawed and diluted to 25$\mu g/mL$ in 1mL of sterile DPBS immediately prior to coating culture surfaces. Laminin (ThermoFisher Scientific, #23017015) is received as a 1mg/mL solution in

0.15M NaCl. To avoid repeated freeze/thaw cycles, the laminin is aliquoted into 25µL

volumes and stored at -20oC. Laminin is thawed and diluted to 25$\mu g/mL$ in sterile 1x DPBS prior to coating culture surfaces. Vitronectin (ThermoFisher Scientific, #A14700) is received as a solution at a concentration of 0.5mg/mL. To avoid

repeated freeze/thaw cycles, vitronectin is aliquoted in 50µL volumes and stored at -80oC. Vitronectin is thawed and the 50µL volume is diluted to a concentration of $25\mu g/mL$ in 1mL of sterile 1x DPBS prior to coating culture surfaces.Proteins were distributed in a 96-well plate - Corning 96 well TC-treated Microplates (Merck Australia, CLS3997) using a manual 200uL micropipette following the schematic in figure 2. Matrigel-coated wells were prepared using Corning Matrigel™ hESC-Qualified Matrix, LDEV-free (Corning, 354277, Lot# 1236001). Matrigel was diluted with a dilution factor of $10.84\mu L/mL$ in Gibco BenchStable DMEM/F12 (ThermoFisher Scientific Australia, A4192002) and dispensed at $85\mu L/well$. Before seeding, the 96-well plate was placed in a humidified incubator set to 37°C and 5% CO2. Plates are either immediately seeded following incubation or are wrapped in parafilm and tin foil and stored at 4°C for up to 5 days.

Stem Cell Culture

The H9 hESC culture media was mTeSR™ Plus Basal Medium supplemented with mTeSR™ Plus 5x supplement (StemCell Technologies, #100-0276). Cells had media exchanged daily and are passaged weekly in $50\mu m$ colonies by gentle dissociation with ReLeSR™ (StemCell Technologies, #05872) for 5 minutes at 37°C followed by gentle tapping of the culture dish. Cell clusters are then collected with a wide-mouth 2mL serological pipette and are agitated by gentle vortexing until most colonies measure ~$50\mu m$ (observed under a microscope). hESC are passaged onto the ECMP array as single cells by exposure to Accutase™ (StemCell Technologies, #07920) for 5 minutes at 37°C followed by centrifugation at 300g for 3 minutes. Cells are re-suspended in culture media supplemented with the RHO/ROCK pathway inhibitor Y-27632 (StemCell technologies, #72304) at a final concentration of 5 $\mu M/mL$. hESC are seeded directly into the ECMP array at a seeding density of $1.24x10^4\ cells/cm^2$ and incubated in Y27632 supplemented media for 24hours before washing and replenished with culture media.

Staining, Imaging, and Analysis

Fixing: Culture media is aspirated, and cells are fixed in 4% PFA for 20 minutes. **Permeabilize:** Fixed cells are then permeabilized in 0.1% Triton X-100 diluted in DPBS at room temperature for 30 minutes. **Blocking:** Cells are blocked by incubation in 1% BSA at room temperature for 15 minutes. **Primary antibodies:** primary antibodies used in this study are listed in supplementary table S3. Cells are stained using antibodies diluted 1:300 in 1% BSA and incubated for 24 hours at 4°C. Primary antibodies are washed away by one wash in DPBS followed by 2x15minute incubations in DPBS. **Secondary antibodies:** secondary antibodies used in this study are listed in supplementary table S3. Cells are stained using antibodies diluted 1:300 in 1% BSA and incubated for 24 hours at 4°C. Secondaries are then washed away by 1x wash in DPBS followed by 2x15minute incubations in DPBS. Unless nuclear material is stained with Hoescht 33342 (ThermoFisher Scientific Australia, 62249), all cells are then mounted by inversion onto VECTASHEILD antifade mounting medium with DAPI (Fisher Scientific, NC9524612) and sealed with clear

nail polish. Confocal imaging was performed on the Zeiss LSM 800 with an inverted Axio Observer Z1 with two multi-alkali (MA) PMT (typical QE 25%) detectors. The microscope settings were as follows: objective 20x with a 1x crop area, pinhole 460µm, scan speed 0.52µs/pixel, 1024x1024pixel image with 2x averaging line-by-line single-directional mean intensity 8bit format. Images were collected using the following detection mirror settings Hoechst33342 & DAPI (400-496nm), Alexa Fluor™ 488 & ATTO 488 (490-583nm), CF™ 555 & Alexa Fluor™ 594 (594-637nm), Atto 647N & CF™ 647 (647-700nm). Fluorophores were excited using the following light sources: 405nm (3.5%), 488nm (4.5%), 561nm (4.5%), and 640nm (5%), respectively. To eliminate crosstalk between channels, the images were collected sequentially. The maximum intensity of images was attained by gain alterations to a point just below saturation in the brightest images, with settings maintained across all samples.

Cardiac Differentiation

H9 hESC cultured at a seeding density of $1.24x10^4\ cells/cm^2$ would reach confluency on day 5 (120h) when seeded onto the Matrigel-coated wells. H9 hESC on the ECMP combinations had varying confluency levels on day 5 (120h). When the differentiation protocol starts, we denote this day as day 0 as a reference for the following steps. On day 0, all cells' media was exchanged for the differentiation media RPMI (ThermoFisher Scientific AU, 11875093) supplemented with 2% B27 Minus insulin (ThermoFisher Scientific AU, A1895601). The cells were treated with GSK3b inhibitor CHIR-98014 (StemCell Technologies AU, 73042) at a concentration of 0.8µM. At exactly 24 hours (day 1) the differentiation media is aspirated and cells were washed with fresh differentiation media. The culture wells are then replenished with differentiation media and cells are left for 48 hours (Days 1 – 3). On day 3 50% of the culture media is aspirated and replaced with fresh differentiation media supplemented with the Wnt-inhibitor Wnt-C59 (Trocis, 5148) at a concentration of 2µM in the final volume. Cells are then incubated for 48 hours (days 3-5). On day five, culture media is aspirated and replenished with fresh differentiation media and cells are left to incubate for 48 hours (Day 5-7). On Day 7, cell media is aspirated and replaced with RPMI supplemented with B27 x50 (ThermoFisher Scientific AU, 17504044). Cells receive media exchanges every 2 days after day 7 with the RPMI media supplement B27 x50. Cardiomyocyte contractions tend to initiate around day 10 of the differentiation protocol and can be kept for long periods in incubation. The cells were incubated at 37°C in a humidified atmosphere with 5% CO2.

High-Speed Camera

Cardiomyocyte contractions were captured on a Zeiss Observer Z1 Spinning disk and TIRF microscope. The microscope is fitted with a temperature-controlled microscope enclosure and stage insert with CO_2 flow regulator. It also featured a motorized stage and Hamamatsu ORCA-FLASH 4.0 Digital CMOS Camera. This setup made it possible to perform long-term live-cell imaging experiments. The microscope settings were as follows: objective 4x with a 1x crop area, temperature setting of 37oC and 5% CO2. Images and video of contracting cardiomyocytes were

taken with a frame rate of 100 fps with variable contrast for 15 seconds to generate 1500 framed .AVI files. A motorized stage was used to create a list of 5 different locations of contracting cardiomyocytes in each culture well; these locations had 3 videos taken with at least 5 minutes between video captures and were repeated daily for a period of 5 days. Contraction data was gathered using the high-speed video analysis platforms, Pulse Video Analysis software (84) and the MUSCLEMOTION plugin for ImageJ (102). The Pulse Video Analysis software is a web-based portal that requires uploading the 15 second .AVI files and setting the parameters on the webpage as follows: frame rate set at 100fps, select type of video analysis set to contractility (brightfield), remove noisy signals set to yes. The upload option then allows for the specification of groups meaning all videos for a particular day, culture plate, and experimental parameters can be listed. This grouped upload allows for a streamlined analysis as automatic averaging of all parameters in each group is performed. The data files that are generated are separated for each video. The individual videos are divided into 25 quadrants and for each quadrant, a contraction and velocity trace are plotted and given in both data and graphical form. In addition, an image of the video's visual field is provided with a description of the active quadrants (areas of contractility) grouped based on their similarity in contraction profile. Finally, a summary document is provided that shows the profile metrics for each quadrant. The metrics measured include Beat Rate (bpm), Minimum Beat Rate (bpm), Maximum Beat Rate (bpm), Beat Rate Variation, Velocity (pixels/sec), Contraction Displacement (pixels), Peak Height Variation, Duration 75% (sec), Duration 50% (sec), Contraction Time (sec), Relaxation Time (sec), and Prevalence (%). The high-speed videos were also analyzed using the MUSCLEMOTION plugin for ImageJ which was downloaded from the following link (https://www.ahajournals.org/doi/suppl/10.1161/CIRCRESAHA.117.312067). This software stipulates the parameters for video quality with a minimum frame rate of 75fps, adequate lighting and contrast, and a .AVI or .TIFF file type. The limitations of this software include the computer's hardware in which the analysis is carried out. Suppose the files being analyzed are of significant quality. In that case, the memory of the computer must be at least 32GB to ensure cashed files don't exceed the physical memory of the computer. The MUSCLEMOTION software required a more experimental approach as many analysis parameters can be adjusted and an understanding of videography dynamics in combination with a good knowledge of cardiomyocyte contraction profiles is needed. The output files from the MUSCLEMOTION software are similar to the Pulse Video Analysis software but do allow for extra percentages of transients which are commonly used in cardiomyocyte contraction profile analysis.

Acknowledgements

J.I. acknowledges scholarship support from the Graduate Research School at the University of New South Wales (UNSW) with the University International Postgraduate Award (UIPA). This work was supported through funding from the Australian Research Council Grant FT180100417 (K.A.K.), the National Health and Medical Research Council Grant APP1185021 (K.A.K.), and the National Cancer Institute of the National Institutes of Health Grant R01CA251443 (K.A.K.). The authors acknowledge the help and support of Dr Alex Macmillan and Dr Michael

Carnell at the Katharina Gaus Light Imaging Facility (KGLMF) of the UNSW Mark Wainwright Analytical Centre. In addition, the authors acknowledge the help and support of the staff at CuriBio with the Pulse™ High-throughput video contractility analysis software.

Reference

1. Taylor DA, Silvestry SC, Bishop SP, Annex BH, Lilly RE, Glower DD, et al. Delivery of primary autologous skeletal myoblasts into rabbit heart by coronary infusion: a potential approach to myocardial repair. Proc Assoc Am Physicians. 1997 May;109(3):245–53.

2. Murry CE, Soonpaa MH, Reinecke H, Nakajima H, Nakajima HO, Rubart M, et al. Haematopoietic stem cells do not transdifferentiate into cardiac myocytes in myocardial infarcts. Nature. 2004 Apr 8;428(6983):664–8.

3. Chong JJH, Murry CE. Cardiac regeneration using pluripotent stem cells—Progression to large animal models. Stem Cell Research. 2014 Nov;13(3):654–65.

4. Murry CE, Keller G. Differentiation of Embryonic Stem Cells to Clinically Relevant Populations: Lessons from Embryonic Development. Cell. 2008 Feb;132(4):661–80.

5. Kane C, Terracciano CMN. Concise Review: Criteria for Chamber-Specific Categorization of Human Cardiac Myocytes Derived from Pluripotent Stem Cells. Stem Cells. 2017 Aug 1;35(8):1881–97.

6. Zimmermann W, Didie M, Doker S, Melnychenko I, Naito H, Rogge C, et al. Heart muscle engineering: An update on cardiac muscle replacement therapy. Cardiovascular Research. 2006 Aug 1;71(3):419–29.

7. Rozario T, DeSimone DW. The extracellular matrix in development and morphogenesis: a dynamic view. Dev Biol. 2010 May 1;341(1):126–40.

8. Joddar B, Natividad-Diaz SL, Padilla AE, Esparza AA, Ramirez SP, Chambers DR, et al. Engineering approaches for cardiac organoid formation and their characterization. Transl Res. 2022 Dec;250:46–67.

9. Sahara M. Recent Advances in Generation of In Vitro Cardiac Organoids. Int J Mol Sci. 2023 Mar 26;24(7):6244.

10. Lyra-Leite DM, Gutiérrez-Gutiérrez Ó, Wang M, Zhou Y, Cyganek L, Burridge PW. A review of protocols for human iPSC culture, cardiac differentiation, subtype-specification, maturation, and direct reprogramming. STAR Protoc. 2022 Sep 16;3(3):101560.

11. Mummery CL, Zhang J, Ng ES, Elliott DA, Elefanty AG, Kamp TJ. Differentiation of human embryonic stem cells and induced pluripotent stem cells to cardiomyocytes: a methods overview. Circ Res. 2012 Jul 20;111(3):344–58.

12. Sung TC, Liu CH, Huang WL, Lee YC, Kumar SS, Chang Y, et al. Efficient differentiation of human ES and iPS cells into cardiomyocytes on biomaterials under xeno-free conditions. Biomater Sci. 2019;7(12):5467–81.

13. Turner D, Rieger AC, Balkan W, Hare JM. Clinical-based Cell Therapies for Heart Disease—Current and Future State. Rambam Maimonides Med J. 2020 Apr 29;11(2):e0015.

14. Zhu R, Millrod MA, Zambidis ET, Tung L. Variability of Action Potentials Within and Among Cardiac Cell Clusters Derived from Human Embryonic Stem Cells. Sci Rep. 2016 Jan 5;6(1):18544.

15. Food and Drug Administration, HHS. International Conference on Harmonisation; guidance on S7B Nonclinical Evaluation of the Potential for Delayed Ventricular Repolarization (QT Interval Prolongation) by Human Pharmaceuticals; availability. Notice. Fed Regist. 2005 Oct 20;70(202):61133–4.

16. Wu H jin, Zou A ruo, Xie F, Du Y mei, Cao Y, Liu Y na, et al. Effect of matrine on human ether à go-go related gene (HERG) channels expressed in Chinese hamster ovary cells. Chin J Integr Med. 2010 Oct;16(5):430–4.

17. Walker BD, Valenzuela SM, Singleton CB, Tie H, Bursill JA, Wyse KR, et al. Inhibition of HERG channels stably expressed in a mammalian cell line by the antianginal agent perhexiline maleate. Br J Pharmacol. 1999 May;127(1):243–51.

18. Withdrawal of Troglitazone and Cisapride. JAMA. 2000 May 3;283(17):2228.

19. Josefson D. Hay fever drug to be banned by the FDA. BMJ. 1997 Jan 25;314(7076):247–247.

20. Crumb WJ, Vicente J, Johannesen L, Strauss DG. An evaluation of 30 clinical drugs against the comprehensive in vitro proarrhythmia assay (CiPA) proposed ion channel panel. J Pharmacol Toxicol Methods. 2016;81:251–62.

21. Passini E, Britton OJ, Lu HR, Rohrbacher J, Hermans AN, Gallacher DJ, et al. Human In Silico Drug Trials Demonstrate Higher Accuracy than Animal Models in Predicting Clinical Pro-Arrhythmic Cardiotoxicity. Front Physiol. 2017;8:668.

22. Robertson C, Tran DD, George SC. Concise review: maturation phases of human pluripotent stem cell-derived cardiomyocytes. Stem Cells. 2013 May;31(5):829–37.

23. Lian X, Hsiao C, Wilson G, Zhu K, Hazeltine LB, Azarin SM, et al. Robust cardiomyocyte differentiation from human pluripotent stem cells via temporal modulation of canonical Wnt signaling. Proc Natl Acad Sci U S A. 2012 Jul 3;109(27):E1848-1857.

24. Zhang J, Klos M, Wilson GF, Herman AM, Lian X, Raval KK, et al. Extracellular Matrix Promotes Highly Efficient Cardiac Differentiation of Human Pluripotent Stem Cells: The Matrix Sandwich Method. Circ Res. 2012 Oct 12;111(9):1125–36.

25. Burridge PW, Matsa E, Shukla P, Lin ZC, Churko JM, Ebert AD, et al. Chemically defined generation of human cardiomyocytes. Nat Methods. 2014 Aug;11(8):855–60.

26. Haase A, Olmer R, Schwanke K, Wunderlich S, Merkert S, Hess C, et al. Generation of induced pluripotent stem cells from human cord blood. Cell Stem Cell. 2009 Oct 2;5(4):434–41.

27. Moretti A, Bellin M, Welling A, Jung CB, Lam JT, Bott-Flügel L, et al. Patient-Specific Induced Pluripotent Stem-Cell Models for Long-QT Syndrome. N Engl J Med. 2010 Oct 7;363(15):1397–409.

28. Itzhaki I, Maizels L, Huber I, Zwi-Dantsis L, Caspi O, Winterstern A, et al. Modelling the long QT syndrome with induced pluripotent stem cells. Nature. 2011 Mar 10;471(7337):225–9.

29. Ma J, Guo L, Fiene SJ, Anson BD, Thomson JA, Kamp TJ, et al. High purity human-induced pluripotent stem cell-derived cardiomyocytes: electrophysiological properties of action potentials and ionic currents. Am J Physiol Heart Circ Physiol. 2011 Nov;301(5):H2006-2017.

30. Devalla HD, Schwach V, Ford JW, Milnes JT, El-Haou S, Jackson C, et al. Atrial-like cardiomyocytes from human pluripotent stem cells are a robust preclinical model for assessing atrial-selective pharmacology. EMBO Mol Med. 2015 Apr;7(4):394–410.

31. Weng Z, Kong CW, Ren L, Karakikes I, Geng L, He J, et al. A simple, cost-effective but highly efficient system for deriving ventricular cardiomyocytes from human pluripotent stem cells. Stem Cells Dev. 2014 Jul 15;23(14):1704–16.

32. Bowers SLK, Banerjee I, Baudino TA. The extracellular matrix: at the center of it all. J Mol Cell Cardiol. 2010 Mar;48(3):474–82.

33. Williams C, Black LD. The Role of Extracellular Matrix in Cardiac Development. In: Suuronen EJ, Ruel M, editors. Biomaterials for Cardiac Regeneration [Internet]. Cham: Springer International Publishing; 2015 [cited 2024 Jan 31]. p. 1–35. Available from: https://link.springer.com/10.1007/978-3-319-10972-5_1

34. Jacot JG, Martin JC, Hunt DL. Mechanobiology of cardiomyocyte development. Journal of Biomechanics. 2010 Jan;43(1):93–8.

35. Mollova M, Bersell K, Walsh S, Savla J, Das LT, Park SY, et al. Cardiomyocyte proliferation contributes to heart growth in young humans. Proc Natl Acad Sci U S A. 2013 Jan 22;110(4):1446–51.

36. Hedin U, Bottger BA, Forsberg E, Johansson S, Thyberg J. Diverse effects of fibronectin and laminin on phenotypic properties of cultured arterial smooth muscle cells. J Cell Biol. 1988 Jul;107(1):307–19.

37. Hynes RO. Fibronectins [Internet]. New York, NY: Springer New York; 1990 [cited 2024 Jan 31]. (Rich A, editor. Springer Series in Molecular Biology). Available from: http://link.springer.com/10.1007/978-1-4612-3264-3

38. Farhadian F, Contard F, Corbier A, Barrieux A, Rappaport L, Samuel JL. Fibronectin expression during physiological and pathological cardiac growth. Journal of Molecular and Cellular Cardiology. 1995 Apr;27(4):981–90.

39. Hornberger LK, Singhroy S, Cavalle-Garrido T, Tsang W, Keeley F, Rabinovitch M. Synthesis of Extracellular Matrix and Adhesion Through β_1 Integrins Are Critical for Fetal Ventricular Myocyte Proliferation. Circulation Research. 2000 Sep 15;87(6):508–15.

40. Feinstein JA, Benson DW, Dubin AM, Cohen MS, Maxey DM, Mahle WT, et al. Hypoplastic Left Heart Syndrome. Journal of the American College of Cardiology. 2012 Jan;59(1):S1–42.

41. Li F, Wang X, Capasso JM, Gerdes AM. Rapid transition of cardiac myocytes from hyperplasia to hypertrophy during postnatal development. J Mol Cell Cardiol. 1996 Aug;28(8):1737–46.

42. Samsa LA, Yang B, Liu J. Embryonic cardiac chamber maturation: Trabeculation, conduction, and cardiomyocyte proliferation. American J of Med Genetics Pt C. 2013 Aug;163(3):157–68.

43. Frangogiannis NG. The extracellular matrix in myocardial injury, repair, and remodeling. J Clin Invest. 2017 May 1;127(5):1600–12.

44. Cannon RO, Butany JW, McManus BM, Speir E, Kravitz AB, Bolli R, et al. Early degradation of collagen after acute myocardial infarction in the rat. The American Journal of Cardiology. 1983 Aug;52(3):390–5.

45. Shamhart PE, Meszaros JG. Non-fibrillar collagens: key mediators of post-infarction cardiac remodeling? J Mol Cell Cardiol. 2010 Mar;48(3):530–7.

46. Fomovsky GM, Holmes JW. Evolution of scar structure, mechanics, and ventricular function after myocardial infarction in the rat. Am J Physiol Heart Circ Physiol. 2010 Jan;298(1):H221-228.

47. Gaggi G, Di Credico A, Izzicupo P, Sancilio S, Di Mauro M, Iannetti G, et al. Decellularized Extracellular Matrices and Cardiac Differentiation: Study on Human Amniotic Fluid-Stem Cells. IJMS. 2020 Aug 31;21(17):6317.

48. Iop L, Palmosi T, Dal Sasso E, Gerosa G. Bioengineered tissue solutions for repair, correction and reconstruction in cardiovascular surgery. J Thorac Dis. 2018 Jul;10(Suppl 20):S2390–411.

49. Parveen S, Singh SP, Panicker MM, Gupta PK. Amniotic membrane as novel scaffold for human iPSC-derived cardiomyogenesis. In Vitro Cell Dev Biol Anim. 2019 Apr;55(4):272–84.

50. Liguori GR, Liguori TTA, de Moraes SR, Sinkunas V, Terlizzi V, van Dongen JA, et al. Molecular and Biomechanical Clues From Cardiac Tissue Decellularized Extracellular Matrix Drive Stromal Cell Plasticity. Front Bioeng Biotechnol. 2020;8:520.

51. Brafman DA, Phung C, Kumar N, Willert K. Regulation of endodermal differentiation of human embryonic stem cells through integrin-ECMP interactions. Cell Death Differ. 2013 Mar;20(3):369–81.

52. Xu RH, Peck RM, Li DS, Feng X, Ludwig T, Thomson JA. Basic FGF and suppression of BMP signaling sustain undifferentiated proliferation of human ES cells. Nat Methods. 2005 Mar;2(3):185–90.

53. Hughes CS, Postovit LM, Lajoie GA. Matrigel: A complex protein mixture required for optimal growth of cell culture. Proteomics. 2010 May;10(9):1886–90.

54. Tompkins JD, Hall C, Chen VC yi, Li AX, Wu X, Hsu D, et al. Epigenetic stability, adaptability, and reversibility in human embryonic stem cells. Proc Natl Acad Sci USA. 2012 Jul 31;109(31):12544–9.

55. Noaksson K, Zoric N, Zeng X, Rao MS, Hyllner J, Semb H, et al. Monitoring differentiation of human embryonic stem cells using real-time PCR. Stem Cells. 2005;23(10):1460–7.

56. Genbacev O, Krtolica A, Zdravkovic T, Brunette E, Powell S, Nath A, et al. Serum-free derivation of human embryonic stem cell lines on human placental fibroblast feeders. Fertil Steril. 2005 May;83(5):1517–29.

57. Braam SR, Zeinstra L, Litjens S, Ward-van Oostwaard D, van den Brink S, van Laake L, et al. Recombinant vitronectin is a functionally defined substrate that supports human embryonic stem cell self-renewal via alphavbeta5 integrin. Stem Cells. 2008 Sep;26(9):2257–65.

58. Beattie GM, Lopez AD, Bucay N, Hinton A, Firpo MT, King CC, et al. Activin A maintains pluripotency of human embryonic stem cells in the absence of feeder layers. Stem Cells. 2005 Apr;23(4):489–95.

59. Brafman DA, Shah KD, Fellner T, Chien S, Willert K. Defining long-term maintenance conditions of human embryonic stem cells with arrayed cellular microenvironment technology. Stem Cells Dev. 2009 Oct;18(8):1141–54.

60. Flaim CJ, Teng D, Chien S, Bhatia SN. Combinatorial Signaling Microenvironments for Studying Stem Cell Fate. Stem Cells and Development. 2008 Feb;17(1):29–40.

61. Flaim CJ, Chien S, Bhatia SN. An extracellular matrix microarray for probing cellular differentiation. Nat Methods. 2005 Feb;2(2):119–25.

62. Sa S, Wong L, McCloskey KE. Combinatorial Fibronectin and Laminin Signaling Promote Highly Efficient Cardiac Differentiation of Human Embryonic Stem Cells. BioResearch Open Access. 2014 Aug;3(4):150–61.

63. Samura T, Miyagawa S, Kawamura T, Fukushima S, Yokoyama J, Takeda M, et al. Laminin-221 Enhances Therapeutic Effects of Human-Induced Pluripotent Stem Cell–Derived 3-Dimensional Engineered Cardiac Tissue Transplantation in a Rat Ischemic Cardiomyopathy Model. JAHA. 2020 Aug 18;9(16):e015841.

64. Herron TJ, Rocha AMD, Campbell KF, Ponce-Balbuena D, Willis BC, Guerrero-Serna G, et al. Extracellular Matrix–Mediated Maturation of Human Pluripotent Stem Cell–Derived Cardiac Monolayer Structure and Electrophysiological Function. Circ: Arrhythmia and Electrophysiology. 2016 Apr;9(4):e003638.

65. Cabral-Pacheco GA, Garza-Veloz I, Castruita-De La Rosa C, Ramirez-Acuña JM, Perez-Romero BA, Guerrero-Rodriguez JF, et al. The Roles of Matrix Metalloproteinases and Their Inhibitors in Human Diseases. IJMS. 2020 Dec 20;21(24):9739.

66. Chong JJH, Yang X, Don CW, Minami E, Liu YW, Weyers JJ, et al. Human embryonic-stem-cell-derived cardiomyocytes regenerate non-human primate hearts. Nature. 2014 Jun;510(7504):273–7.

67. Hazeltine LB, Badur MG, Lian X, Das A, Han W, Palecek SP. Temporal impact of substrate mechanics on differentiation of human embryonic stem cells to cardiomyocytes. Acta Biomaterialia. 2014 Feb;10(2):604–12.

68. Tallawi M, Rai R, Boccaccini AldoR, Aifantis KE. Effect of Substrate Mechanics on Cardiomyocyte Maturation and Growth. Tissue Engineering Part B: Reviews. 2015 Feb;21(1):157–65.

69. Cao H, Zhou Q, Liu C, Zhang Y, Xie M, Qiao W, et al. Substrate stiffness regulates differentiation of induced pluripotent stem cells into heart valve endothelial cells. Acta Biomaterialia. 2022 Apr;143:115–26.

70. Ma Z, Wang J, Loskill P, Huebsch N, Koo S, Svedlund FL, et al. Self-organizing human cardiac microchambers mediated by geometric confinement. Nat Commun. 2015 Jul 14;6(1):7413.

71. Bao M, Xie J, Huck WTS. Recent Advances in Engineering the Stem Cell Microniche in 3D. Advanced Science. 2018 Aug;5(8):1800448.

72. Werley CA, Chien MP, Gaublomme J, Shekhar K, Butty V, Yi BA, et al. Geometry-dependent functional changes in iPSC-derived cardiomyocytes probed by functional imaging and RNA sequencing. Pesce M, editor. PLoS ONE. 2017 Mar 23;12(3):e0172671.

73. Myers FB, Silver JS, Zhuge Y, Beygui RE, Zarins CK, Lee LP, et al. Robust pluripotent stem cell expansion and cardiomyocyte differentiation *via* geometric patterning. Integrative Biology. 2013 Dec 18;5(12):1495–506.

74. Le MNT, Takahi M, Ohnuma K. Auto/paracrine factors and early Wnt inhibition promote cardiomyocyte differentiation from human induced pluripotent stem cells at initial low cell density. Sci Rep. 2021 Nov 2;11(1):21426.

75. Przybyla L, Voldman J. Probing Embryonic Stem Cell Autocrine and Paracrine Signaling Using Microfluidics. Annual Rev Anal Chem. 2012 Jul 19;5(1):293–315.

76. Kattman SJ, Huber TL, Keller GM. Multipotent Flk-1+ Cardiovascular Progenitor Cells Give Rise to the Cardiomyocyte, Endothelial, and Vascular Smooth Muscle Lineages. Developmental Cell. 2006 Nov;11(5):723–32.

77. Bondue A, Lapouge G, Paulissen C, Semeraro C, Iacovino M, Kyba M, et al. Mesp1 Acts as a Master Regulator of Multipotent Cardiovascular Progenitor Specification. Cell Stem Cell. 2008 Jul;3(1):69–84.

78. Wheelwright M, Mikkila J, Bedada FB, Mandegar MA, Thompson BR, Metzger JM. Advancing physiological maturation in human induced pluripotent stem cell-derived cardiac muscle by gene editing an inducible adult troponin isoform switch. Stem Cells. 2020 Oct 1;38(10):1254–66.

79. Karbassi E, Fenix A, Marchiano S, Muraoka N, Nakamura K, Yang X, et al. Cardiomyocyte maturation: advances in knowledge and implications for regenerative medicine. Nat Rev Cardiol. 2020 Jun;17(6):341–59.

80. Piccini I, Rao J, Seebohm G, Greber B. Human pluripotent stem cell-derived cardiomyocytes: Genome-wide expression profiling of long-term in vitro maturation in comparison to human heart tissue. Genomics Data. 2015 Jun;4:69–72.

81. Kubalak SW, Miller-Hance WC, O'Brien TX, Dyson E, Chien KR. Chamber specification of atrial myosin light chain-2 expression precedes septation during murine cardiogenesis. Journal of Biological Chemistry. 1994 Jun;269(24):16961–70.

82. O'Brien TX, Lee KJ, Chien KR. Positional specification of ventricular myosin light chain 2 expression in the primitive murine heart tube. Proc Natl Acad Sci USA. 1993 Jun;90(11):5157–61.

83. Wu P, Deng G, Sai X, Guo H, Huang H, Zhu P. Maturation strategies and limitations of induced pluripotent stem cell-derived cardiomyocytes. Bioscience Reports. 2021 Jun 25;41(6):BSR20200833.

84. Maddah M, Heidmann JD, Mandegar MA, Walker CD, Bolouki S, Conklin BR, et al. A Non-invasive Platform for Functional Characterization of Stem-Cell-Derived

Cardiomyocytes with Applications in Cardiotoxicity Testing. Stem Cell Reports. 2015 Apr;4(4):621–31.

85. Kane C, Terracciano CMN. Concise Review: Criteria for Chamber-Specific Categorization of Human Cardiac Myocytes Derived from Pluripotent Stem Cells. Stem Cells. 2017 Aug 1;35(8):1881–97.

86. Sánchez C, Bueno-Orovio A, Wettwer E, Loose S, Simon J, Ravens U, et al. Inter-Subject Variability in Human Atrial Action Potential in Sinus Rhythm versus Chronic Atrial Fibrillation. Panfilov AV, editor. PLoS ONE. 2014 Aug 26;9(8):e105897.

87. Barth AS, Merk S, Arnoldi E, Zwermann L, Kloos P, Gebauer M, et al. Functional profiling of human atrial and ventricular gene expression. Pflugers Arch - Eur J Physiol. 2005 Jul;450(4):201–8.

88. Verkerk AO, Wilders R, Van Borren MMGJ, Peters RJG, Broekhuis E, Lam K, et al. Pacemaker current (If) in the human sinoatrial node. European Heart Journal. 2007 Sep 7;28(20):2472–8.

89. Irisawa H, Brown HF, Giles W. Cardiac pacemaking in the sinoatrial node. Physiological Reviews. 1993 Jan 1;73(1):197–227.

90. Boyett MR, Honjo H, Yamamoto M, Nikmaram MR, Niwa R, Kodama I. Downward gradient in action potential duration along conduction path in and around the sinoatrial node. American Journal of Physiology-Heart and Circulatory Physiology. 1999 Feb 1;276(2):H686–98.

91. Nagy N, Szél T, Jost N, Tóth A, Gy. Papp J, Varró A. Novel experimental results in human cardiac electrophysiology: measurement of the Purkinje fibre action potential from the undiseased human heart. Can J Physiol Pharmacol. 2015 Sep;93(9):803–10.

92. Patel C, Burke JF, Patel H, Gupta P, Kowey PR, Antzelevitch C, et al. Is there a significant transmural gradient in repolarization time in the intact heart?: Cellular Basis of the T Wave: A Century of Controversy. Circ: Arrhythmia and Electrophysiology. 2009 Feb;2(1):80–8.

93. Dawodu AA, Monti F, Iwashiro K, Schiariti M, Chiavarelli R, Puddu PE. The shape of human atrial action potential accounts for different frequency-related changes in vitro. International Journal of Cardiology. 1996 Jun;54(3):237–49.

94. Le Grand B, Hatem S, Deroubaix E, Couetil JP, Coraboeuf E. Calcium current depression in isolated human atrial myocytes after cessation of chronic treatment with calcium antagonists. Circ Res. 1991 Aug;69(2):292–300.

95. Workman A. The contribution of ionic currents to changes in refractoriness of human atrial myocytes associated with chronic atrial fibrillation. Cardiovascular Research. 2001 Nov;52(2):226–35.

96. Bukowska A, Nikonova Y, Wolke C, Lendeckel U, Kockskämper J, Goette A. Anti-inflammatory effects of endothelin receptor blockade in left atrial tissue of spontaneously hypertensive rats. IJC Heart & Vasculature. 2022 Oct;42:101088.

97. Dobrev D, Graf E, Wettwer E, Himmel HM, Hála O, Doerfel C, et al. Molecular Basis of Downregulation of G-Protein–Coupled Inward Rectifying K^+ Current ($I_{K,ACh}$) in Chronic Human Atrial Fibrillation: Decrease in GIRK4 mRNA Correlates With Reduced $I_{K,ACh}$ and Muscarinic Receptor–Mediated Shortening of Action Potentials. Circulation. 2001 Nov 20;104(21):2551–7.

98. Van Wagoner DR, Pond AL, Lamorgese M, Rossie SS, McCarthy PM, Nerbonne JM. Atrial L-Type Ca^{2+} Currents and Human Atrial Fibrillation. Circulation Research. 1999 Sep 3;85(5):428–36.

99. Drouin E, Lande G, Charpentier F. Amiodarone reduces transmural heterogeneity of repolarization in the human heart. Journal of the American College of Cardiology. 1998 Oct;32(4):1063–7.

100. Li GR, Feng J, Yue L, Carrier M. Transmural heterogeneity of action potentials and I_{to1} in myocytes isolated from the human right ventricle. American Journal of Physiology-Heart and Circulatory Physiology. 1998 Aug 1;275(2):H369–77.

101. Rowland TJ, Miller LM, Blaschke AJ, Doss EL, Bonham AJ, Hikita ST, et al. Roles of Integrins in Human Induced Pluripotent Stem Cell Growth on Matrigel and Vitronectin. Stem Cells and Development. 2010 Aug;19(8):1231–40.

102. Sala L, Van Meer BJ, Tertoolen LGJ, Bakkers J, Bellin M, Davis RP, et al. MUSCLEMOTION: A Versatile Open Software Tool to Quantify Cardiomyocyte and Cardiac Muscle Contraction In Vitro and In Vivo. Circulation Research [Internet].

2018 Feb 2 [cited 2024 Feb 6];122(3). Available from: https://www.ahajournals.org/doi/10.1161/CIRCRESAHA.117.312067

103. James TN, Sherf L, Fine G, Morales AR. Comparative Ultrastructure of the Sinus Node in Man and Dog. Circulation. 1966 Jul;34(1):139–63.

104. Ono N, Yamaguchi T, Ishikawa H, Arakawa M, Takahashi N, Saikawa T, et al. Morphological varieties of the Purkinje fiber network in mammalian hearts, as revealed by light and electron microscopy. Arch Histol Cytol. 2009;72(3):139–49.

105. Nygren A, Fiset C, Firek L, Clark JW, Lindblad DS, Clark RB, et al. Mathematical Model of an Adult Human Atrial Cell: The Role of K^+ Currents in Repolarization. Circulation Research. 1998 Jan 23;82(1):63–81.

106. Mary-Rabine L, Albert A, Pham TD, Hordof A, Fenoglio JJ, Malm JR, et al. The relationship of human atrial cellular electrophysiology to clinical function and ultrastructure. Circ Res. 1983 Feb;52(2):188–99.

107. Tracy RE. Cardiac myocyte sizes in right compared with left ventricle during overweight and hypertension. Journal of the American Society of Hypertension. 2014 Jul;8(7):457–63.

108. Shimada T, Kawazato H, Yasuda A, Ono N, Sueda K. Cytoarchitecture and intercalated disks of the working myocardium and the conduction system in the mammalian heart. Anat Rec. 2004 Oct;280A(2):940–51.

109. Kamakura T, Makiyama T, Sasaki K, Yoshida Y, Wuriyanghai Y, Chen J, et al. Ultrastructural Maturation of Human-Induced Pluripotent Stem Cell-Derived Cardiomyocytes in a Long-Term Culture. Circ J. 2013;77(5):1307–14.

110. Lukyanenko V, Chikando A, Lederer WJ. Mitochondria in cardiomyocyte Ca2+ signaling. The International Journal of Biochemistry & Cell Biology. 2009 Oct;41(10):1957–71.

111. Jakob H, Oelert H, Rupp J, Nawrath H. Functional role of cholinoceptors and purinoceptors in human isolated atrial and ventricular heart muscle. British J Pharmacology. 1989 Aug;97(4):1199–208.

112. Redpath CJ, Rankin AC, Kane KA, Workman AJ. Anti-adrenergic effects of endothelin on human atrial action potentials are potentially anti-arrhythmic. Journal of Molecular and Cellular Cardiology. 2006 May;40(5):717–24.

113. Chuva De Sousa Lopes SM, Hassink RJ, Feijen A, Van Rooijen MA, Doevendans PA, Tertoolen L, et al. Patterning the heart, a template for human cardiomyocyte development. Developmental Dynamics. 2006 Jul;235(7):1994–2002.

114. Gaborit N, Le Bouter S, Szuts V, Varro A, Escande D, Nattel S, et al. Regional and tissue specific transcript signatures of ion channel genes in the non-diseased human heart. The Journal of Physiology. 2007 Jul 15;582(2):675–93.

115. Atere M, Galligan S. Unusual Troponin Level in Atrioventricular Nodal Reentrant Tachycardia Despite Normal Coronary Arteries. Am J Case Rep. 2020 May 8;21:e922831.

116. Christoffels VM, Moorman AFM. Development of the Cardiac Conduction System: Why Are Some Regions of the Heart More Arrhythmogenic Than Others? Circ: Arrhythmia and Electrophysiology. 2009 Apr;2(2):195–207.

117. England J, Pang KL, Parnall M, Haig MI, Loughna S. *Cardiac troponin T* is necessary for normal development in the embryonic chick heart. Journal of Anatomy. 2016 Sep;229(3):436–49.

118. Naito AT, Shiojima I, Akazawa H, Hidaka K, Morisaki T, Kikuchi A, et al. Developmental stage-specific biphasic roles of Wnt/β-catenin signaling in cardiomyogenesis and hematopoiesis. Proc Natl Acad Sci USA. 2006 Dec 26;103(52):19812–7.

119. Takahashi K, Yamanaka S. Induction of Pluripotent Stem Cells from Mouse Embryonic and Adult Fibroblast Cultures by Defined Factors. Cell. 2006 Aug;126(4):663–76.

120. Lo B, Parham L. Ethical Issues in Stem Cell Research. Endocrine Reviews. 2009 May 1;30(3):204–13.

121. Menasché P, Vanneaux V, Hagège A, Bel A, Cholley B, Parouchev A, et al. Transplantation of Human Embryonic Stem Cell–Derived Cardiovascular

Progenitors for Severe Ischemic Left Ventricular Dysfunction. Journal of the American College of Cardiology. 2018 Jan;71(4):429–38.

122. Glauche I, Herberg M, Roeder I. Nanog Variability and Pluripotency Regulation of Embryonic Stem Cells - Insights from a Mathematical Model Analysis. Di Bernardo D, editor. PLoS ONE. 2010 Jun 21;5(6):e11238.

123. Karbassi E, Murry CE. Flexing Their Muscles: Maturation of Stem Cell–Derived Cardiomyocytes on Elastomeric Substrates to Enhance Cardiac Repair. Circulation. 2022 May 3;145(18):1427–30.

Supporting Results

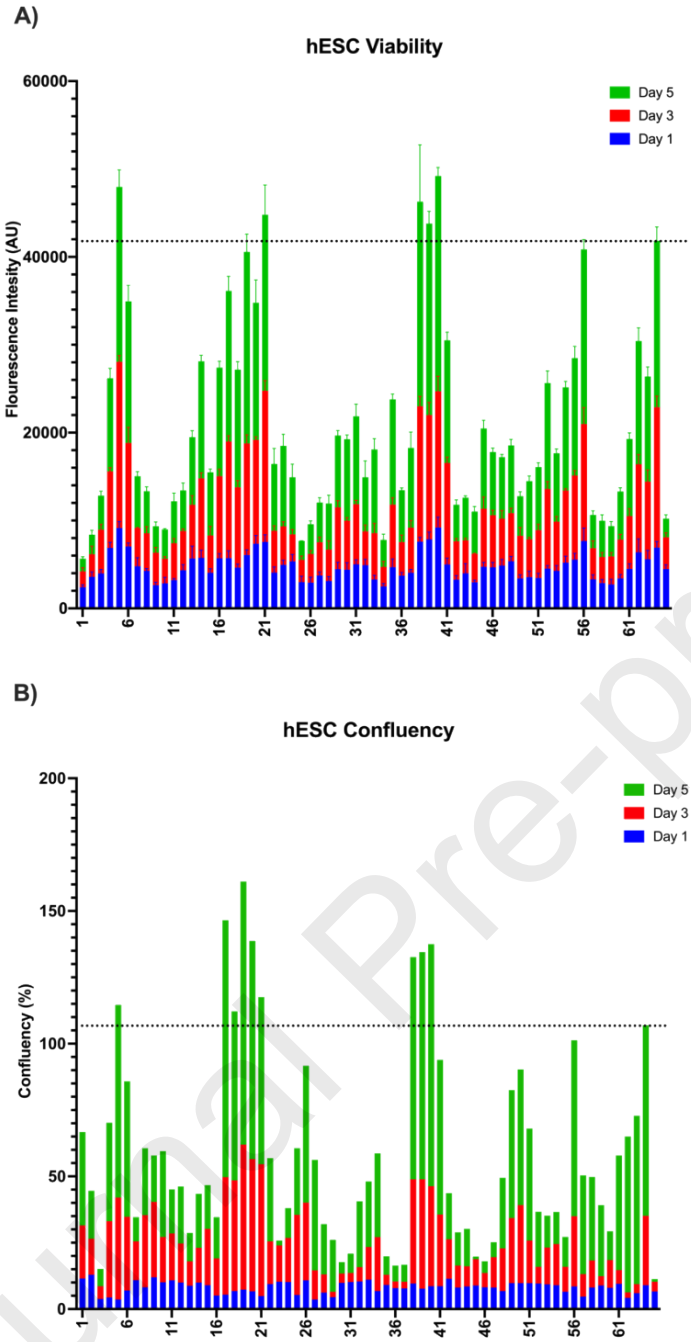

Protein combination	Well plate location	Graph number
C1	A1	1
C3	B1	2
C4	C1	3
F	D2	4
L	E1	5
V	F1	6
C1C3	G1	7
C1C4	H1	8
C1F	A2	9
C1L	B2	10
C1V	C2	11
C3C4	D2	12
C3F	E2	13
C3L	F2	14
C3V	G2	15
C4F	H2	16
C4L	A3	17
C4V	B3	18
FL	C3	19
FV	D3	20
LV	E3	21
C1C3C4	F3	22
C1C3F	G3	23
C1C3L	H3	24
C1C3V	A4	25
C1C4F	B4	26
C1C4L	C4	27
C1C4V	D4	28
C1FL	E4	29
C1FV	F4	30
C1LV	G4	31
C3C4F	H4	32
C3C4L	A5	33
C3C4V	B5	34
C3FL	C5	35
C3FV	D5	36
C3LV	E5	37
C4FL	F5	38
C4FV	G5	39
C4LV	H5	40
FLV	A6	41
C1C3C4F	B6	42
C1C3C4L	C6	43
C1C3C4V	D6	44
C1C3FL	E6	45
C1C3FV	F6	46
C1C3LV	G6	47
C1C4FL	H6	48
C1C4FV	A7	49
C1C4LV	B7	50
C1FLV	C7	51
C3C4FL	D7	52
C3C4FV	E7	53
C3C4LV	F7	54
C3FLV	G7	55
C4FLV	H7	56
C1C3C4FL	A8	57
C1C3C4FV	B8	58
C1C3C4LV	C8	59
C1C3FLV	D8	60
C1C4FLV	E8	61
C3C4FLV	F8	62
C1C3C4FLV	G8	63
Matrigel	A11-H11	64
Plastic	A12-H12	65

Figure S1. Viability and Confluency of hESC over 5 days. A) Graphical summation of viability as measured via alamarBlue™ HS stain over 5 days on 63 ECMP combinations. The viability of the cells on each day is added up to show how the ECMP combinations affect cell growth. Dotted line indicates viability of control group (Matrigel). B) Graphical summation of confluency as measured via the Olympus confluency checker software over 5 days on all 63 ECMP combinations. The confluency on each day is added up to highlight the effects of the ECMP on cell growth over time. The dotted line indicates the confluency of the control group (Matrigel).

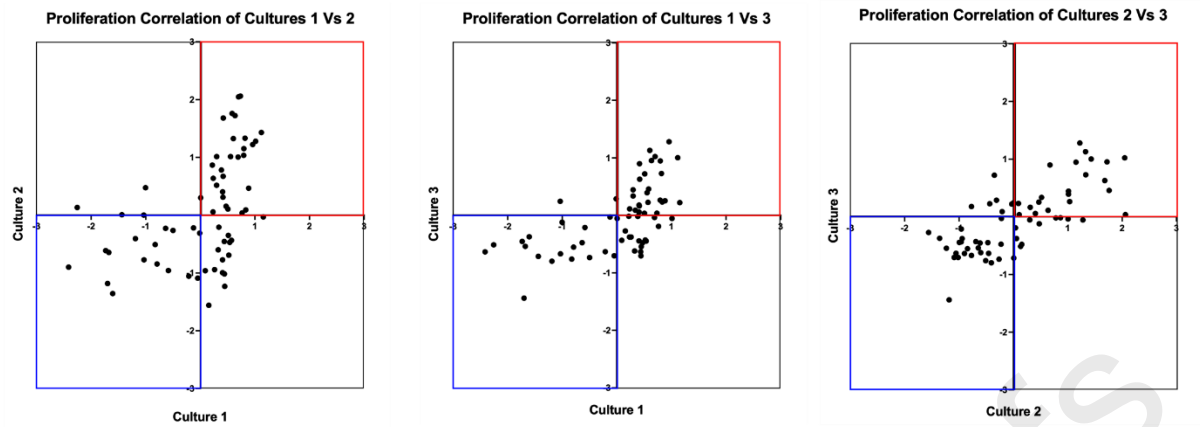

Figure S2: Pearson's correlation of extracellular matrix proteins (ECMPs) combinations effect on human embryonic stem cell (hESC) proliferation. A) Pearson correlation matrices of mean proliferation index values (μPRO) comparing ECMP combinations from independent. cultures. Each matrix is split into two segments that correspond to the higher (red) and lower (blue) proliferation groups compared to the global average mean = 0.

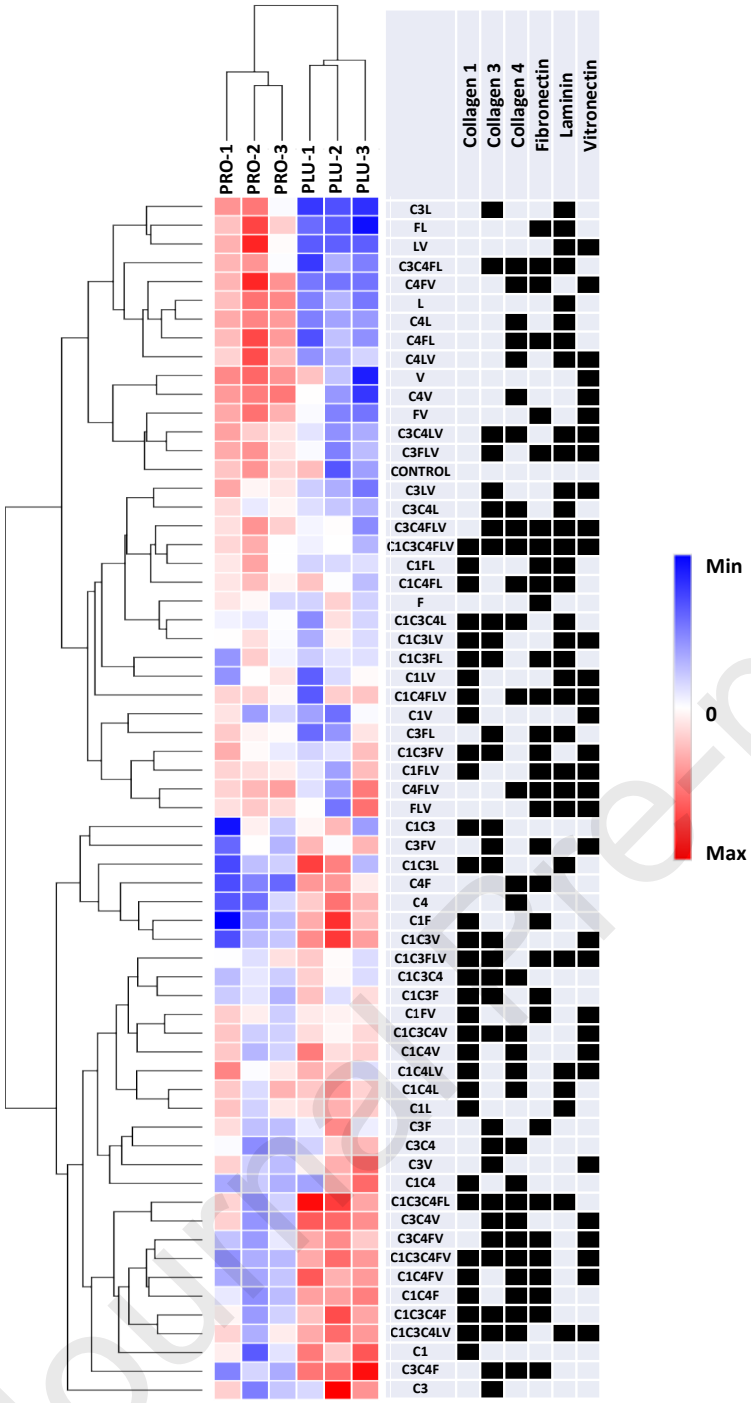

Figure S3. **Heatmap of extracellular matrix proteins (ECMPs) combinations effect on human embryonic stem cell (hESC) proliferation and corresponding pluripotency.** A) Heat map of the mean proliferation index values (μ_{PRO}) and mean pluripotency index values (μ_{PLU}) for each ECMP combination (row) for the six independent cultures (columns). Six independent array cultures were conducted for each ECMP combination and seeded with hESC H9 cells. The ECMP combination is indicated with the protein name anacronym and the shaded boxes in the table to the right of the heat map. A hierarchical clustering was performed with a Euclidian distancing metric and an average linkage method. Hierarchical clustering of the ECMPs revealed four segregated groups also displayer in the correlation graph in figure 3.7A (i) High Proliferation and high pluripotency (red), (ii) High proliferation and low pluripotency (green), (iii) Low proliferation

and high pluripotency (orange), (iv) Low proliferation and low pluripotency (blue). These high and low data points are referring to the averaged index values around the global average mean (0).

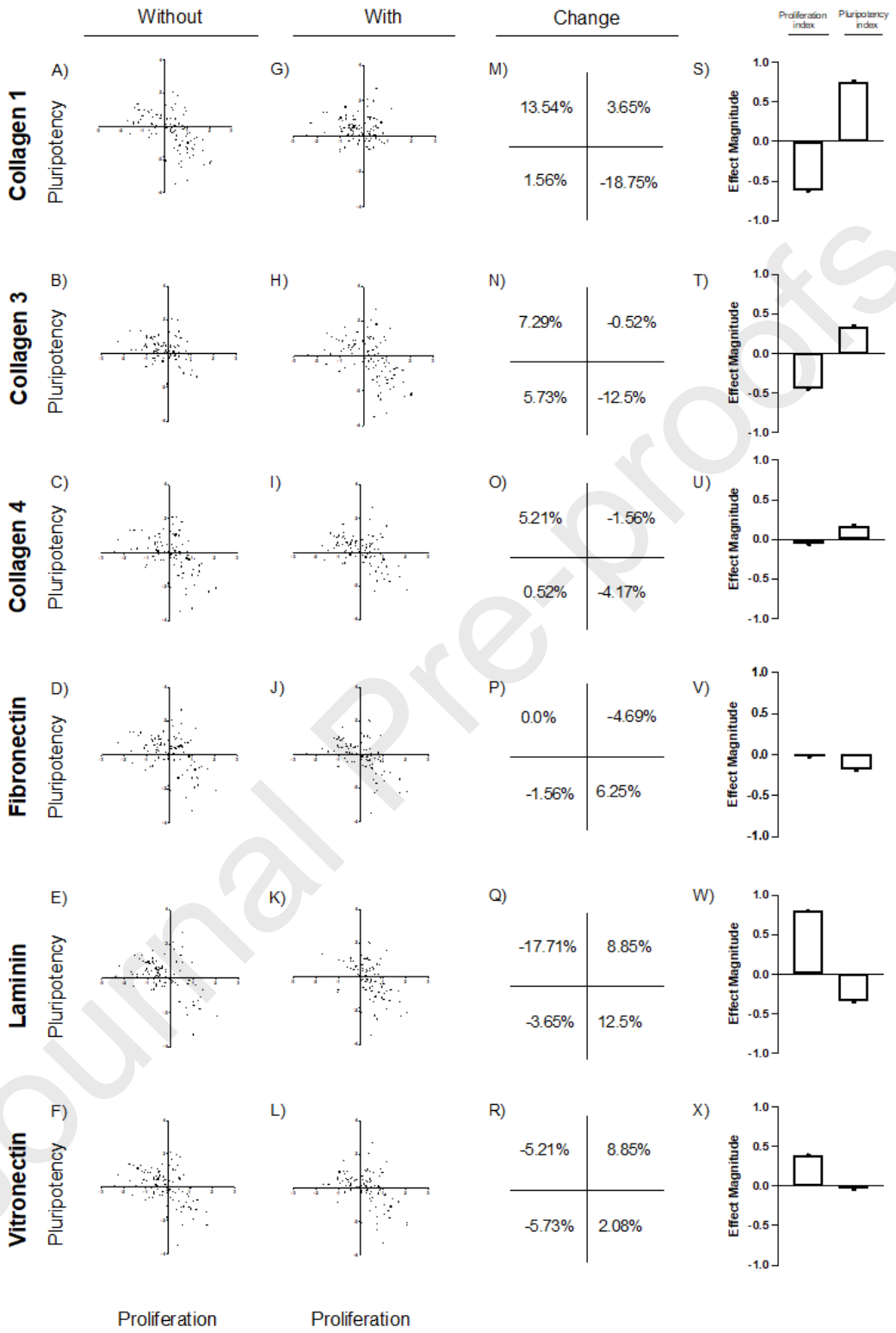

Figure S4. **Analysis of extracellular matrix proteins (ECMP) effect on proliferation and pluripotency of human embryonic stem cells (hESC).** Pluripotency Vs proliferation correlations is plotted for all the ECMP combinations (A, B, C, D, E, F) without and (G, H, I, J, K, L) with the Specific ECMP stated on the left of the plots. (M, N, O, P, Q, R) The percentage change in each of the four quadrants of the correlation graph when the specified ECMP is included. (S, T, U, V,

W, X) The effect magnitude of each of the specified ECMPs on the hESCs pluripotency and proliferation.

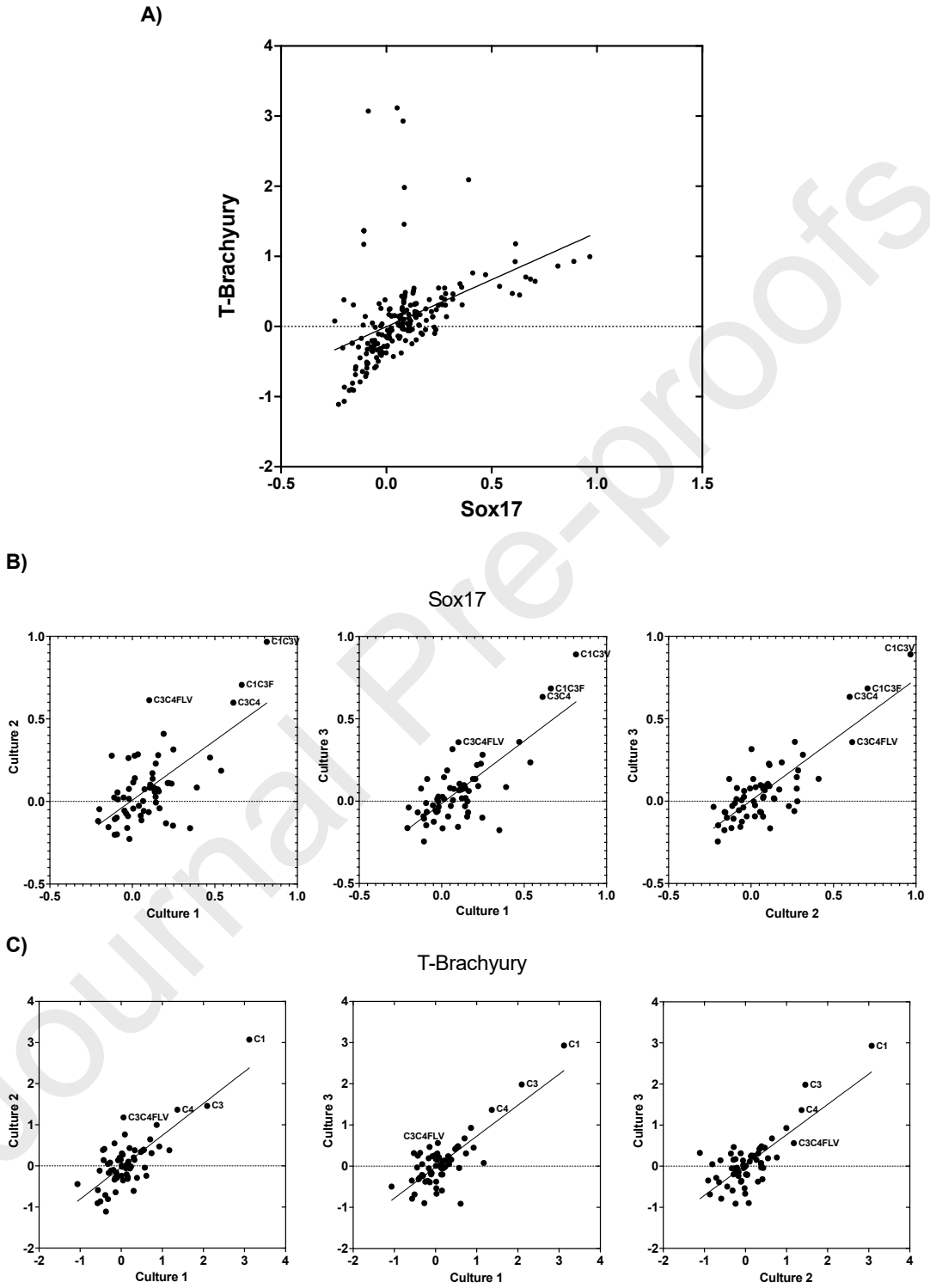

Figure S5. **Correlation of germ layer expression on extracellular matrix proteins (ECMPs) combinations.** A) Pearson correlation matrix of sox17 and T-Brachyury index values (r=0.4468 R^2= 0.1996). B) Person correlation comparing sox17 expression on ECMP combinations from independent cultures (left to right r=0.6489 R^2=0.4211, r=0.7558 R^2=0.5712, r=0.8187

R^2=0.6703). C) Person correlation comparing T-Brachyury expression on ECMP combinations from independent cultures (left to right r=0.7750 R^2=0.6007, r=0.7837 R^2=0.6142, r=0.7694 R^2=0.5921).

To evaluate cardiac progenitor expression on the protein microarray, we used the following equation:

$$CPROG = \frac{\chi - \mu_{CP}}{\sigma_{CP}}$$

Where χ is the Log_2 of the cardiac progenitor signal for the well, μ_{CP} is the average of the Log_2 cardiac progenitor signal for all the wells on the plate, and σ_{CP} is the standard deviation of the Log_2 cardiac progenitor signals for all the wells on the plate. The cardiac progenitor Index values from the replicated cultures (n=3 per ECMP condition) were averaged for each ECMP combination (μ_{CPROG}). The progenitor expression in the hESC cells to each ECMP combination is displayed in a heat map in Figure S6 alongside the proliferation, pluripotency, and germ layer marker index values. We can initially use this cluster diagram to identify the protein combinations that give high and low expression values for the pre-cardiac mesoderm and cardiac progenitor markers and how this may correlate to germ layer expression. Initial observations don't reveal distinct groups of KDR+/MESP1+ compared to germ layer or pluripotency markers, but we can see some possible correlation between cardiac progenitor expression and proliferation.

We expect that the MESP1 and KDR markers will be expressed during cardiac differentiation. To test this, we initially performed a Pearson correlation to determine the relationship of their co-expression. Figure S7 reveals a weak correlation between the cardiac progenitor markers (r=0.1511 R^2=0.02284 p=0.0364). To highlight that this is not an anomalous result, three independent cultures were fixed and stained for MESP1 and KDR. The correlations between those three independent cultures are shown in Figures S7 B and C, which all highlight good positive correlations of expression. Given that these graphs display index values for the expression of cardiac progenitors, they represent the expression compared to a global average mean. This means that the most likely candidates for cardiac differentiation would display enhanced index values, but this is not guaranteed.

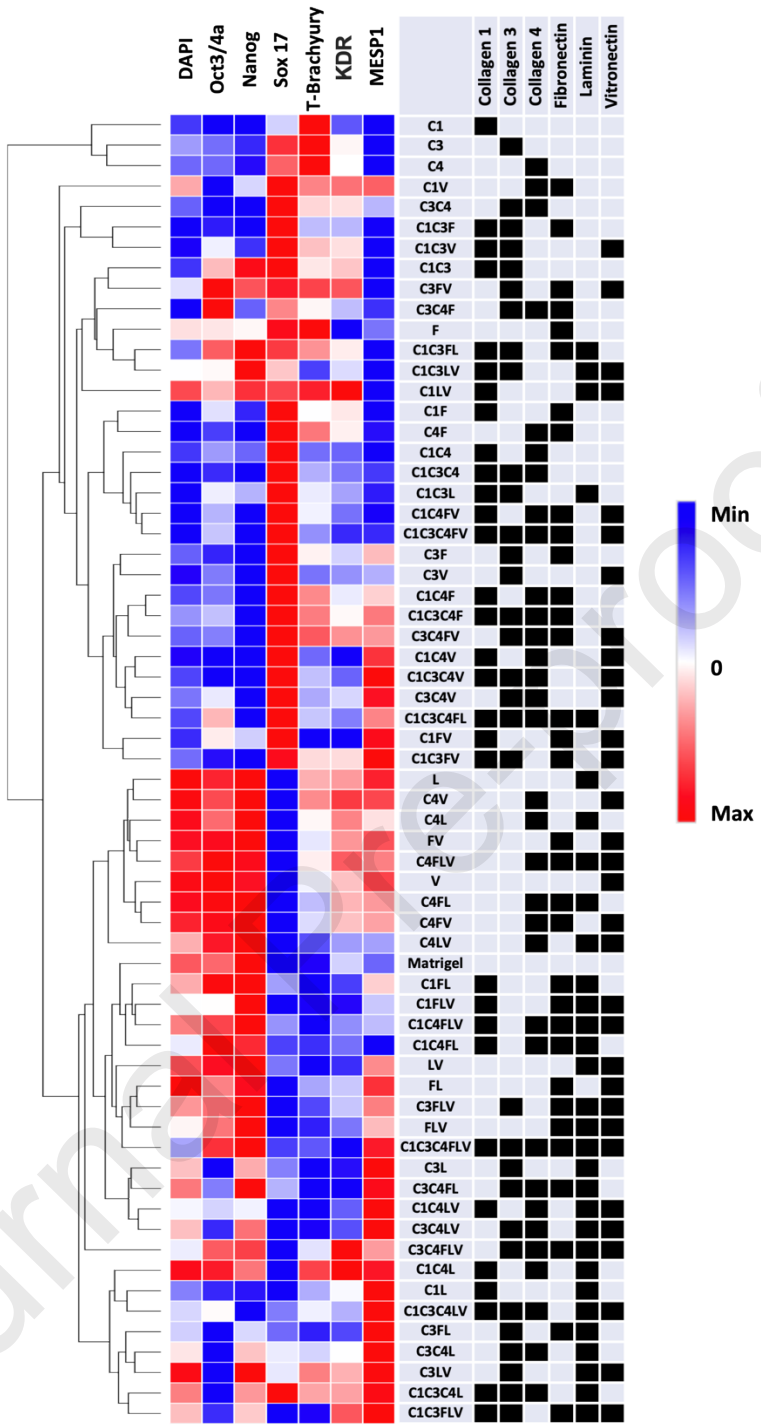

Figure S6. **Heat map of extracellular matrix proteins (ECMPs) combinations effect on human embryonic stem cell (hESC) proliferation, pluripotency, germ layer differentiation, and cardiac progenitor expression.** Heat map of the mean proliferation index values (μ_{PRO}), mean pluripotency index values (μ_{Plu}), mean germ layer index values (μ_{Germ}), and cardiac progenitor index values (μ_{CP}) for each ECMP combination (row). Three independent array cultures were conducted for each biomarker and had their index values averaged for each ECMP combination (column). The ECMP combination is indicated with the protein name acronym and the shaded boxes in the table to the right of the heat map. A hierarchical clustering was performed with a Euclidian distancing metric and an average linkage method. These high and low data points are referring to the averaged index values around the global average mean (0).

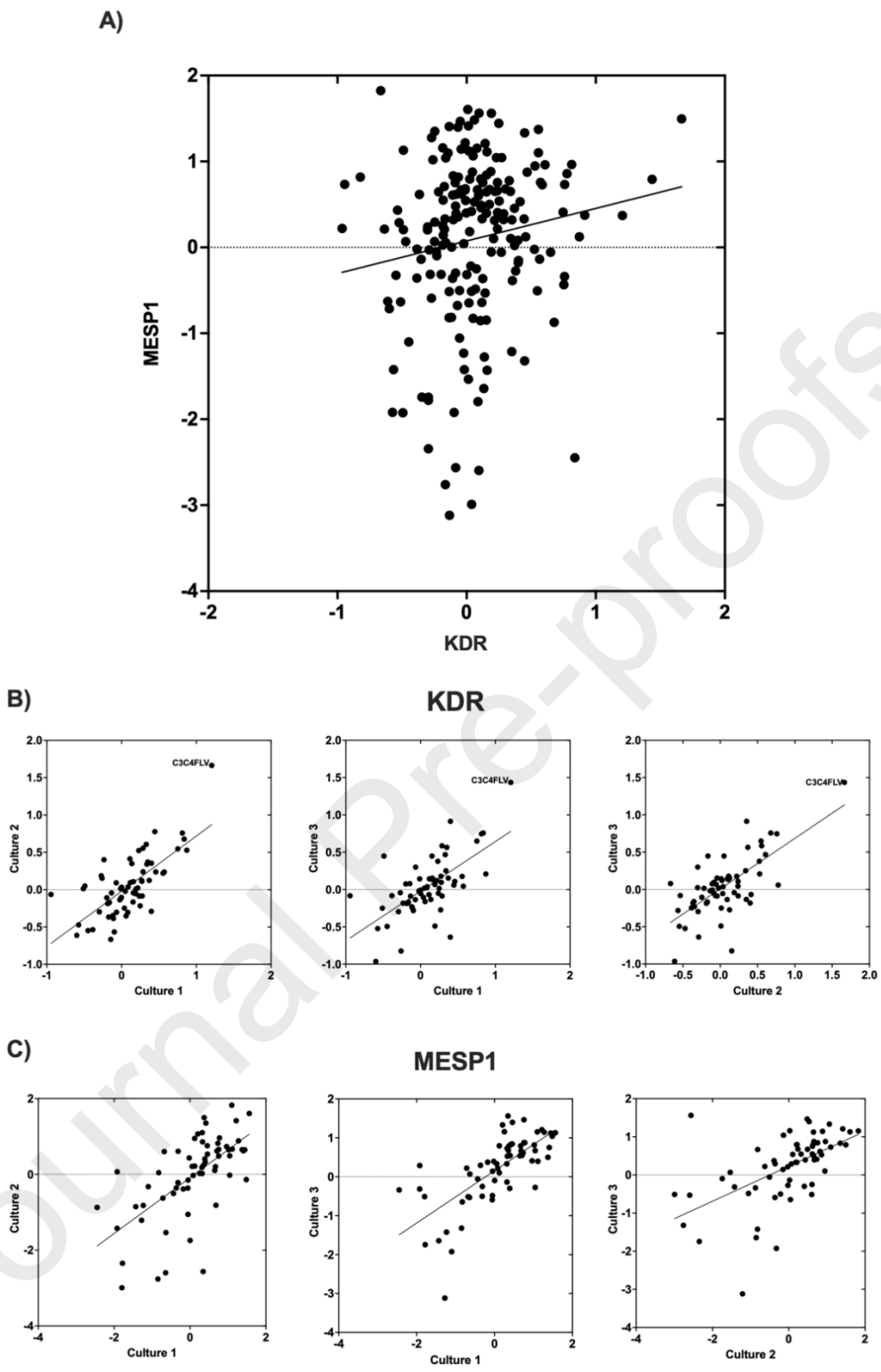

Figure S7. **Correlation of cardiac progenitor expression on extracellular matrix proteins (ECMPs) combinations.** A) Pearson correlation matrix of MESP1 and KDR index values (r=0.1511 R^2= 0.02284). B) Person correlation comparing KDR expression on ECMP combinations from independent cultures (left to right r=0.7046 R^2=0.4965, r=0.6482 R^2=0.4201, r=0.6928 R^2=0.4800). C) Person correlation comparing MESP1 expression on ECMP combinations from independent cultures (left to right r=0.6378 R^2=0.4068, r=0.7040 R^2=0.4957, r=0.5540 R^2=0.3069).

Figure S8A shows the index values for MESP1, pre and post differentiation, on all 63 ECMP combinations. As we have seen that certain ECMP combinations can influence germ layer differentiation, we can assume that the ECMP combinations that show positive index values in hESC are more likely to produce contracting cardiomyocytes. Figure S8B shows all 21 protein combinations with positive index values for KDR and MESP1. It is assumed that positive expression of cardiac progenitor markers should correlate with high expression of T-Brachyury to indicate cardiac differentiation originates from mesoderm lineage. From what was revealed in the previous section, Sox17 and T-Brachyury are often co-expressed as indicated by the positive correlation of their index markers.

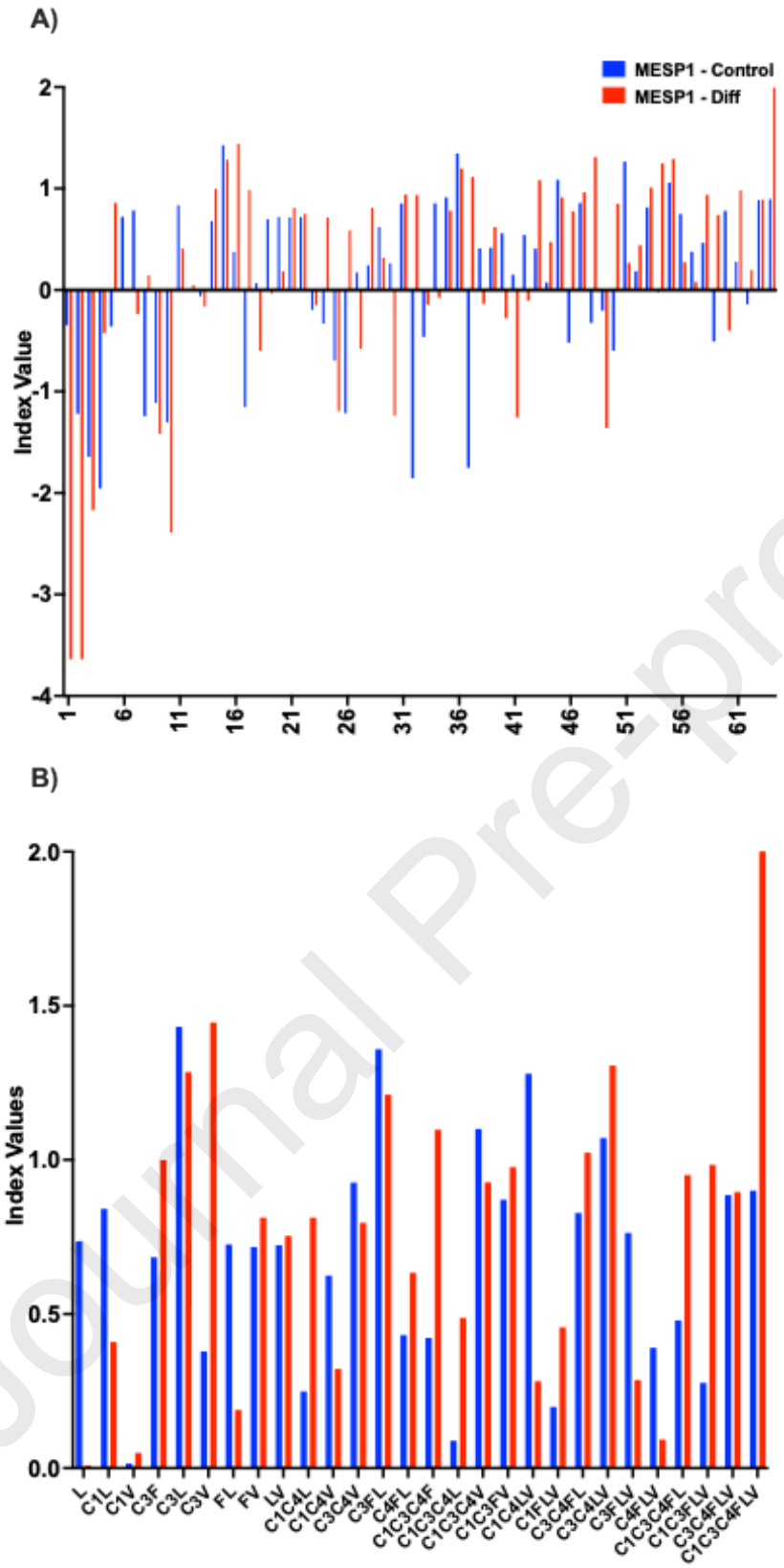

Protein combination	Well plate location	Graph number
C1	A1	1
C3	B1	2
C4	C1	3
F	D2	4
L	E1	5
V	F1	6
C1C3	G1	7
C1C4	H1	8
C1F	A2	9
C1L	B2	10
C1V	C2	11
C3C4	D2	12
C3F	E2	13
C3L	F2	14
C3V	G2	15
C4F	H2	16
C4L	A3	17
C4V	B3	18
FL	C3	19
FV	D3	20
LV	E3	21
C1C3C4	F3	22
C1C3F	G3	23
C1C3L	H3	24
C1C3V	A4	25
C1C4F	B4	26
C1C4L	C4	27
C1C4V	D4	28
C1FL	E4	29
C1FV	F4	30
C1LV	G4	31
C3C4F	H4	32
C3C4L	A5	33
C3C4V	B5	34
C3FL	C5	35
C3FV	D5	36
C3LV	E5	37
C4FL	F5	38
C4FV	G5	39
C4LV	H5	40
FLV	A6	41
C1C3C4F	B6	42
C1C3C4L	C6	43
C1C3C4V	D6	44
C1C3FL	E6	45
C1C3FV	F6	46
C1C3LV	G6	47
C1C4FL	H6	48
C1C4FV	A7	49
C1C4LV	B7	50
C1FLV	C7	51
C3C4FL	D7	52
C3C4FV	E7	53
C3C4LV	F7	54
C3FLV	G7	55
C4FLV	H7	56
C1C3C4FL	A8	57
C1C3C4FV	B8	58
C1C3C4LV	C8	59
C1C3FLV	D8	60
C1C4FLV	E8	61
C3C4FLV	F8	62
C1C3C4FLV	G8	63
Matrigel	A11-H11	64
Plastic	A12-H12	65

Figure S8. **Bar chart of cardiac progenitor expression index values in H9 hESC fixed on day 5 (120h) when seeded on ECMP array.** A) Index values for KDR (blue) and MESP1 (red) of hESC on all ECMP combinations. B) Index value of ECMP combinations that showed positive index values for both KDR and MESP1. These high and low data points refer to the averaged index values around the global average mean (0) for the individual ECMP combination.

In Figure S9, we can see KDR has a positive correlation with Sox17, but it does not have a significant correlation with T-Brachyury (Sox17 – r=0.7251 R^2=0.5257 p=<0.0001. T-Brachyury – r=0.1751 R^2=0.03066 p=0.1664). When isolating the data points corresponding to the 21 ECMP combinations that were double positive for KDR and MESP1 (blue dots), we see a similar correlation of KDR with Sox 17 and a greatly enhanced positive correlation with T-Brachyury (Sox17 – r=0.6069 R^2=0.3648 p=0.0045. T-Brachyury – r=0.6116 R^2=0.3740 p=0.0042). In Figure S9, we see the correlation of MESP1 with Sox17 and T-Brachyury is very weak and negative in both graphs (Sox17 - r=-0.08959 R^2=0.008026 p=0.4814. T-Brachyury - r=-0.4079 R^2=0.1664 p=0.0008). Again, when we look at the isolated data points corresponding to the 21 ECMP combinations that were double positive for KDR. and MESP1 (blue dots), we see a similar trend in Sox 17 but an enhanced positive yet relatively weak correlation between T-Brachyury and MESP1 (Sox17 - r=-0.1032 R^2=0.01065 p=0.6651. T-Brachyury - r=0.2682 R^2=0.07194 p=0.2529).

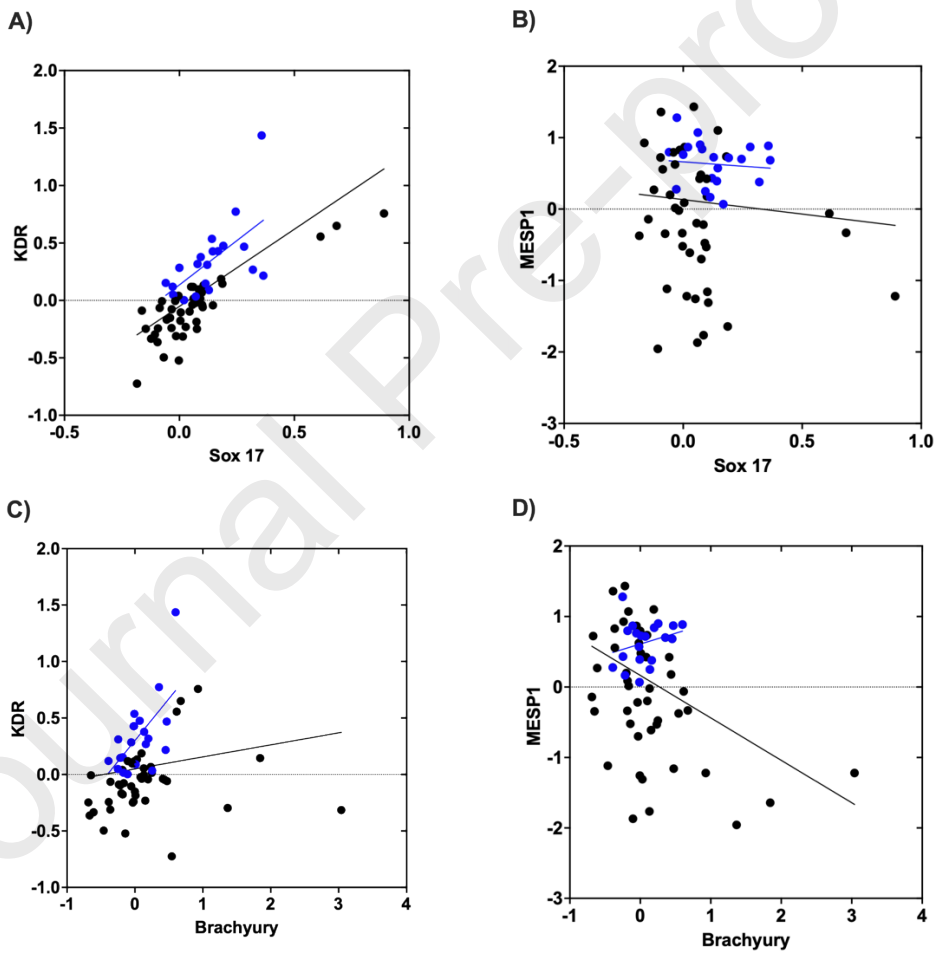

Figure S9. **Correlation of cardiac progenitor and germ layer expression on extracellular matrix proteins (ECMPs) combinations**. Mean index values for all ECMP combinations are displayed using black dots and the ECMP combinations that had positive index values for both KDR and MESP1 are displayed with blue dots. A) Correlation of KDR and Sox17 index values (black dots - r=0.7257 R^2= 0.5257 blue dots - r=0.7257 R^2= 0.5257). B) Person correlation of MESP1 and Sox17 index values ((black dots - r=-0.08958 R^2=0.008026 blue dots – r=-0.1032 R^2=0.01065). C) Pearsons correlation of KDR And T-Brachyury index values ((black dots -

r=0.1751 R^2=0.03066 blue dots - r=0.6116 R^2=0.3740). D) Pearsons correlation of MESP1 And T-Brachyury index values ((black dots - r=-0.4792 R^2=0.1664 blue dots - r=0.2682 R^2=0.07194).

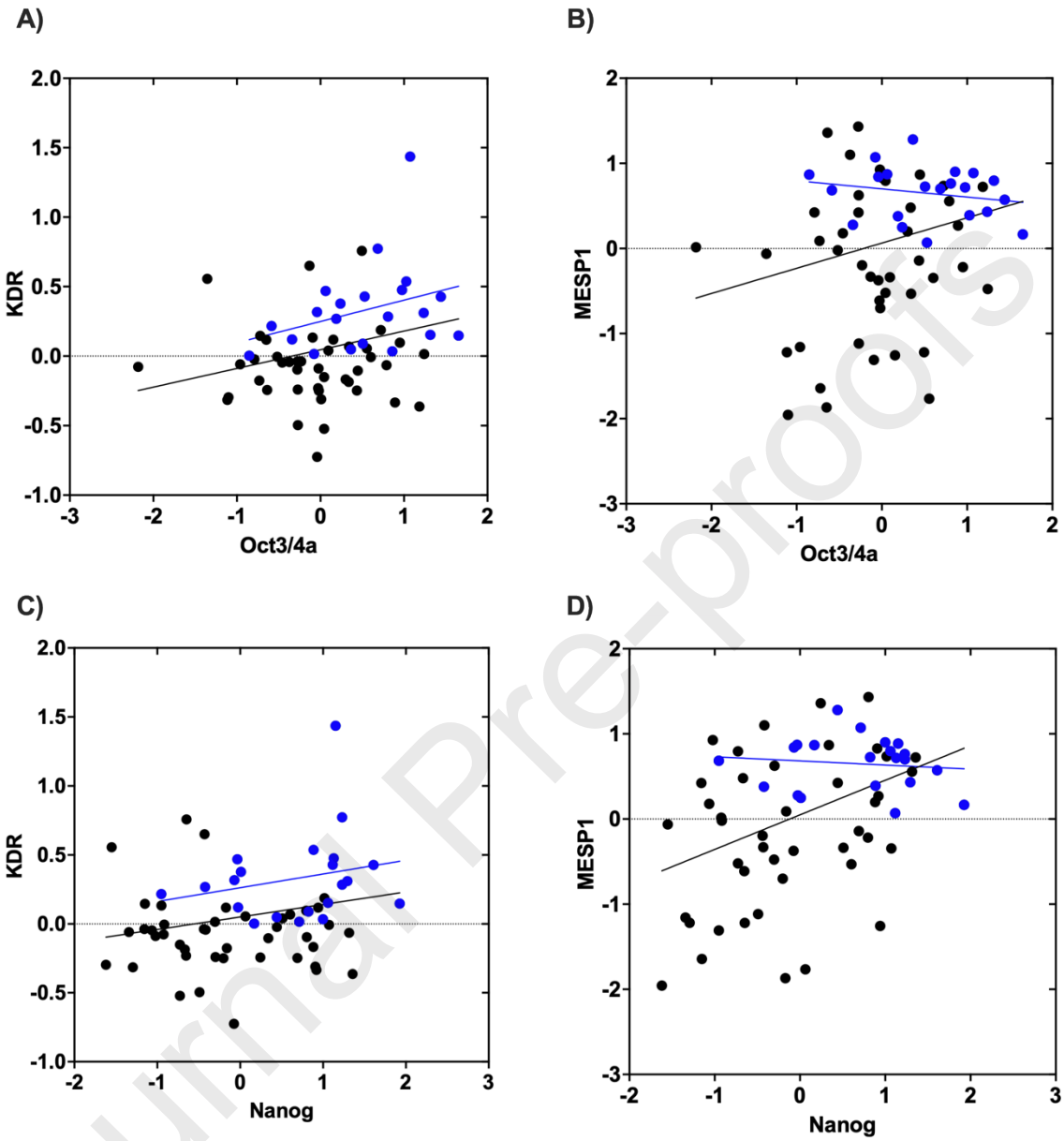

Figure S10. **Correlation of cardiac progenitor and pluripotency expression on extracellular matrix proteins (ECMPs) combinations.** Mean index values for all ECMP combinations are displayed using black dots and the ECMP combinations that had positive index values for both KDR and MESP1 are displayed with blue dots. A) Correlation of KDR and OCT3/4a index values (black dots - r=0.2892 R^2=0.08363 blue dots - r=0.3225 R^2=0.1040). B) Person correlation of MESP1 and OCT3/4a index values ((black dots - r=0.2617 R^2=0.06848 blue dots – r=-0.2076 R^2=0.04311). C) Pearsons correlation of KDR and Nanog index values ((black dots - r=0.2337 R^2=0.05465 blue dots - r=0.2242 R^2=0.05026). D) Pearsons correlation of MESP1 and Nanog index values ((black dots - r=0.4302 R^2=0.1851 blue dots - r=-0.1130 R^2=0.01276).

Finally, we wanted to investigate the relationship between cardiac progenitor markers and proliferation. In figures Figure S11 we see the correlation of MESP1 and KDR is positively correlated with proliferation (KDR:Proliferation r=0.2753 R^2=0.07581 p=0.0277. MESP1:Proliferation r=0.6617 R^2=0.4379 p=<0.0001). This is an expected result, as we saw a strong negative correlation between proliferation and pluripotency in Figure 4. Surprisingly when we isolated data points corresponding to the 21 ECMP combinations that were double positive for KDR and MESP1 (blue dots), we saw this positive correlation become weak and uncorrelated (KDR:Proliferation r=0.1150 R^2=0.01322 p=0.6293. MESP1:Proliferation r=-0.1798 R^2=0.0324 p=0.4481). Although weekly correlated, it is notable that ECMP combinations that have positive index values for both MESP1 and KDR are always present in the top end of the ECMP combinations for proliferation. Given that we see the same weak correlation result when comparing cardiac progenitor markers with pluripotency markers, it bolsters the interpretation that the hESC cells may be able to exist in multiple states within a well. This leads to the expression of pluripotency, germ layer, and cardiac progenitor markers, all expressed in the same well but not necessarily co-expressed in the same cell colonies.

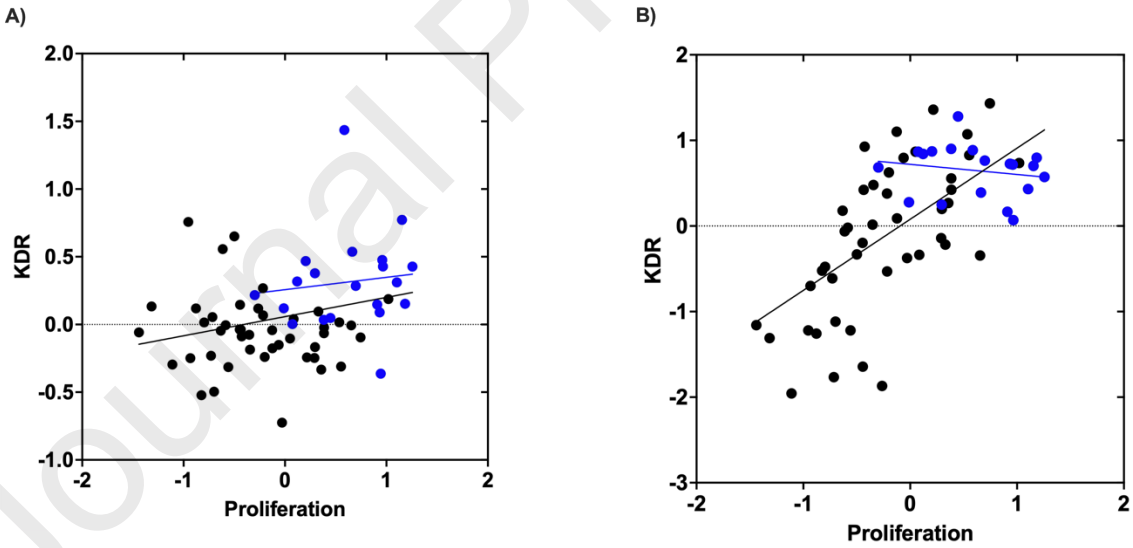

Figure S11. **Correlation of cardiac progenitor and proliferation expression on extracellular matrix proteins (ECMPs) combinations.** Mean index values for all ECMP combinations are displayed using black dots and the ECMP combinations that had positive index values for both KDR and MESP1 are displayed with blue dots. A) Correlation of MESP1 and proliferation index values (black dots - r=0.6617 R^2=0.4379 blue dots - r=0.1798 R^2=0.03234). B) Person correlation of KDR and proliferation index values ((black dots - r=0.2753 R^2=0.07581 blue dots – r=0.1150 R^2=0.01322).

By analyzing the cluster diagram and by observing the correlation of the relative index value for both KDR and MESP1, positive index values for both cardiac progenitor stains highlights that there are specific ECMP combination that promotes germ layer differentiation with specific mesoderm commitment and early cardiac lineage specification. These results are significant as they highlight that ECMP proteins can direct lineage specification before any cardiac differentiation protocol induction. Following these observations, we induce cardiac differentiation using the protocol described in the materials and methods section and analyze the effects on hESC in this array platform.

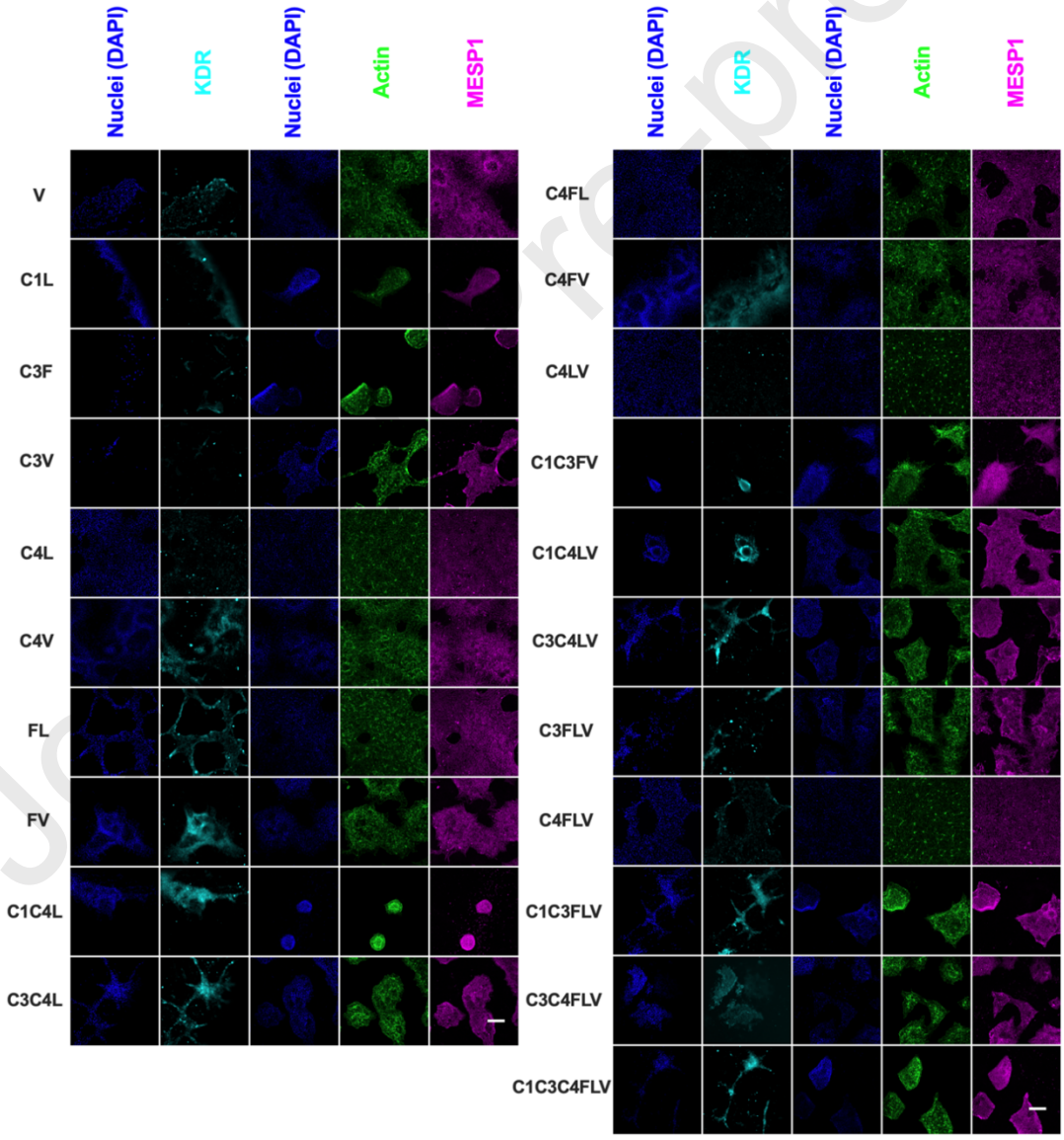

Figure S12. **Confocal images of ECMP combinations with positive index values for both KDR and MESP1.** These ECMP combinations showed high expression of KDR and MESP1 and are highlighted as ECMP combinations of interest for further study as they promote the expression of cardiac progenitor markers. Corresponding immunocytochemical stain DAPI (blue), KDR (cyan), Actin (green), and MESP1 (Magenta), scale bar is 100μm. These high-expression images refer to the biomarker intensities averaged index values around the global average mean (0). These images are representative of similar images (n=3) using a single-plane confocal image of the best representation decided by the microscope user.

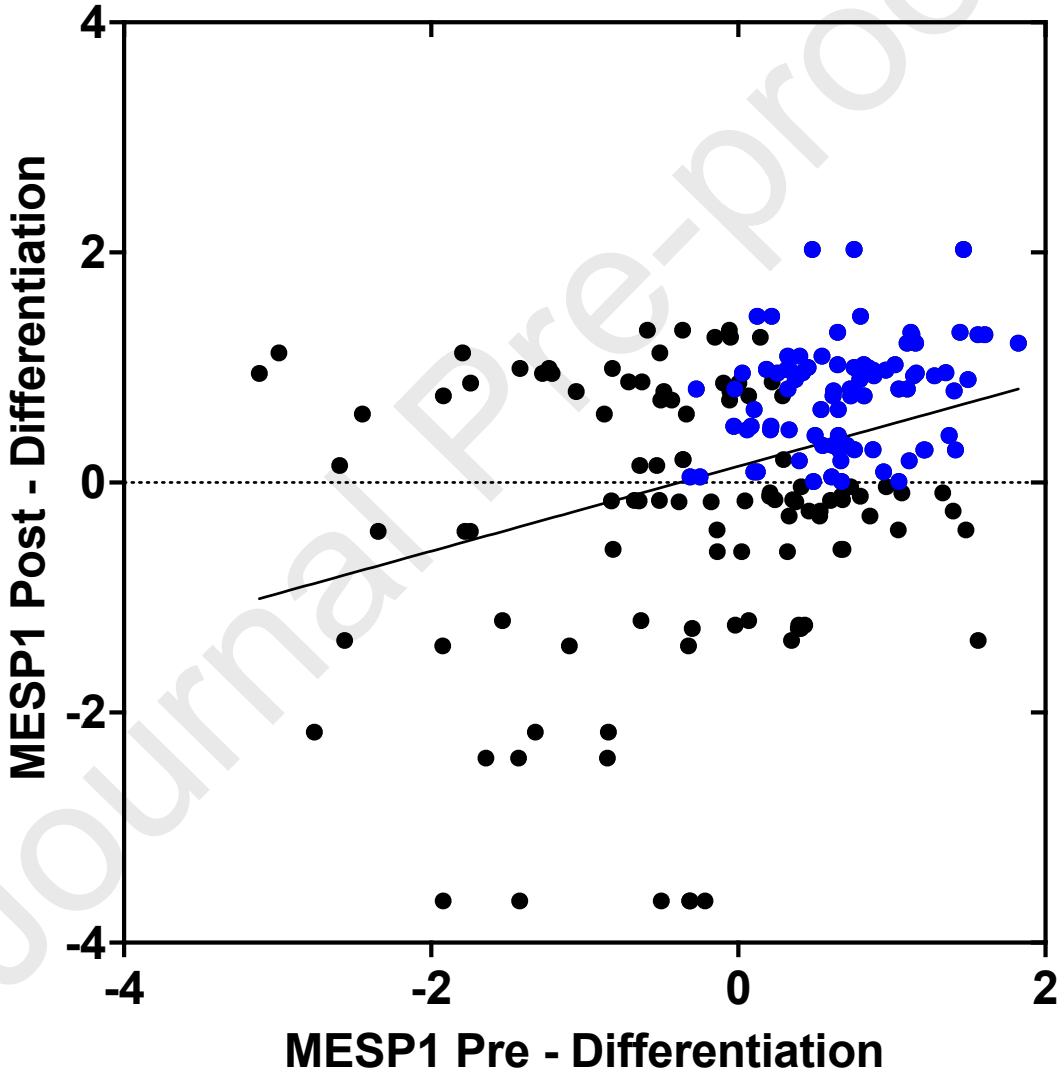

Figure S13. **Correlation of cardiac progenitor MESP1 expression on extracellular matrix proteins (ECMPs) combinations for pre and post-differentiation.** Index values for all ECMP combinations are displayed using black dots. The ECMP combinations with positive index values for both pre and post-differentiation expression of MESP1 are shown with blue dots. A) Correlation of pre and post-differentiation MESP1 index values (black dots - r=0.3243 R^2=0.1052

p=<0.0001) and correlation of double positive pre and post differentiation MESP1 index values (blue dots - r=0.2468 R^2=0.06090 p=0.0264).

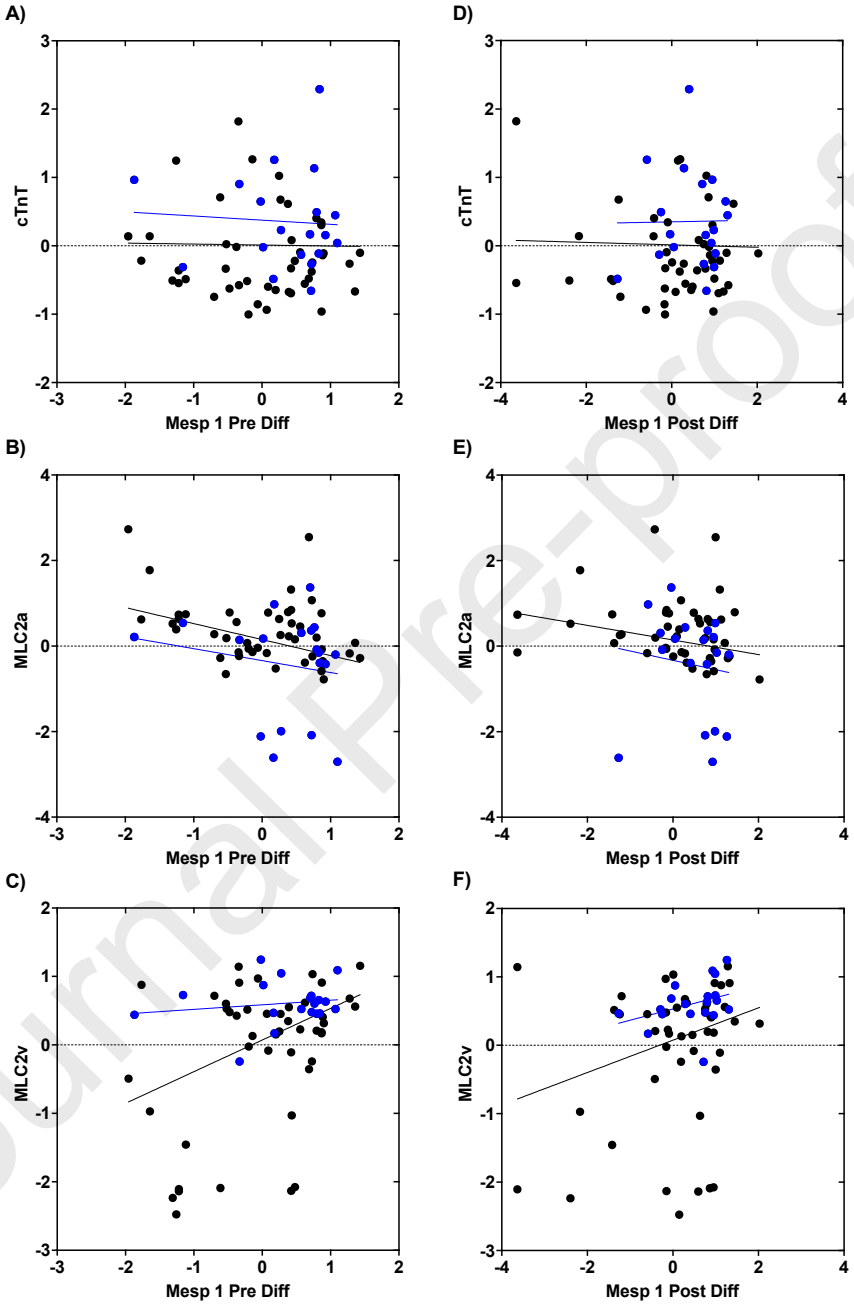

Figure S14. Correlation of cardiac progenitor MESP1 pre and post differentiation expression with mature cardiac markers on extracellular matrix proteins (ECMPs) combinations. Mean index values for all ECMP combinations are displayed using black dots and the ECMP combinations that produced contracting cardiomyocytes are displayed with blue dots. A) Correlation of MESP 1 Pre differentiation and cTnT index values (black dots - r=-0.01704 R^2=0.0002905 p=0.8937 Blue dots – r=-0.06512 R^2=0.004240 p=0.7911). B) Correlation of MESP 1 Pre differentiation and MLC2a index values (black dots - r=-0.3259 R^2=0.1062 p=0.0086 Blue dots – r=-0.1746 R^2=0.03050 p=0.4746). C) Correlation of MESP 1 Pre differentiation and MLC2v

index values (black dots - r=0.4091 R^2=0.1674 p=0.0008 Blue dots – r=0.1549 R^2=0.02400 p=0.5266). D) Correlation of MESP 1 Post differentiation and cTnT index values (black dots - r=-0.02863 R2=0.0008199 p=0.8223 Blue dots – r=0.01203 R2=0.0001448 p=0.9610). E) Correlation of MESP 1 Post differentiation and MLC2a index values (black dots - r=-0.1960 R2=0.03842 p=0.1206 Blue dots – r=-0.1227 R2=0.01506 p=0.6167). F)Correlation of MESP 1 Post differentiation and MLC2v index values (black dots - r=0.2762 R2=0.07626 p=0.0272 Blue dots – r=0.3446 R2=0.1187 p=0.1486)

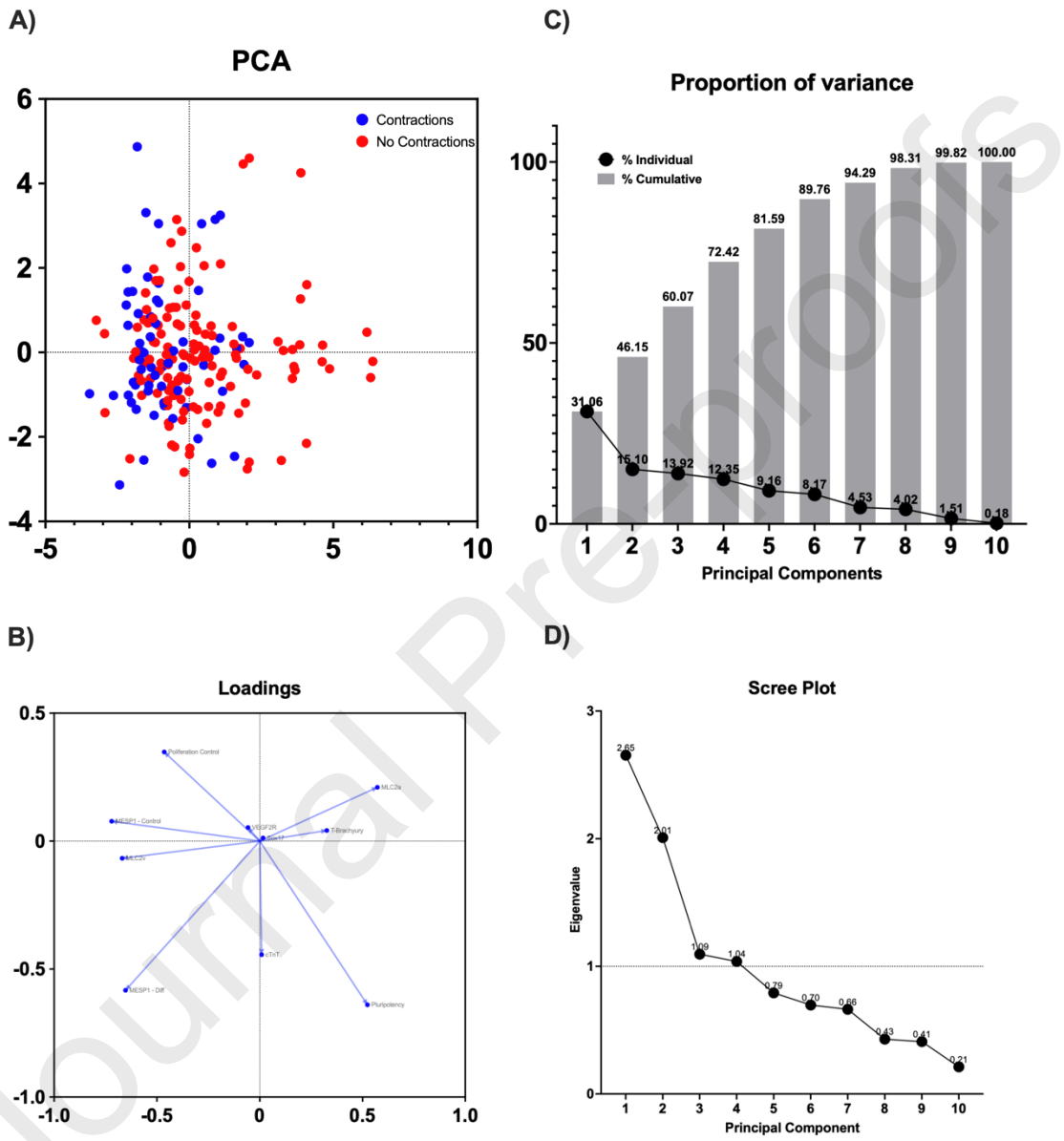

Figure S15: Principal component analysis of all 10 expression markers expression in hESC cells on 63 ECMP combinations and a Matrigel control group. A) Data points are separated into two groups, the ECMP combinations that produced contracting cardiomyocytes (blue dots) and those ECMP combinations where no cardiomyocytes were observed contracting (red dots). B) loading plot to show how strongly each biomarker influenced the principal component C) Scree plot showing the variation each principal component captured from the 10 biomarker expressions D) proportions of variance to show the percentage of variance each of the 10 biomarkers had on the principal components.

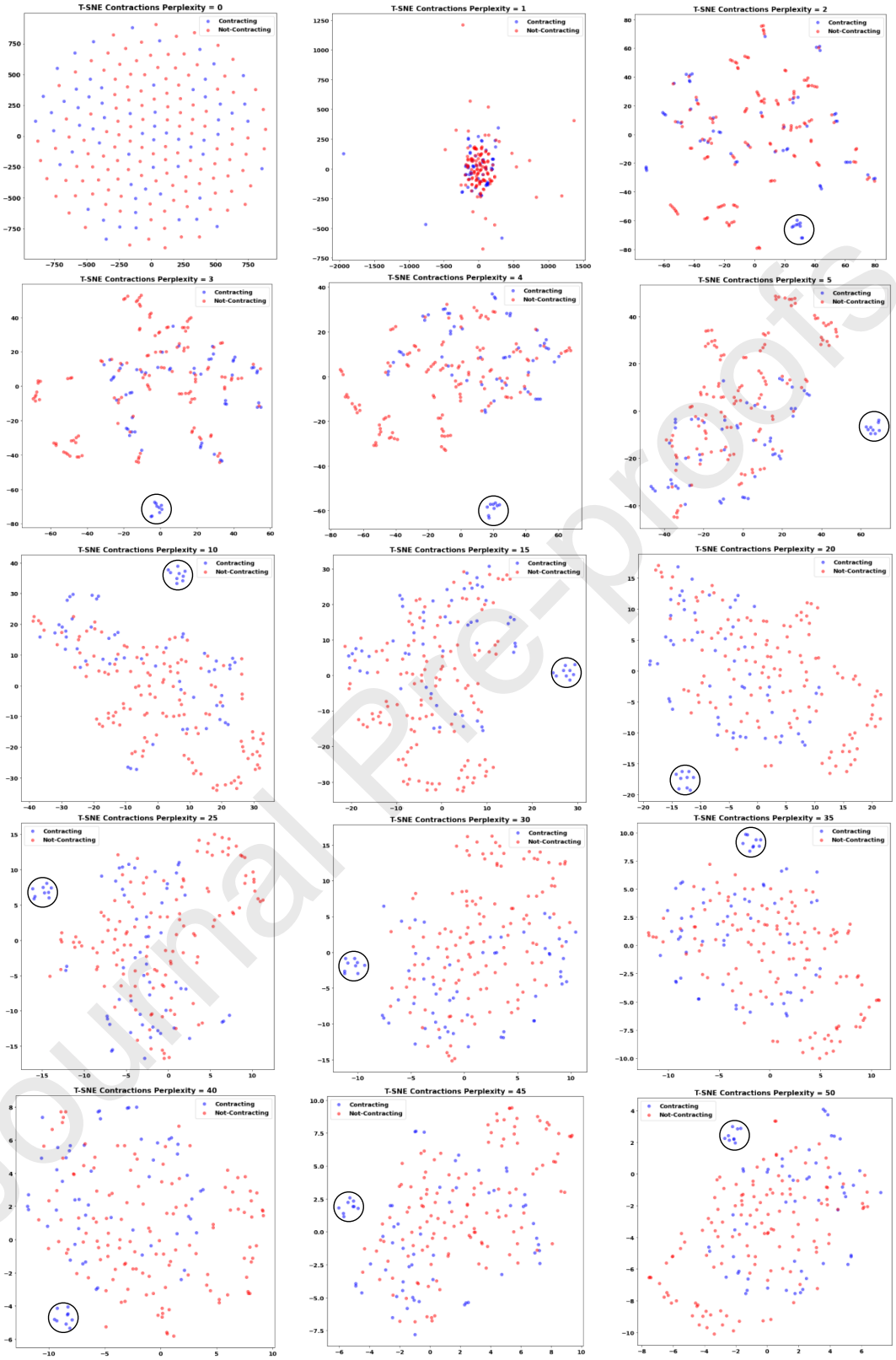

Figure S16: T-distributed stochastic neighbour embedding (t-SNE) of biomarker index data from hESC cells on 63 ECMP combinations and a Matrigel control group. Data points are separated into two groups, the ECMP combinations that produced contracting cardiomyocytes (blue dots) and those ECMP combinations where no cardiomyocytes were observed contracting

(red dots). Data is displayed in multiple graphs with the perplexity value varied between 0-50. The tight cluster of ECMP combinations (C1C3FLV, C3C4FV, and C1C3C4V) is circled in each graph.

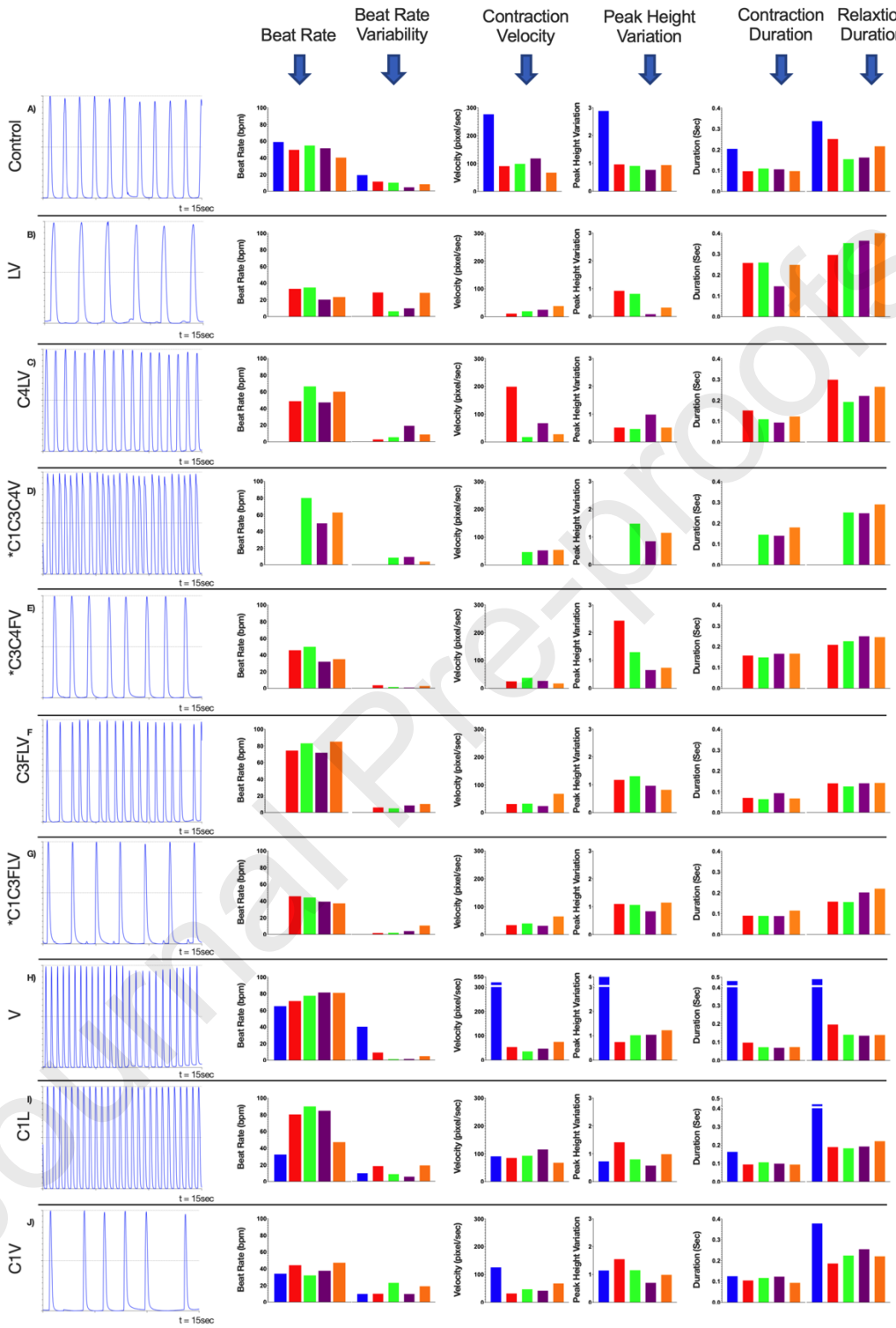

Figure S17_1 Contraction Profiles for all ECMP combinations that produced contracting cardiomyocytes. We studied and quantified the action potential (AP) morphology values of cardiomyocytes on 20 different ECMP combinations. The left panel shows the normalized peak height contraction profiles for each ECMP combination as derived from high-speed videos. These

profiles are from videos taken on day 5 after initial contraction and are representative of an average of 9 independent videos taken. The bar charts on the right show the beat rate, beat rate variation, contraction velocity, peak height variation, contraction duration, and relaxation duration of the cardiomyocytes measured over a five-day period. These mean values are averaged from three independent regions within the culture well with videos taken in triplicate with a ten-minute interval between each recording round.

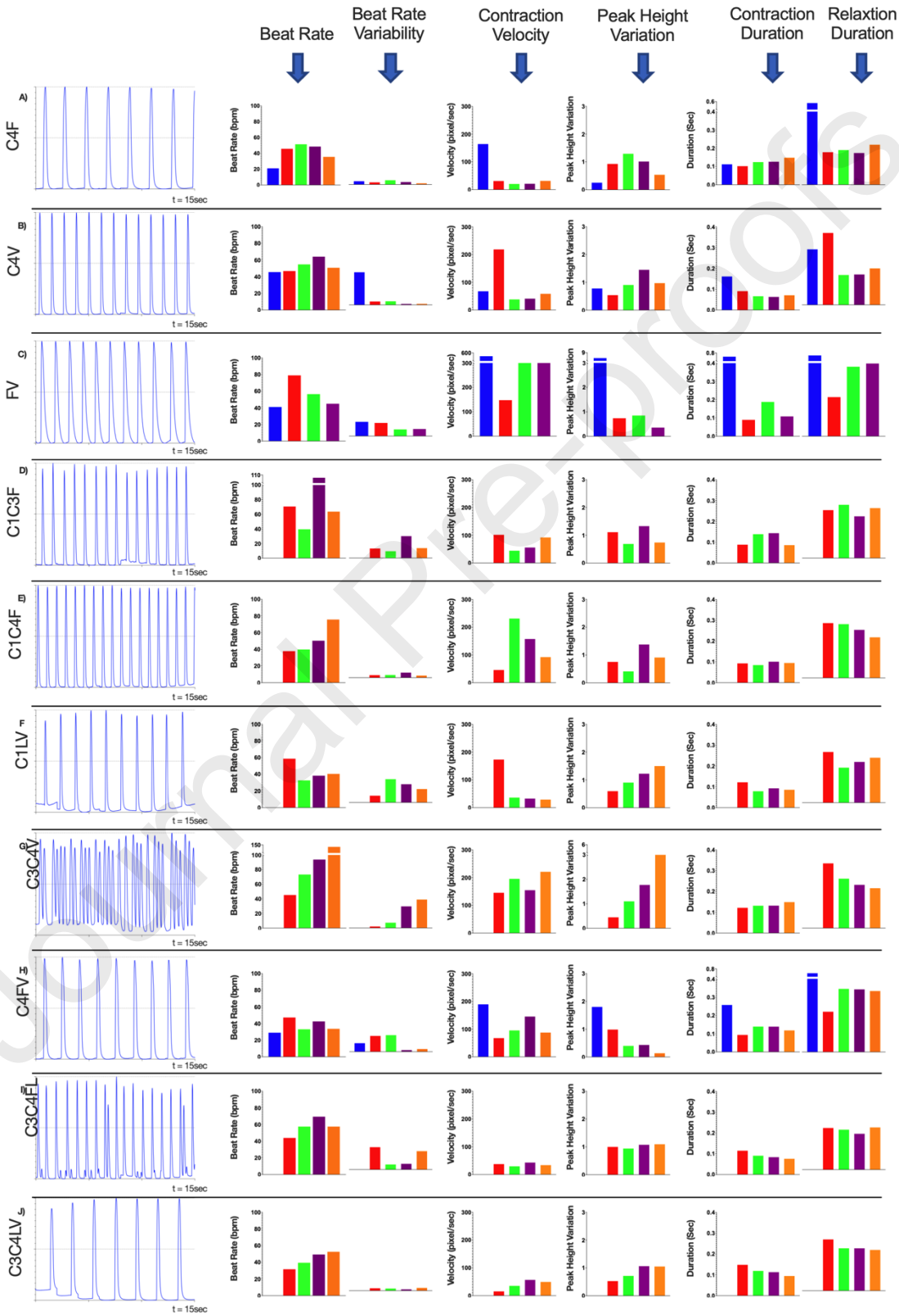

Figure S17_2 Contraction Profiles for all ECMP combinations that produced contracting cardiomyocytes. (continued from S17_1).

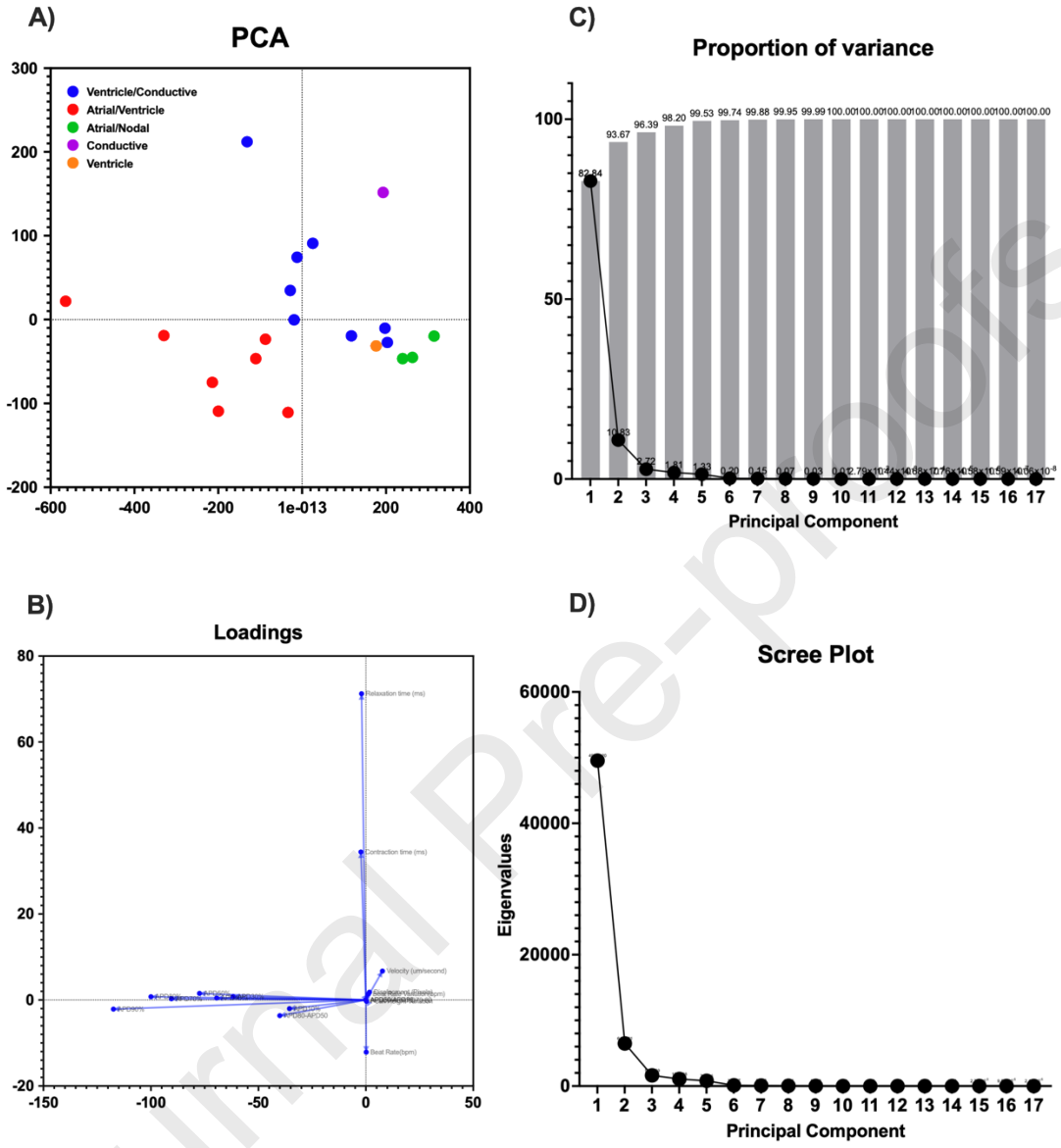

Figure S18: Principal component analysis of the action potential (AP) morphology data from the 20 ECMP combinations and a Matrigel control group that produced contracting cardiomyocytes. A) Data points are separated into five groups depending on the assigned chamber specification with ventricular/conductive (blue), atrial/ventricular (red), atrial nodal (green), conductive (purple), and ventricular (orange). B) loading plot to show how strongly each AP morphology component influenced the principal component analysis C) proportions of variance to show the percentage of variance each additional AP morphology component had on the principal components. D) Scree plot showing the eigenvalue variation of each principal component captured from the AP morphology components.

Figure S19: T-distributed stochastic neighbour embedding (t-SNE) of Action Potential (AP) morphology data from the 20 ECMP combinations and a Matrigel control group that produced contracting cardiomyocytes. Data points are separated into five groups depending on the assigned chamber specification with ventricular/conductive (blue), atrial/ventricular (red),

atrial nodal (green), conductive (purple), and ventricular (orange). Data is displayed in multiple graphs with the perplexity value varied between 0-15.

Structure	**Nodal Myocytes**	**Conduction myocytes**	**Atrial Myocytes**	**Ventricular Myocytes**
Shape	Ovoid (103)	Cylindrical (104)	Cylindrical (105, 106)	Cylindrical, bifurcated (107)
Sarcomere organization	Absent (103)	Poor (104)	Very Ordered (106)	Very ordered, Highly aligned (108, 109)
Abundance of mitochondria	Few (103)	Few (104)	Abundant (106)	Very abundant (110)
Number of Nuclei	Mono (103)		Mono, bi-nucleated (106)	Mono, bi-nucleated (108)
Electrophysiology	**Nodal Myocytes**	**Conduction myocytes**	**Atrial Myocytes**	**Ventricular Myocytes**
AP velocity	5-10μm/s	~100μm/s	~20μm/s	30-70μm/s
Notch	Absent (90)	Possible (91)	Possible (111)	Abundant (99)
Contraction Time	~100ms	~100-120ms	80-100ms	100-150ms
Relaxation Time	100-150ms	200-400ms	150-200ms	200-400ms
APD10%	40-65ms (29)	80-100ms	40-100ms (29)	80-150ms (29)
APD50%	100ms (88)	~220ms (91)	25-200ms (95, 97, 112, 98)	200-300ms (99, 98)
APD90%	150ms (88)	~300ms (91)	200-400ms (95, 97, 112, 98)	250-440+ms (99, 98)
APD30-40 /APD70-80	0.65 (29)	0.6-0.8	0.7-0.9 (29)	0.8-1.0 (29)
APD50/APD90	0.6 (100)	0.7 (100)	0.2-0.5 (100)	0.65-0.85 (100)
APD90-APD50	50ms (100)	80ms (100)	175-200ms (100)	50-130ms (100)
Molecular Markers	**Nodal Myocytes**	**Conduction myocytes**	**Atrial Myocytes**	**Ventricular Myocytes**
MLC2a			↑↑ (5, 118)	↑↑ (5, 114)
MLC2v			Absent (113, 114)	↑↑↑ (113, 114)
cTnT	↑↑↑ (78, 115, 116, 117)	↑↑ (115)	↑↑ (115)	↑↑ (115)

Table S1. Criteria for cardiomyocyte specification

Protein	Beat Rate (bpm)	Velocity (um/second)	Displacement (Pixels)	Peak Height Variation	Contraction time (ms)	Relaxation time (ms)	APD10%	APD30%	APD40%	APD50%	APD70%	APD80%	APD90%	APD30-40 /APD70-80	APD50/APD90	APD90-APD50	AP Morphology
V	47±19.04	22.03	4.45	0.99	93.500	220.356	46.40±4.90	77.20±4.58	91.20±4.40	102.80±4.58	132.40±4.36	155.20±5.10	184.40±7.12	0.61	0.56	52.40	Atrial/Nodal
C1C3F	76±2.43	29.89	4.93	0.91	94.643	194.714	41.33±9.15	90.00±5.35	107.33±5.94	128.00±4.14	170.67±5.94	193.33±4.88	228.00±4.14	0.76	0.56	65.33	Atrial/Nodal
C3C4FL	53±3.31	16.00	3.37	1.05	94.167	195.422	42.50±8.66	74.21±13.46	93.68±7.61	108.33±5.14	157.37±5.62	185.79±6.92	223.16±8.20	0.69	0.49	77.46	Atrial/Nodal
C3FLV	37±10.62	21.13	4.82	1.15	115.056	219.089	65.56±5.11	114.12±5.07	134.71±5.14	151.76±5.29	184.12±5.07	204.71±5.14	238.82±4.85	1.00	0.64	52.94	Ventricle/Conductive
C1L	47±19.04	22.03	4.45	0.99	93.500	220.356	93.08±4.71	145.77±5.04	168.46±3.68	183.85±4.96	220.00±0.00	240.77±2.72	267.69±4.30	1.09	0.69	56.92	Ventricle/Conductive
C1C4F	40±16.10	9.34	1.44	1.50	85.500	215.571	69.41±5.56	117.06±4.70	132.94±4.70	148.82±3.32	182.94±4.70	202.35±4.37	232.35±4.37	0.82	0.64	53.53	Ventricle/Conductive
CONTROL	23±28.3	12.45	4.56	0.32	248.100	408.400	112.00±15.49	204.00±6.99	230.00±4.71	260.00±4.71	314.00±5.16	354.00±5.16	416.00±5.16	0.65	0.63	94.00	Ventricle/Conductive
C4LV	63±3.73	17.63	4.17	1.15	179.667	289.333	105.88±8.70	179.41±6.59	205.88±5.07	228.82±4.85	274.12±5.07	300.00±0.00	336.47±4.93	1.02	0.68	71.18	Ventricle/Conductive
*C1C3C4V	35±2.53	5.64	2.02	0.74	166.444	245.444	76.80±10.69	189.20±5.72	215.60±5.83	240.00±5.77	284.00±5.77	318.75±53.84	337.60±6.63	0.76	0.71	78.75	Ventricle/Conductive
C1V	36±1.44	10.19	2.58	0.54	147.917	218.867	96.67±8.16	166.67±8.16	193.33±5.16	220.00±0.00	273.33±5.16	306.67±8.16	358.33±24.01	0.80	0.61	86.67	Ventricle/Conductive
C3C4V	34±3.16	28.51	7.21	0.13	118.111	333.544	78.24±20.69	153.55±17.04	182.26±13.34	207.69±12.35	253.23±13.76	281.54±10.84	340.00±10.54	1.01	0.61	73.85	Ventricle/Conductive
*C1C3FLV	81±4.67	24.26	3.24	1.22	73.000	139.043	104.29±5.35	168.57±3.78	191.43±3.78	215.71±5.35	272.86±4.88	304.29±5.35	382.86±18.90	0.73	0.56	88.57	Atrial/Ventricle
LV	60±8.62	9.07	2.30	0.52	122.856	264.089	185.00±23.45	325.00±16.43	371.67±11.69	418.33±14.72	501.67±16.02	553.33±13.66	633.33±21.60	0.90	0.66	135.00	Atrial/Ventricle
*C3C4FV	85±10.18	22.12	2.90	0.82	68.044	141.300	138.75±3.54	235.00±5.35	266.25±7.44	295.00±5.35	348.75±6.41	382.50±8.86	438.75±12.46	0.93	0.67	87.50	Atrial/Ventricle
C4F	51±1.23	18.98	2.63	0.97	70.889	175.111	140.00±5.77	230.00±5.77	265.71±5.35	291.43±3.78	350.00±0.00	390.00±0.00	455.71±7.87	0.89	0.64	98.57	Atrial/Ventricle
C4FV	58±22.07	11.01	1.52	1.09	75.989	202.689	122.22±8.33	222.22±4.41	250.00±0.00	268.89±3.33	308.89±3.33	334.44±5.27	386.67±5.00	1.09	0.70	65.56	Atrial/Ventricle
C3C4LV	40±8.05	21.87	4.10	0.94	97.809	215.791	126.67±13.66	210.00±5.77	234.29±5.35	253.33±5.16	294.29±7.87	324.29±12.72	383.33±23.38	0.81	0.66	70.95	Atrial/Ventricle
FV	64±13.50	29.91	5.44	0.74	85.500	239.750	125.45±5.22	220.00±0.00	254.55±5.22	300.00±0.00	384.55±6.88	450.00±10.00	570.91±19.73	0.53	0.53	150.00	Atrial/Ventricle
C1LV	137±38.84	71.79	18.97	5.46	148.643	191.643	65.56±7.26	119.00±8.76	136.00±5.16	157.00±4.83	189.00±3.16	211.00±3.16	261.00±15.24	0.77	0.60	54.00	Ventricle
C4V	45±8.48	113.46	20.34	0.35	108.611	397.689	73.08±4.80	120.77±2.77	135.38±5.19	153.85±5.06	184.62±5.19	206.92±4.80	240.77±4.94	0.66	0.64	53.08	Conductive

Table S2. Summary of contraction profiles and action potential morphologies

DNA Stains							
Antibody	Company	Catalog number			Dilution		
DAPI	Merck	F6057			immersed		
Hoescht 33342	ThermoFisher Scientific	62249			1-300		
Primary Antibodies							
Antibody	Company	Catalog number	Conjugated	Animmal host	Dilution	Specification	clonal
T-brachyury	Abcam	ab209665	n/a	Rabbit	1-300	Human, Mouse, Rat	Monoclonal
Sox17	ThermoFisher Scientific	*OTI2G8*	n/a	Mouse	1-300	Dog, Human	Polyclonal
OCT3/4a	Abcam	ab27985	n/a	Goat	1-300	Human, Mouse, Rat	Polyclonal
Nanog	Invitrogen	14-5768-82	n/a	Mouse	1-300	Human	Monoclonal
MESP1	Novus/Invitrogen	NOVNBP151 613	n/a	Mouse	1-300	Human, Mouse	Monoclonal
VEGF2R/KDR/ FLK1	G-Biosciences	ITA1858	Alexa Fluro 594	Rabbit	1-300	Human, Mouse, Rat	Polyclonal
C-TNNT	G-Biosciences	ITA6344	Alexa Fluro 647	Rabbit	1-300	Human, Mouse, Rat	Polyclonal
MLC2a	Synaptic Systems	311011	n/a	Mouse	1-300	Human, Mouse, Rat	Monoclonal
MLC2v	ProteinTech	10906-1-AP	n/a	Rabbit	1-300	Human, Mouse, Rat, Monkey, Zebrafish	Polyclonal
Secondary Antibodies							
Antibody	Company	Catalog number	Conjugated	Animmal host	Dilution	Specification	clonal
Anti-Mouse 647	Merck	SAB4600182	CF 647	Goat	1-300	Mouse	polyclonal

Anti-Goat 647	ThermoFisher Scientific	A32849	AF 647	Donkey	1-300	Goat	polyclonal
Anti-Rabbit 555	Merck	SAB4600068	CF 555	Goat	1-300	Rabbit	Polyclonal
Anti-Mouse 555	Merck	SAB4600060	CF555	Donkey	1-300	Mouse	Polyclonal
Anti-Rabbit 647	Merck	SAB4600184	CF 647	Goat	1-300	Rabbit	Polclonal
Anti-mouse 488	Merck	62197	ATTO 488	Goat	1-300	Mouse	Polyclonal
Anti-Rabbit 488	Merck	18772	ATTO 488	Goat	1-300	Rabbit	Polyclonal
Rodamin Phalloidin	Merck	P1951	532nm	Death Cap Mushroom	1-500		
647 phalloidin	Merck	65906	ATTO 647N		1-500		
488 Phalloidin	Merck	49409	ATTO 488		1-500		

Table S3. Summary of primary, secondary, and nucleic stains used in this study. Company name and catalog number are provided for the Australian branches or distributors.

Supporting Materials and Methods

MANOVA Statistical analysis performed in Jupiter Notebook

First import the index values in triplicate for the 6 biomerkers of interest.

All this work is being performed Post-hoc but we will perform the follwing stat tests with an a priori assumption and use the results to guide our sample size for follow up experiments.

Our null hypothesis is that all biomarker expression is equal in the hESC cells when cultured on matrigel and the three ECMP combinations.

In [1]:
```
import pandas as pd
from dfply import *
```

In [2]:
```
df=pd.read_csv("/Users/jakeireland/Desktop/ECMP_manova/biomarker_index_va
df.head(12)
```

Out[2]:

	ECMP	Brachyury	VEGF2R	MESP1_pre	Cardiac_Troponin	MLC2a	MLC2v
0	Control	-0.567480	0.001326	-0.317131	2.382947	-0.256828	1.222423
1	Control	-0.589210	0.032750	-0.216395	0.972971	-0.050736	1.102282
2	Control	-0.789036	-0.054707	-0.501197	2.105462	-0.130873	1.102227
3	C1C3C4V	-0.164387	-0.271513	1.276741	0.692673	-2.932961	1.127341
4	C1C3C4V	0.548269	0.186899	0.882933	-0.139654	-2.704976	1.090379
5	C1C3C4V	0.191941	-0.042307	1.142349	-0.426744	-2.476990	1.053416
6	C3C4FV	-0.011045	-0.234834	-0.050669	0.519584	-2.462966	1.264612
7	C3C4FV	0.147950	0.401330	-0.152777	0.550871	-2.112189	1.246099
8	C3C4FV	0.259005	-0.181223	0.142656	0.876184	-1.761411	1.227586
9	C1C3FLV	-0.136764	0.216400	0.315105	0.480966	-1.899717	1.329818
10	C1C3FLV	-0.641799	0.023257	0.183345	0.427584	-2.150255	0.633982
11	C1C3FLV	-0.389281	0.119828	0.332640	-0.218072	-1.920614	1.172446

Get summary statistics based on each independant variable

In [3]:
```
df >> group_by(X.ECMP) >> summarize(n=X['Brachyury'].count(), mean=X['Bra
```

Out[3]:

	ECMP	n	mean	std
0	C1C3C4V	3	0.191941	0.356328
1	C1C3FLV	3	-0.389281	0.252518
2	C3C4FV	3	0.131970	0.135732
3	Control	3	-0.648575	0.122127

In [4]:
```
df >> group_by(X.ECMP) >> summarize(n=X['VEGF2R'].count(), mean=X['VEGF2R
```

Out[4]:

	ECMP	n	mean	std
0	C1C3C4V	3	-0.042307	0.229206
1	C1C3FLV	3	0.119828	0.096572
2	C3C4FV	3	-0.004909	0.352833
3	Control	3	-0.006877	0.044302

In [5]:
```
df >> group_by(X.ECMP) >> summarize(n=X['MESP1_pre'].count(), mean=X['MES
```

Out[5]:

	ECMP	n	mean	std
0	C1C3C4V	3	1.100675	0.200184
1	C1C3FLV	3	0.277030	0.081606
2	C3C4FV	3	-0.020264	0.150045
3	Control	3	-0.344908	0.144418

In [6]:
```
df >> group_by(X.ECMP) >> summarize(n=X['Cardiac_Troponin'].count(), mean
```

Out[6]:

	ECMP	n	mean	std
0	C1C3C4V	3	0.042092	0.581418
1	C1C3FLV	3	0.230159	0.389096
2	C3C4FV	3	0.648880	0.197472
3	Control	3	1.820460	0.746945

In [7]:
```
df >> group_by(X.ECMP) >> summarize(n=X['MLC2a'].count(), mean=X['MLC2a']
```

Out[7]:

	ECMP	n	mean	std
0	C1C3C4V	3	-2.704975	0.227985
1	C1C3FLV	3	-1.990196	0.139009
2	C3C4FV	3	-2.112189	0.350777
3	Control	3	-0.146146	0.103891

In [8]:
```
df >> group_by(X.ECMP) >> summarize(n=X['MLC2v'].count(), mean=X['MLC2v']
```

Out[8]:

	ECMP	n	mean	std
0	C1C3C4V	3	1.090379	0.036962
1	C1C3FLV	3	1.045416	0.364896
2	C3C4FV	3	1.246099	0.018513
3	Control	3	1.142311	0.069379

Visualize datasets in box plots

In [9]:
```
import seaborn as sns
import matplotlib.pyplot as plt
```

In [10]:
```
fig, axs = plt.subplots(ncols=1)
sns.swarmplot(data=df, x="ECMP", y="Brachyury", hue=df.ECMP.tolist())
plt.show()
fig, axs = plt.subplots(ncols=1)
sns.swarmplot(data=df, x="ECMP", y="VEGF2R", hue=df.ECMP.tolist())
plt.show()
fig, axs = plt.subplots(ncols=1)
sns.swarmplot(data=df, x="ECMP", y="MESP1_pre", hue=df.ECMP.tolist())
plt.show()
fig, axs = plt.subplots(ncols=1)
sns.swarmplot(data=df, x="ECMP", y="Cardiac_Troponin", hue=df.ECMP.tolist
plt.show()
fig, axs = plt.subplots(ncols=1)
sns.swarmplot(data=df, x="ECMP", y="MLC2a", hue=df.ECMP.tolist())
plt.show()
fig, axs = plt.subplots(ncols=1)
sns.swarmplot(data=df, x="ECMP", y="MLC2v", hue=df.ECMP.tolist())
plt.show()
```

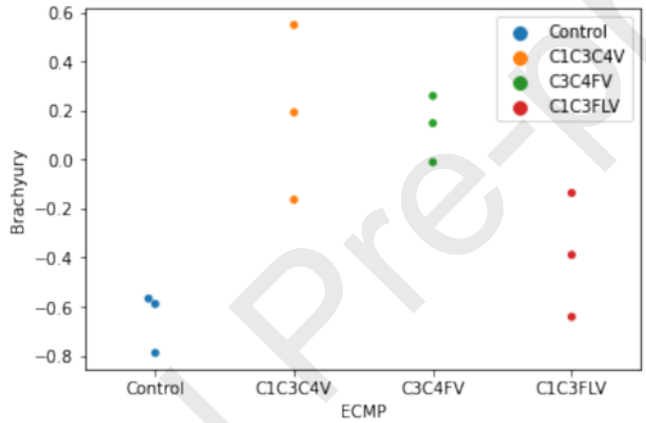

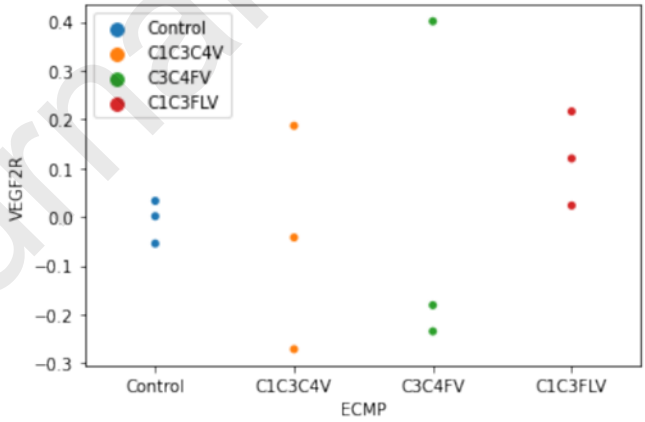

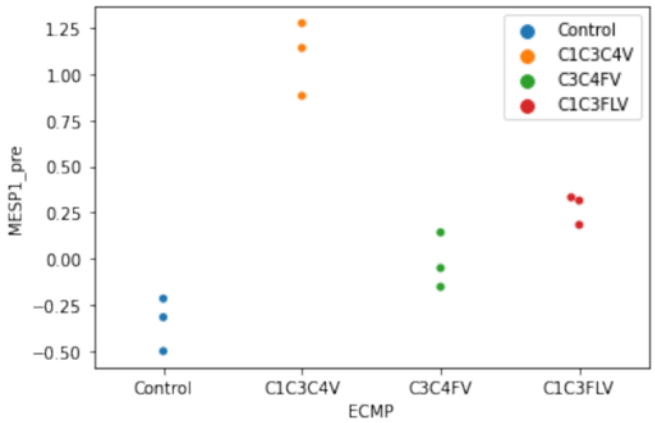

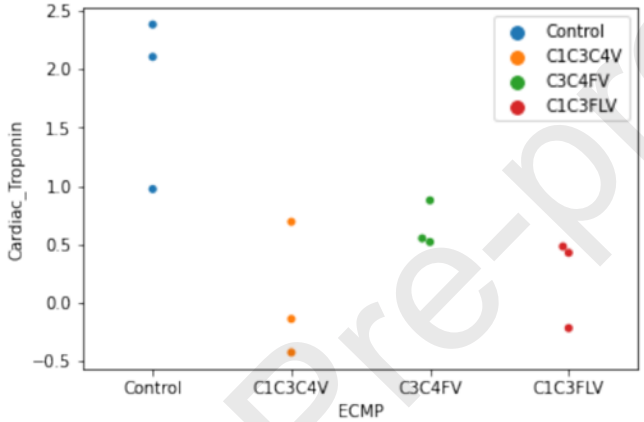

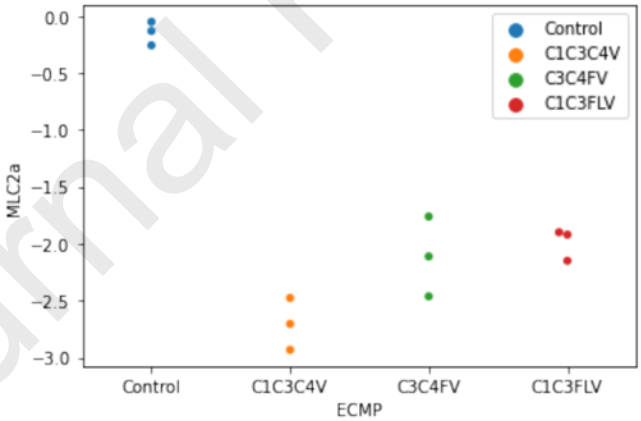

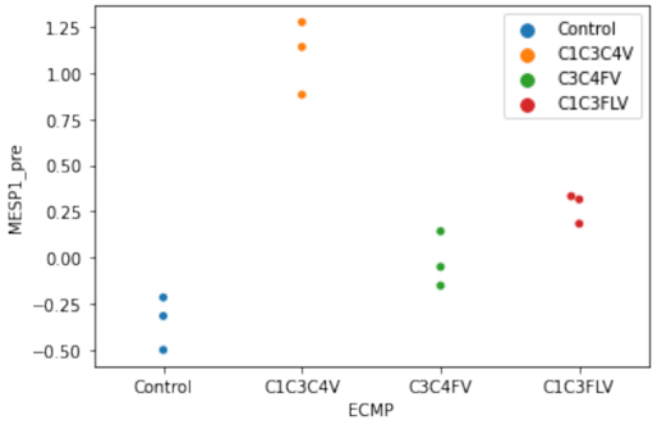

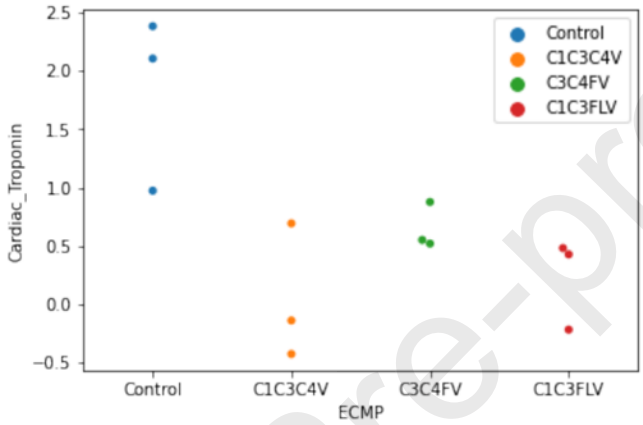

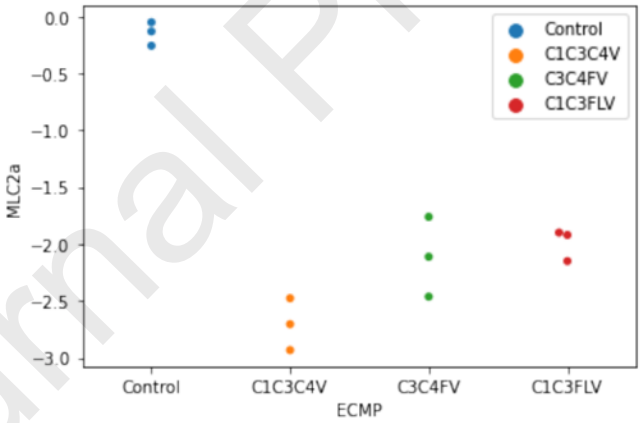

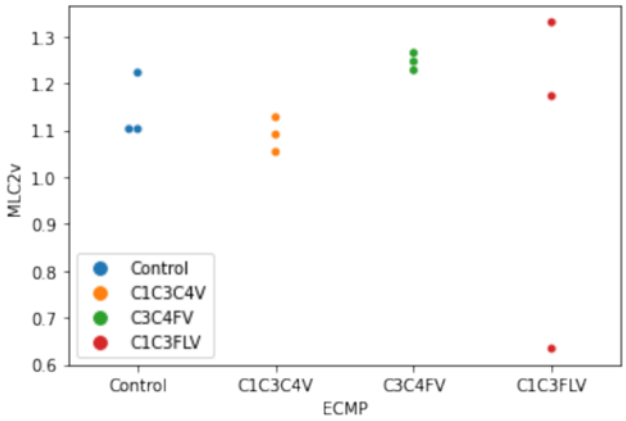

perform one-way MANOVA

MANOVA has the following assumptions

1. independant groups
2. multivariant normality
3. homogenity of the coveriance matricies
4. no multicollinarity
5. liniear relationship of dependant variables

In [22]:
```
import math

df.hist(alpha=0.7,
        column=["Brachyury", "VEGF2R", "MESP1_pre", "Cardiac_Troponin", "
        grid=True,
        figsize=(10, 10),
        legend=True,
        bins=20)
plt.xlabel('Index values');
```

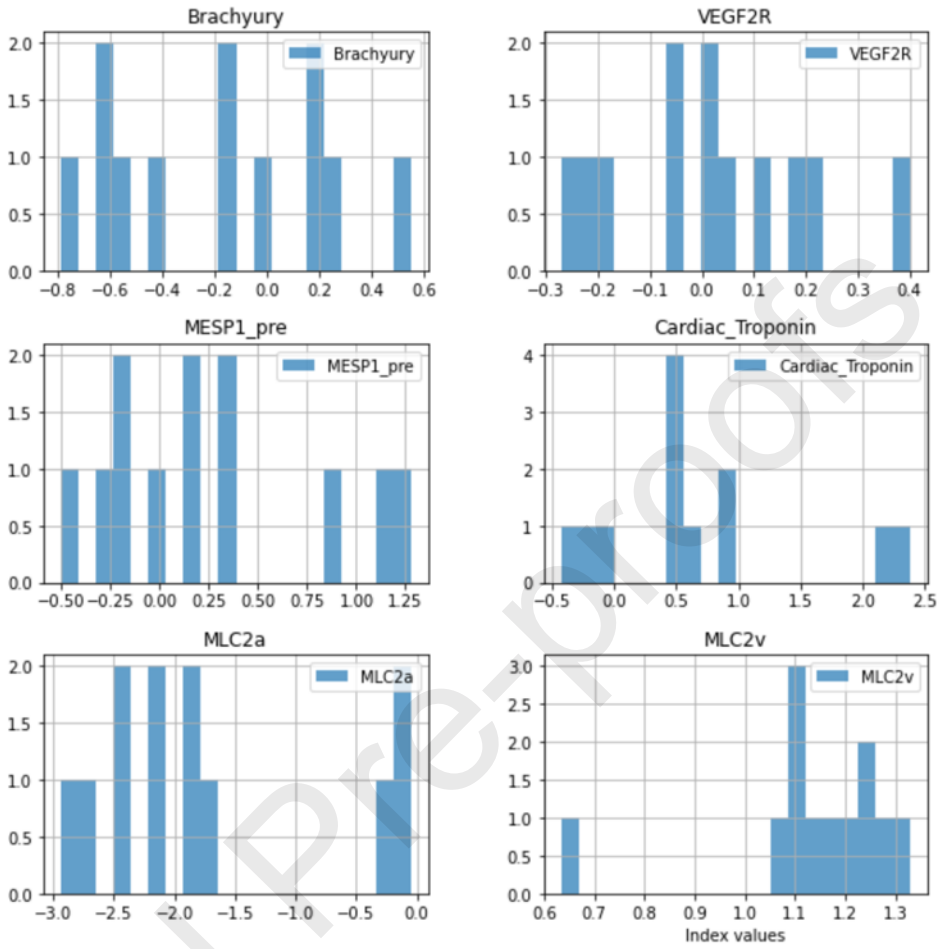

In [23]:
```
from scipy.stats import shapiro
import statsmodels.api as sm


fig = sm.qqplot(df['Brachyury'], line='q')
plt.show()
shapiro(df['Brachyury'])
```

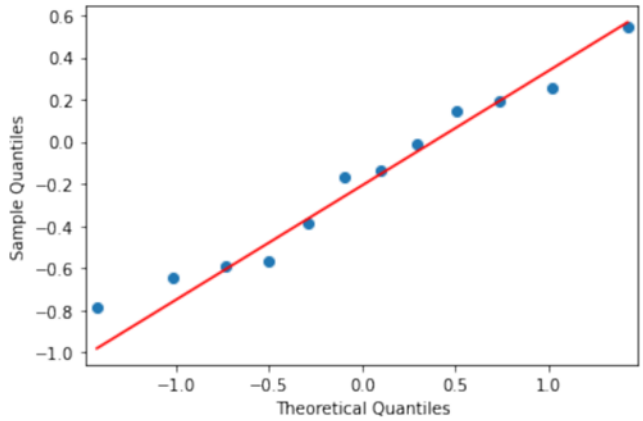

Out[23]: ShapiroResult(statistic=0.9569190144538879, pvalue=0.739113450050354)

In [24]:
```
fig = sm.qqplot(df['VEGF2R'], line='q')
plt.show()
shapiro(df['VEGF2R'])
```

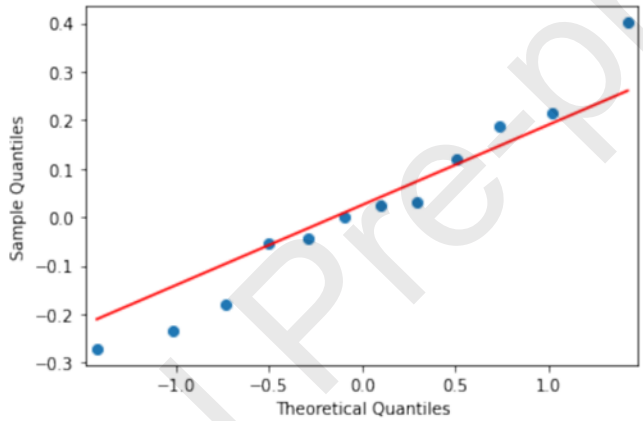

Out[24]: ShapiroResult(statistic=0.9707323312759399, pvalue=0.9183229804039001)

In [25]:
```
fig = sm.qqplot(df['MESP1_pre'], line='q')
plt.show()
shapiro(df['MESP1_pre'])
```

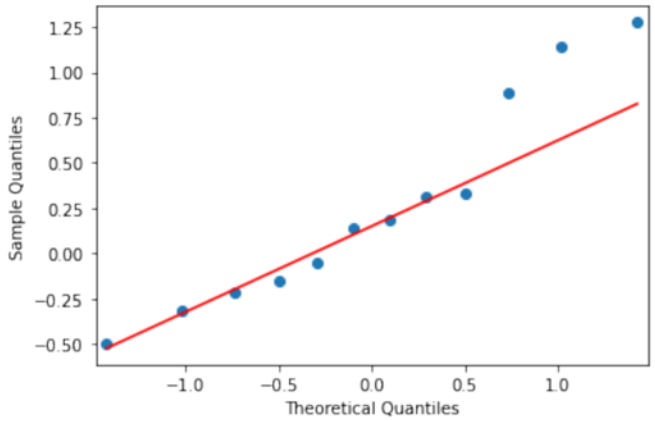

Out[25]: ShapiroResult(statistic=0.9201974868774414, pvalue=0.2875524163246155)

In [26]:
```
fig = sm.qqplot(df['Cardiac_Troponin'], line='q')
plt.show()
shapiro(df['Cardiac_Troponin'])
```

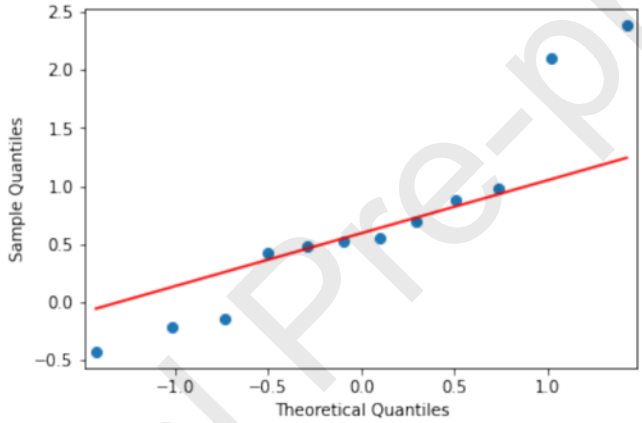

Out[26]: ShapiroResult(statistic=0.8975018262863159, pvalue=0.14726729691028595)

In [27]:
```
fig = sm.qqplot(df['MLC2a'], line='q')
plt.show()
shapiro(df['MLC2a'])
```

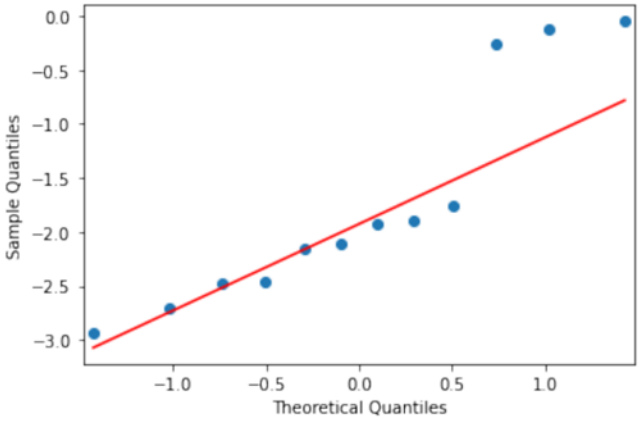

Out[27]: ShapiroResult(statistic=0.8382189273834229, pvalue=0.02634250558912754)

In [28]:
```
fig = sm.qqplot(df['MLC2v'], line='q')
plt.show()
shapiro(df['MLC2v'])
```

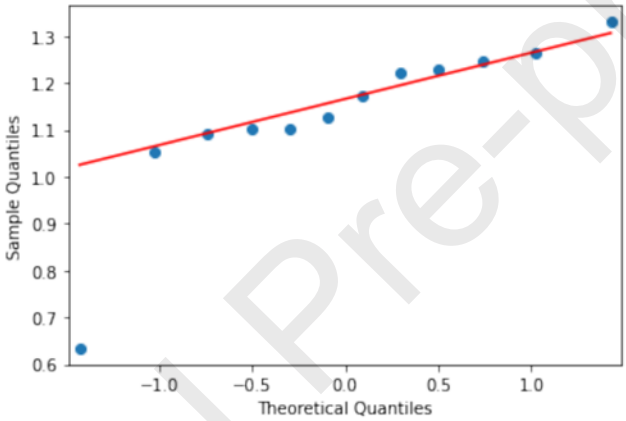

Out[28]: ShapiroResult(statistic=0.7808288335800171, pvalue=0.005718437023460865)

In [29]:
```
df.cov()
```

Out[29]:

	Brachyury	VEGF2R	MESP1_pre	Cardiac_Troponin	MLC2a	Ml
Brachyury	0.176836	0.011015	0.133020	-0.213072	-0.297707	0.02
VEGF2R	0.011015	0.038368	-0.020266	-0.034842	0.009292	0.00
MESP1_pre	0.133020	-0.020266	0.330372	-0.332544	-0.450866	-0.01
Cardiac_Troponin	-0.213072	-0.034842	-0.332544	0.718644	0.669380	0.02
MLC2a	-0.297707	0.009292	-0.450866	0.669380	1.038933	0.01
MLC2v	0.024320	0.002834	-0.014813	0.023335	0.014972	0.03
group	0.097897	0.056934	0.101574	-0.567834	-0.673549	-0.01

In [30]:
```
import pingouin as pg
df['group'] = [1] * 3 + [2] * 3 + [3] * 3 + [4] * 3
df.head()
```

Out[30]:

	ECMP	Brachyury	VEGF2R	MESP1_pre	Cardiac_Troponin	MLC2a	MLC2v
0	Control	-0.567480	0.001326	-0.317131	2.382947	-0.256828	1.222423
1	Control	-0.589210	0.032750	-0.216395	0.972971	-0.050736	1.102282
2	Control	-0.789036	-0.054707	-0.501197	2.105462	-0.130873	1.102227
3	C1C3C4V	-0.164387	-0.271513	1.276741	0.692673	-2.932961	1.127341
4	C1C3C4V	0.548269	0.186899	0.882933	-0.139654	-2.704976	1.090379

In [31]:
```
pg.box_m(df, dvs=['Brachyury', 'VEGF2R', 'MESP1_pre', 'Cardiac_Troponin',
```

Out[31]:

	Chi2	df	pval	equal_cov
box	-378.931401	63.0	1.0	True

Before performing we have tested the following assumptions

1. independant groups

Yes all groups are indipendant

1. multivariant normality

We find from our normality test that all data set accept MLC2a and MLC2v are normally distributed.

1. homogenity of the coveriance matricies

Using the dataframe covariance test and the M box test we find there is homogenity of covariance matresies

1. no multicollinarity

cannot test with more than two variable

1. liniear relationship of dependant variables

cannot test with more than two varaibles

In [32]:
```
from statsmodels.multivariate.manova import MANOVA
fit = MANOVA.from_formula('Brachyury + VEGF2R + MESP1_pre + Cardiac_Tropo
print(fit.mv_test())
```

```
                    Multivariate linear model
================================================================

----------------------------------------------------------------
          Intercept         Value   Num DF Den DF F Value Pr > F
----------------------------------------------------------------
             Wilks' lambda   0.0050 6.0000 3.0000 99.8060 0.0015
            Pillai's trace   0.9950 6.0000 3.0000 99.8060 0.0015
    Hotelling-Lawley trace 199.6120 6.0000 3.0000 99.8060 0.0015
       Roy's greatest root 199.6120 6.0000 3.0000 99.8060 0.0015
----------------------------------------------------------------

----------------------------------------------------------------
          ECMP           Value    Num DF  Den DF F Value  Pr > F
----------------------------------------------------------------
          Wilks' lambda   0.0002 18.0000  8.9706   8.9792 0.0010
         Pillai's trace   2.5068 18.0000 15.0000   4.2354 0.0035
 Hotelling-Lawley trace 195.6523 18.0000  2.6667  43.4783 0.0081
    Roy's greatest root 186.8769  6.0000  5.0000 155.7308 0.0000
================================================================
```

The Pillai's Trace test statistics is statistically significant [Pillai's Trace = 2.5068, F(18, 15) = 4.2354, p = 0.0035] and indicates that ECMP substrates composition has a statistically significant association the biomarker expression levels. We thus reject the null hypothesis that the biomarker expression levels are equal between the matrigel and ECMP combinations.

post-hoc test.

Here we will perform the linear discriminant analysis (LDA) using sklearn to see the differences between each group. LDA will discriminate the groups using information from all the independent variables (biomarker index values).

In [33]:
```
from sklearn.discriminant_analysis import LinearDiscriminantAnalysis as l
from mpl_toolkits.mplot3d import Axes3D
```

In [34]:
```
X = df[["Brachyury", "VEGF2R", "MESP1_pre", "Cardiac_Troponin", "MLC2a",
y = df["ECMP"]
post_hoc = lda().fit(X=X, y=y)
```

In [35]:
```
post_hoc.priors_
```

Out[35]:
```
array([0.25, 0.25, 0.25, 0.25])
```

In [36]:
```
post_hoc.means_
```

Out[36]:
```
array([[ 0.19194101, -0.04230683,  1.10067452,  0.04209173, -2.7049755 ,
         1.09037852],
       [-0.38928142,  0.11982827,  0.27702999,  0.23015926, -1.99019553,
         1.04541557],
       [ 0.13197014, -0.00490932, -0.02026355,  0.64887977, -2.11218897,
         1.24609904],
       [-0.6485754 , -0.00687718, -0.34490767,  1.82045991, -0.1461458 ,
         1.14231085]])
```

In [37]:
```
post_hoc.scalings_
```

Out[37]:
```
array([[ 4.71599436, -2.81108968, -4.23309929],
       [ 2.18489516,  4.25017159,  2.62383414],
       [ 8.54358301,  6.22969748, -1.21319743],
       [-0.14223803,  0.52283996, -1.18340767],
       [-5.75732331,  2.07940376, -1.23126934],
       [-4.00211623, -1.87330433,  1.60898969]])
```

In [38]:
```
post_hoc.explained_variance_ratio_
```

Out[38]:
```
array([0.95514805, 0.03589252, 0.00895942])
```

In [39]:
```
X_new = pd.DataFrame(lda().fit(X=X, y=y).transform(X), columns=["lda1", "
X_new["ECMP"] = df["ECMP"]
sns.scatterplot(data=X_new, x="lda1", y="lda2", hue=df.ECMP.tolist())
plt.show()
```

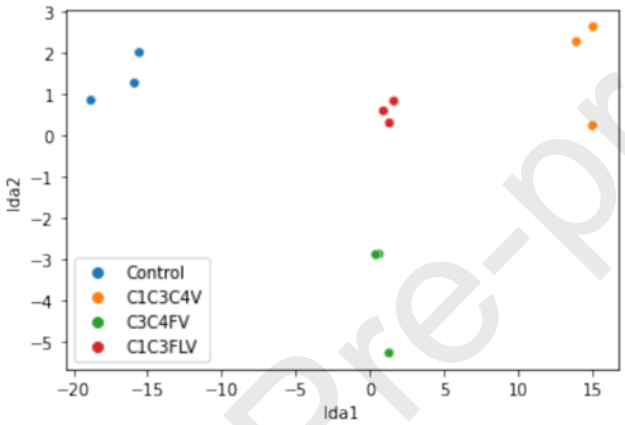

In [40]:
```
fig = plt.figure()
ax = fig.add_subplot(111, projection = '3d')

x = X_new['lda1']
y = X_new['lda2']
z = X_new['lda3']

ax.set_xlabel("lda1")
ax.set_ylabel("lda2")
ax.set_zlabel("lda3")

ax.scatter(x, y, z)
plt.show()
```

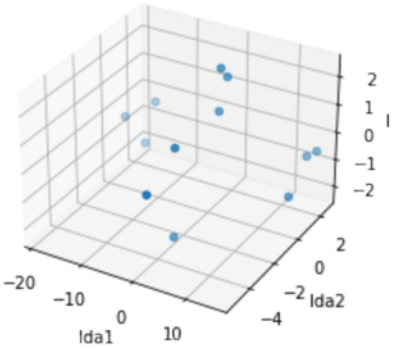

The LDA scatter plot discriminates against multiple ECMP combinations based on the biomarker index values (independant variables). All ECMP combinations are well seperated indicating a significant difference between all ECMP combinations.

More Post-Hoc tests

Perform multiple ANOVA tests between the 4 ECMP combiantions and the individual biomarkers.

In [41]:
```
import statsmodels.api as sm
from statsmodels.formula.api import ols
from bioinfokit.analys import stat
```

In [42]:
```
res = stat()
res.anova_stat(df=df, res_var='Brachyury', anova_model='Brachyury ~ (ECMP
res.anova_summary
```

Out[42]:

	df	sum_sq	mean_sq	F	PR(>F)
ECMP	3.0	1.497054	0.499018	8.908121	0.00626
Residual	8.0	0.448147	0.056018	NaN	NaN

In [43]:
```
model = ols('Brachyury ~ (ECMP)', data=df).fit()
anova_table = sm.stats.anova_lm(model, typ=2)
anova_table
```

Out[43]:

	sum_sq	df	F	PR(>F)
ECMP	1.497054	3.0	8.908121	0.00626
Residual	0.448147	8.0	NaN	NaN

In [44]:
```
model = ols('VEGF2R ~ (ECMP)', data=df).fit()
anova_table = sm.stats.anova_lm(model, typ=2)
anova_table
```

Out[44]:

	sum_sq	df	F	PR(>F)
ECMP	0.045419	3.0	0.321584	0.809846
Residual	0.376631	8.0	NaN	NaN

In [45]:
```
model = ols('MESP1_pre ~ (ECMP)', data=df).fit()
anova_table = sm.stats.anova_lm(model, typ=2)
anova_table
```

Out[45]:

	sum_sq	df	F	PR(>F)
ECMP	3.453888	3.0	51.110021	0.000015
Residual	0.180207	8.0	NaN	NaN

In [46]:
```
model = ols('Cardiac_Troponin ~ (ECMP)', data=df).fit()
anova_table = sm.stats.anova_lm(model, typ=2)
anova_table
```

Out[46]:

	sum_sq	df	F	PR(>F)
ECMP	5.732353	3.0	7.03551	0.012399
Residual	2.172732	8.0	NaN	NaN

In [47]:
```
model = ols('MLC2a ~ (ECMP)', data=df).fit()
anova_table = sm.stats.anova_lm(model, typ=2)
anova_table
```

Out[47]:

	sum_sq	df	F	PR(>F)
ECMP	11.017982	3.0	71.613079	0.000004
Residual	0.410278	8.0	NaN	NaN

In [48]:
```
model = ols('MLC2v ~ (ECMP)', data=df).fit()
anova_table = sm.stats.anova_lm(model, typ=2)
anova_table
```

Out[48]:

	sum_sq	df	F	PR(>F)
ECMP	0.067052	3.0	0.640087	0.61027
Residual	0.279344	8.0	NaN	NaN

When perfroming MANOVA we assumed there was a statistically significant differnece between the 4 protein substrate combinations (Matrigel, C1C3C4V, C3C4FV, C1C3FLV). Performing an LDA post-hoc test we see all groups are seperated well indicating significant differnece between the four groups. Finally perfroming ANOVA tests on the indipendant biomarkers between the four grups, we find Brachyury, MESP1_pre, Cardiac_Troponin, and MLC2a also have significantly differnet values between the four ECMP groups.

Using G*Power 3.1 the following was performed.

MANOVA: Global Effect A priori: Compute required sample size - given alpha, power, and effect size

Effect size F^2(V) was calculated with the following values

Pillai V = 0.995 (intercept value from table above) Number of groups = 4 Responce varaibles = 6

Input parameters

Effect size F^2(V) = 0.4962594 alpha err prob = 0.05 power (1-beta err prob) = 0.8 number of groups = 4 responce variables = 6

For future work, a Recomended sample size = 20 should be used to confirm statistical significance between the 4 groups with these 6 biomarker stains.

```
In [ ]:
```

- A straightforward protein microarray approach to evaluate the utility of initial matrix coatings in promoting pluripotency, germ layer specification, and cardiomyocyte differentiation, using pluripotent stem cells.
- Combinatorial screen with statistical analysis identifies proteins that guide cardiomyocyte differentiation from pluripotent stem cells.
- Specific combinations of matrix proteins at initial adhesion can control cardiomyocyte differentiation.
- Combinations of molecular marker immunofluorescence and high-speed video analysis determines chamber-specific contraction profiles.

Declaration of interests

☒ The authors declare that they have no known competing financial interests or personal relationships that could have appeared to influence the work reported in this paper.

☐ The authors declare the following financial interests/personal relationships which may be considered as potential competing interests: